DIGITAL HOLOGRAPHIC DIAGNOSTICS

OF NEAR-INJECTOR REGION

By

JAIHO LEE

Bachelor of Science
Chonbuk National University
Jeonju, Jeonbuk, South Korea
2002

Master of Science
Chonbuk National University
Jeonju, Jeonbuk, South Korea
2004

Submitted to the Faculty of the
Graduate College of the
Oklahoma State University
in partial fulfillment of
the requirements for
the Degree of
DOCTOR OF PHILOSOPHY
May, 2009

DIGITAL HOLOGRAPHIC DIAGNOSTICS

OF NEAR-INJECTOR REGION

Dissertation Approved:

Dr. Khaled A. Sallam
_____
Dissertation Adviser

Dr. Afshin J. Ghajar
_____

Dr. Frank W. Chambers
_____

Dr. Bruce J. Ackerson
_____

Dr. A. Gordon Emslie
_____
Dean of the Graduate College

ACKNOWLEDGMENTS

I wish to express my appreciation for Heavenly Father. I also wish to express my sincere gratitude to my parents and their support and love. In particular, I would like to express my genuine appreciation to my father. He eagerly looked forward to attending my commencement, but passed away last year.

I am thankful for the support and guidance from my advisor, Dr. Khaled Sallam. I also express my gratitude to Drs. Afshin Ghajar (committee chair), Frank Chambers, and Bruce Ackerson for their participation on the thesis committee. Finally, I would like to thank Anu Osta and Brian Miller for all of their assistance.

TABLE OF CONTENTS

LIST OF TABLES

LIST OF FIGURES

viii

NOMENCLATURE

d $\qquad$ = drop diameter

d_j $\qquad$ = jet diameter

d_o $\qquad$ = injector orifice diameter

q_o $\qquad$ = jet/freestream momentum flux ratio, $\rho_L v_j^2 / \rho_\infty u_\infty^2$

GLR $\qquad$ = aerating gas-to-liquid mass flow rate ratio

SMD $\qquad$ = Sauter mean diameter, $\sum_{i=1}^{n} d_i^3 \Big/ \sum_{i=1}^{n} d_i^2$, d_{32}

MMD $\qquad$ = mass median diameter, $d_{0.5}$

M $\qquad$ = freestream Mach number

We_L $\qquad$ = jet Weber number, $\rho_L d_j v_j^2 / \sigma$

We_∞ $\qquad$ = crossflow Weber number, $\rho_G d_j u_\infty^2 / \sigma$

Re $\qquad$ = Reynolds number, $\rho_L d_j v_j / \mu_L$

Oh_L $\qquad$ = liquid jet Ohnesorge number, $\sqrt{We_L} / Re_L = \mu_L / \sqrt{\rho_L \sigma d_j}$

u $\qquad$ = velocity component in the crossflow (horizontal) direction

U_∞ $\qquad$ = freestream velocity

v $\qquad$ = velocity component in the jet streamwise (vertical) direction

v_j $\qquad$ = jet exit velocity

w	= velocity component in the jet spanwise (normal to the page) direction
x	= cross-stream (horizontal) distance from the injector exit
y	= streamwise (vertical) distance from the injector exit
z	= spanwise (normal to the page) distance from the injector exit
R	= conversion factor, D_m/D_p
S	= conversion factor, G_m/G_R
D	= pin diameter
G	= gap distance in spanwise direction between each calibration pin
ρ	= density
ν	= kinematic viscosity
σ	= surface tension
$\Delta\xi$	= hologram resolution
Δd	= distance from the objective lens to CCD sensor
λ	= wave length
N	= the number of pixels
Δx	= the pixel size
X	= reconstructed distance (mm)
Y	= ratio of pin diameter to pixels
s	= standard deviation
n	= number of samples of data
t	= t-distribution
$1-\alpha$	= confidence level

Subscripts:

G   = aerating gas property

j   = jet exit property

L   = liquid property

∞ = freestream property

m   = metric dimension

p   = pixel dimension

R   = reconstructed

eq   = equivalent

τ = depth of focus

Superscripts:

~   = mass averaged properties

ABSTRACT

Study of primary breakup of liquid jets is important because it is motivated by the application to gas turbine fuel injectors, diesel fuel injectors, industrial cleaning and washing machine, medical spray, and inkjet printers, among others. When it comes to good injectors, a liquid jet has to be disintegrated into a fine spray near injector region during primary breakup. However the dense spray region near the injectors is optically obscure for Phase Doppler Interferometer like Phase Doppler Particle Analyzers (PDPA). Holography can provide three dimensional image of the dense spray and eliminate the problem of the small depth of focus associated with shadowgraphs. Traditional film-based holographic technique has long been used for three dimensional measurements in particle fields, but it is time consuming, expensive, chemically hazardous. With the development of the CCD sensor, holograms were recorded and reconstructed digitally. Digital microscopic holography (DMH) is similar to digital inline holography (DIH) except that no lens is used to collimate the object beam. The laser beams are expanded with an objective lens and a spatial filter. This eliminates two lenses from the typical optical path used for in-line holography, which results in a much cleaner hologram recording. The DMH was used for drop size and velocity measurements of the breakup of aerated liquid jets because it is unaffected by the non-spherical droplets that are encountered very close to the injector exit, which would cause problems for techniques

such as Phase Doppler Particle Analyzer, otherwise. Large field of view was obtained by patching several high resolution holograms. Droplet velocities in three dimensions were measured by tracking their displacements in the streamwise and cross-stream direction and by tracking the change in the plane of focus in the spanwise direction. The uncertainty in spanwise droplet location and velocity measurements using single view DMH was large at least 33%. This large uncertainty in the spanwise direction, however, can be reduced to 2% by employing double view DMH. Double view DMH successfully tracked the three dimensional bending trajectories of polymer jets during electrospinning. The uncertainty in the spatial growth measurements of the bending instability was reduced using orthogonal double view DMH. Moreover, a commercial grade CCD was successfully used for single- and double-pulsed DMH of micro liquid jet breakup. Using a commercial grade CCD for the DMH, the cost of CCD sensor needed for recording holograms can be reduced.

CHAPTER I

INTRODUCTION

1.1 Background

In the field of atomization and spray, imaging diagnostics are very useful in obtaining visualizations and measurements of drop sizes, locations, and velocities. They offer many advantages over traditional diagnostics due to their simplicity, flexibility, and non-intrusiveness. However, the field of view, the depth of focus, the frequency of taking photographs, and the tedium of the direct measurement of sizes of individual drops should be considered carefully in order to obtain high quality flow visualization and measurements. Shadowgraphs and holograms were extensively used for flow visualization and to provide measurements of liquid atomization and spray systems (Wu et al., 1997; Mazallon et al., 1999; Burke et al., 2003; Sallam et al., 2004; Miller et al., 2008, among many others).

1.2 Problem Statement

The breakup of liquid jets is three-dimensional by their very nature, and important properties such as drop sizes and drop and jet velocities, and rates of primary and secondary breakup are difficult to measure with 2-D techniques such as shadowgraphy

(e.g. Sallam et al., 1999, 2002) because only a small number of droplets will be in focus in each individual image. Holographic techniques (Hariharan, 2002) on the other hand, can be utilized to obtain three dimensional image of the spray with almost every drop in focus. Moreover, because it provides the phase information, holographic techniques can be automated to find the location, size and velocity of every droplet in the measuring volume. A digital holographic based diagnostic should therefore be developed for investigating the dense spray near injector region.

1.3 Previous Studies

1.3.1 Digital Holography

Holography relies on the interference of two waves of coherent light: 1) the object wave, which is diffracted by the object being recorded and 2) the reference wave, which represents the status of the object wave before it was affected by the object. As the object wave comes in contact with the object, the phase of the light wave is changed. Later when it meets the reference wave an interference pattern is formed which can be recorded as a hologram on the CCD sensor. This interference pattern (hologram) has information of both the phase and the magnitude of the object wave. If the original reference beam is shone onto the hologram then a 3-D image is reproduced having the same characteristics of the original object. This technique was first invented by Gabor (1948) and later it was made practical with the use of off-axis reference beam (Leith and Upatnieks, 1965), which separated the real and virtual images. With the advancements in computer technology, Goodman and Lawrence (1967) found that holograms could be recorded on

film and reconstructed digitally. Later with the development of the CCD sensor, Schnars and Juptner (1994) recorded and reconstructed holograms entirely digitally.

Two light waves are still needed in digital holography, but they can be included within the same laser beam since the portions of the laser beam that are unaffected by the object can serve as the reference wave. This single collimated beam setup is preferred over other possible holographic recording methods because of its simplicity and its favorability to digital recording. The inline arrangement (e.g. Meng and Hussain, 1995, Xu et al., 2001, 2002) reduces the spatial resolution requirements on the CCD sensor which typically has an order of magnitude lower resolution than a holographic film. The interference of the object and reference waves creates light and dark fringes, and according to the sampling theorem each fringe has to fall across two pixels to be resolved. The frequency of these fringes increases as the angle between the object and reference beam increases. Therefore, the in-line arrangement is the most suitable for present-day CCD sensors. In addition to its lower resolution requirements, the in-line arrangement does not require the matching of the optical paths of the two waves and this simplifies the experimental setup.

The principal drawback with this single beam setup is that resolution decreases in a dense spray because there is not enough of the beam that passes through the volume unaffected by particles to serve as a reference wave. The Royer criterion (Jones et al., 1977) quantifies this amount of obscuration based on "shadow density." According to the Royer criterion, hologram quality can be defined as follows: a shadow density less than

1% produces a "good" hologram, between 1% and 10% produces a "marginal"-quality hologram, and greater than 10%, a "bad" hologram. Adding a separate reference beam solves the beam obscuration problem. However, to keep the low fringe frequency both the object and reference beam are combined with a beam splitter and sent to the CCD with in-line configuration.

The addition of a separate reference beam solves the problem of beam obscuration, but it does not solve all the problems associated with recording dense sprays. Another problem is intrinsic speckle noise. Meng et al. (1993) describes this speckle noise as the interference of the scattering waves from multiple particles. When the scattered light waves interfere with each other, they appear as a random pattern of speckles when the hologram is reconstructed. This causes a problem with automatic particle measurement because it becomes difficult to distinguish a focused droplet from the speckles. Meng et al. (1993) offers two ways to improve this problem: 1) suppress the undiffracted reconstruction wave (a.k.a. DC term) and 2) separate the virtual and real image through an off-axis setup. Schnars and Jueptner (2005) offer two simple ways of suppressing this DC term: 1) subtract the average intensity from the hologram or 2) measure the intensities of the reference beam and object beam separately and subtract the intensities from the hologram before reconstruction.

Digital microscopic holography (e.g. Garcia-Sucerquia, 2006, Garcia-Sucerquia et al., 2006) is similar in setup to standard in-line digital holography except no lens is used to collimate the beam. This method eliminates the need for a relay lens to introduce

magnification because the expanding beam provides the magnification needed. This eliminates two lenses from the optical path, which results in a much cleaner hologram recording and reconstruction. The expanding beam also increases the system resolution because the fringes that are needed to reconstruct the image are expanding with the laser beam. This allows for recording distance to be shortened which results in higher resolution. Sheng et al. (2006) suggested that inline digital microscopic holography is useful for measuring three dimensional particle distribution and motions. Miller et al. (2007) investigated the secondary breakup of aerated liquid jets in subsonic crossflow using holographic techniques. They compared two holographic methods: digital microscopic holography (DMH) and digital inline holography (DIH). The two methods were useful for probing the dense spray region of aerated liquid jets. They concluded that DMH is better due to the ability to resolve the smaller droplets in the spray. However, their setup was limited to single pulsed digital hologram and therefore did not permit any velocity measurement of liquid jets. Palero et al. (2007) used digital holography for micro droplet diagnostics. They suggested that digital image plane holography (DIPH) can overcome the drawbacks of inline digital holography, such as low particle concentration or low resolution in spanwise distance. However, when it comes to the cost of holography, the research grade PIV CCD is still expensive. In view of the rapid progress in commercial grade CCD, the objective of this study is to develop a cheap technique that provides visualization, size and velocity measurements of liquid jet breakup in the near injector region. One constraint, however, is that a digital camera with a removable lens is required for holography. Although a typical double-pulse Nd:YAG system is still

expensive, the advent of Diode Pumped Solid State (DPSS) lasers would offer similar possibilities on the illumination side.

1.3.2 Electrospinning of Polymer Jets

Electrospinning method is capable of producing fibers with the diameters ranging from sub-microns to nanometers using electrical forces (Reneker and Chum, 1996). The basic electrospinning experimental setup is relatively simple as shown in Figure 1-1 (Shin et al, 2001). The minimum requirements include a polymer solution, an electrode which is inserted into the polymer solution, a high voltage DC source connected to the electrode, and a grounded collector (Andrady, 2008). Electrospinning is a special case of electrohydrodynamic atomization. Jaworek and Krupa (1999) studied various modes of droplet formation (dripping mode, micro-dripping mode, spindle mode, and multi-spindle mode) and liquid jet formation (cone jet mode, oscillating jet mode, precession mode, and multi jet mode) by electro-hydrodynamic instabilities as shown in Figure 1-2. The dripping mode can be observed when electric potential between the nozzle tip connected to the high voltage source and the grounded electrode is very weak. With the increase in the applied voltage, the dripping mode is changed into micro-dripping mode or spindle mode. An axisymmetric Taylor cone is formed at the nozzle tip in the cone jet mode. The liquid jets ejected from the Taylor cone experience axisymmetric instability and bending instability (also known as whipping instability). The subsequent modes are the oscillating jet mode and multi jet modes. The oscillating jet mode is similar to the cone jet but the Taylor cone at the nozzle tip is deformed. Precession mode is the oscillating jet mode with a bending instability. Finally multi jet mode can be observed at low surface tension

and high applied voltage. The multiple jets ejected from a Taylor cone experience a bending instability.

Stabilization of the Taylor cone is imperative for the generation of uniform nanofibers during the electrospinning process because the unsteady deformation of the Taylor cone can prevent the stable polymer jets from being ejected from the cone. Rutledge and Fridrikh (2007) explained the electrospinning process with five operational components: fluid charging, formation of the cone-jet, thinning of the steady jet, onset and growth of jet instabilities, and collection of the fibers. A nozzle (or capillary tube) including a polymeric solution keeps a distance (e.g. 20 cm) from a grounded collector, which connects to an electrode of high voltage power (Shin et al., 2001). Initially a droplet forms at the tip of the tube due to the solution surface tension. However, with the increase in the electric potential between the tube containing the polymer solution and the grounded collector, the charge repulsion generates an electric force overcoming the surface tension of the solution. When the electric force defeats the surface tension, the droplet on the nozzle tip becomes distorted forming a Taylor cone. At a critical voltage, a charged polymer jet ejects from the tip of the Taylor cone and moves toward the grounded collector. The diameter of the cone jet is a function of distances from the apex of the cone due to the evaporation of the solvent (Doshi & Renerker, 1999, and Shin et al., 2001). The straight cone jet starts to curve at a critical distance due to the non-uniform distribution of surface charges (i.e. bending instability).

The different jet instability modes during electrospinning process have been studied by many (Shin et al., 2001, Yarin et al., 2001, Hohman et al., 2001, and Reneker et al., 2000). There exist three different instabilities during electrospinning process: the Rayleigh instability, the axisymmetric conducting instability, and the bending conducting instability (Shin et al., 2001 and Hohman et al., 2001). The Rayleigh instability is axisymmetric and dominated by the surface tension, but the axisymmetric conducting instability is sensitive to fluid conductivity much more than the surface tension. In axisymmetric instability modes, the cross sectional area of the polymer jets is modulated along the constant centerline of the jets. High applied voltage suppresses the axisymmetric instability but favors the bending instability (Hohman et al, 2001). The typical bending instability is shown in Figure 1-3. The bending instability results from the increase in the surface charges of the jet, and results in a complicated three dimensional motion (Yarin et al., 2001). The diameter of the jet is maintained constant but the center line of the jet is modulated (Hohman et al., 2001). Consequently the bending instability drastically increases the surface area of the jet and decreases the surface charge density of the jet as shown in Figure 1-4 (Shin et al., 2001). The bending instability can be dampened using an electrostatic lens element and biased collection target (Deitzel et al., 2001). Wannatong et al. (2004) reviewed the different forces acting on the bending instability. The forces include gravitational force, electrostatic force, coulumbic repulsion forces, viscoelastic forces, surface tension force, and frictional forces between the surface of the jet and the ambient gas. The jet diameter and the direction of the motion are determined by the sum of the forces. The jet becomes bent apparently due to the interaction of the different perturbations. Many studies for the

8

development of numerical models and theoretical analysis to predict the trajectories of the jet have been made (Shin et al., 2001, Reneker et al., 2000 and Yarin et al., 2005). Another concern is most studies have been limited to two dimensional trajectories due to their optical setup. Thus, tracking the three dimensional motion of polymer jets is still needed to validate the computational models of the electrospinning process. Experimentally it has been very challenging to measure the trajectory using photography due to the small depth of field encountered at the high magnification necessary for such small objects and the three dimensional motion of the trajectory.

Zuo et al. (2005) experimentally studied the relationship between jet instability and bead formation of nanofibers. They concluded that axisymmetric instabilities promote the elongation of the polymer jets to accommodate surface charges and result in the formation of beaded polymer nanofibers and that two axisymmetric instabilities including the Rayleigh instability and the axisymmetric conducting instability influence the bead formation of the electrospun nanofibers. To observe the morphology of the polymer jet at different distance from the nozzle tip, they moved a glass slide into the bending envelope region and examined the slide using a scanning electron microscope. They observed smooth fibers on the glass slides collected near the nozzle region, but wave-like and dumbbell-like fibers on the glass slides collected away from the nozzle as shown in Figure 1-5. Dumbbell-like fibers featured two or three beads on the elongated thin fiber. The beaded fibers can be produced with the increase in the axisymmetric instabilities, whereas the continuous uniform fibers can be generated by the decrease in axisymmetric instabilities. They also found that higher applied voltages and the increased

fluid conductivity favor uniform smooth fibers, but high solution feeding rates and high surface tension promote the formation of the beaded fibers. A concern, however, about their findings is the effect of evaporation and wetting of the samples they examined on the SEM and whether these collected fibers represent the nature of the polymer solution jet near the nozzle. An experimental technique that is capable of probing the polymer solution jet in-flight is needed to reveal the temporal and spatial growth of the axisymmetric instability. An experimental technique, e.g. digital double view microscopic holography, is needed to measure the three dimensional trajectories of the polymer jets and to examine the spatial and temporal growth rate of the bending and Rayleigh instabilities during the electrospinning process of beaded nanofibers.

1.3.3 Aerated Liquid Jets

A good understanding of the phenomena of liquid jet breakup is essential for successful design of gas turbine fuel injectors, ramjet and scramjet engines, diesel fuel injectors, medical sprays, and inkjet printers, among others. The major objective of most injectors is to atomize a liquid jet into a fine spray. Pressure atomizers, such as plain orifice nozzle injectors, accomplish this objective by using very small orifice diameter and/or very high injection pressure. In many applications this solution is not feasible, because small orifice diameters tend to get clogged easily and high injection pressure is not always available. An aerated liquid injector (also known as an effervescent atomizer), on the other hand, can easily provide dense sprays of fine droplets with low injection pressures and large orifice diameter by introducing gas bubbles into the liquid stream inside an injector. Aerated injection is similar to the flash atomization because it produces gas bubbles

inside the injector for promoting atomization. However, unlike flash atomizers, aerated injection can easily control the amount of bubbles and their sizes without the complications of dissolving gas or heating the liquid to its boiling point. The aerated liquid injector allows large exit orifice diameter because atomization quality depends on liquid sheet thickness rather than the orifice diameter. Moreover, the aerated atomization generates fine spray at low injection pressures and low gas flow rates for a wide range of operating viscosities.

The dense spray region near the injector is optically-opaque for Phase Doppler Interferometry, e.g. Phase Doppler Particle Analyzers (PDPA). Moreover, two-dimensional methods, e.g. shadowgraphy, have limited depth-of-field that renders them impractical for measuring droplet sizes and velocities of three-dimensional spray structure. Miller et al. (2008) have successfully used digital holography to probe the droplet sizes of an aerated liquid jet in crossflow at downstream distances between $x/d_o = 25$ and $x/d_o = 50$ using a single laser beam. They used two methods, digital inline holography (DIH) and digital microscopic holography (DMH) (also known as digital holographic microscopy), and demonstrated that the two methods are suitable for measuring the properties of the dense spray region and insensitive to the non-spherical droplets. They concluded that DMH is the best method for providing valuable information about the small droplets encountered in the spray because of its ability to resolve very small details. In spite of their efforts, however, there is still a lack of data on droplet velocities in the near field. There is also a lack of data on droplet sizes and droplet velocities very near the aerated injector ($x/d_o < 25$).

Kim and Lee (2001) studied the two phase internal flow pattern inside the aerated injector for different GLRs (Gas Liquid Ratio) by using a transparent aerated injector and pulsed shadowgraphy. The flow patterns inside the aerated injector could be classified into three regimes as follows: bubbly flow regime, intermittent flow regime, and annular flow regime. When the GLR is small, the flow pattern inside the injector becomes bubbly because small bubbles are distributed throughout the liquid. However, at a large value of GLR, a liquid layer is formed along the wall of the injector exit passage and the internal flow pattern becomes annular. At the intermediate GLR, the internal flow pattern randomly wanders between the bubbly flow and annular flow regimes.

Lefebvre et al. (1998) investigated the influences of nozzle geometric design on atomization performance. They concluded that exit orifice diameter has little effect on the mean droplet sizes. Buckner and Sojka (1991) investigated effervescent atomization of high viscosity fluids in the annular flow regime. They concluded that mean droplet diameter is sensitive to GLR but nearly independent of liquid viscosity, fluid supply pressure, and mixture mass flow rate as shown in Figure 1-6~1-8. Lund et al. (1993) reported the influence of surface tension on effervescent atomization. They found that drop size decreases with an increase in surface tension as shown in Figure 1-9.

Santangelo and Sojka (1995) investigated the near nozzle spray structure of an effervescent atomizer using focused image holography. They divided the spray structure into three flow regimes based on the GLRs. In bubbly flow regime, GLR < 2%, the

breakup process is governed by individual bubble expansion. A cylinder of liquid (a trunk) breaks up into ligaments and droplets due to individual bubble expansion as shown in Figure 1-10. In transition flow regime the trunk became distorted and was replaced by a ring of limbs, which formed a tree as shown in Figure 1-11. In the annular flow regime, the trunk is greatly reduced in length, and a small number of large limbs break up into a higher number of thinner limbs and branches. Sutherland et al. (1996) reported entrainment of ambient air into the spray produced by ligament controlled effervescent atomizer. The advantage of this atomizer is to get mean drop sizes below 70 µm, and to reduce atomizing air consumption by less than 0.009. They found that entrainment number which is function of steady entrainment rate and momentum rate is insensitive to liquid physical properties but increases with GLR. Wade et al. (1999) reported that the spray characteristics of an effervescent atomizer operating in the MPa injection pressure ranges. The Sauter mean diameter (SMD), an indicated diameter of the drop whose ratio of volume to surface area is the same as that of the entire spray, decreases with the increase in injection pressure. Spray cone angle was not influenced by the exit orifice diameter but increased with the increase of GLR and the injection pressure.

Lin et al. (2001 and 2002) studied the spray structure of the aerated liquid jet in crossflow using PDPA and pulsed shadowgraphy. They reported that as the GLR increased, the droplet distribution in the spray plume changed from multi-dispersed to mono-dispersed. They also suggested a correlation for the penetration height of the aerated liquid jet injected in crossflow. Sallam et al. (2006) investigated primary breakup of round aerated liquid jets in supersonic crossflow using single- and double-pulsed

shadowgraphy and holography. For GLR greater than 2%, the aerated liquid jet was in the annular flow regime, and spray cone angle and surface breakup properties along upstream and downstream of the liquid sheet were similar indicating weak aerodynamic effect as shown in Figure 1-12. They developed a correlation for the aerated liquid sheet thickness as shown in Figure 1-13. Miller et al. (2006) used two injector exit diameters of 1mm and 5mm, GLR of 4% and 8%, jet-to-freestream momentum ratios of 0.74 and 4 to investigate the spray structure at two locations of 25 and 50 jet diameters. The effect of GLR on the mean drop sizes is shown in Figure 1-14. The increase in GLR from 4% to 8% reduced the SMD probably due to the squeezing effect of the liquid sheet. The variation of the exit diameters influenced the number of droplets produced but not the droplet sizes. The jet-to-freestream momentum flux ratio had an effect on controlling the spray plume penetration. At the same GLR, the SMD was reduced between two different downstream locations of $x/d_o = 25$ and $x/d_o = 50$. They suggested that this effect was due to the secondary breakup. However, they did not perform any velocity measurements and therefore could not measure the rates of breakup in the near field. A velocimetry technique capable of probing the near-injector region is needed to measure the rates of breakup in this region.

1.4 Specific Objectives

In view of the recent findings about digital holographic diagnostics of near injector region, the specific objectives of this study were as follows:

1. Develop an inexpensive DMH technique for the near injector region using a commercial grade CCD.

2. Decrease the uncertainty of spatial measurements in spanwise direction and increase the spatial resolution in spanwise direction using double view DMH.

3. Find droplet velocities in three-dimensions by tracking their displacements during the time interval between the double-pulses in the streamwise and cross-stream direction and by tracking the change in the plane of focus in the spanwise direction.

4. Validate that DMH is a robust tool for investigating the dense spray near the injector region of aerated liquid jet in crossflow that is optically opaque to other non-imaging methods such as PDPA.

5. Complete new measurements and construct a data set of three dimensional maps of the spray structure for aerated liquid jet in crossflow in the near-injector region ($0 < x/d_o < 25$).

1.5 Organization of the Dissertation

This dissertation is organized into five chapters and two appendices. The problem statement, previous related studies, and specific objectives of the present study have been presented in the first chapter. The second chapter describes experimental methods including the optical setups of digital holographic diagnostics, validity of digital

microscopic holography (DMH), and uncertainty measurements. The experimental results are presented and discussed in the fourth chapter. Finally, the summary and main conclusions of the present investigation and recommendations for future study are presented in the fifth chapter. The two appendices deal with drop size distribution, and provide high resolution reconstruction holograms of the electrospinning polymer jets.
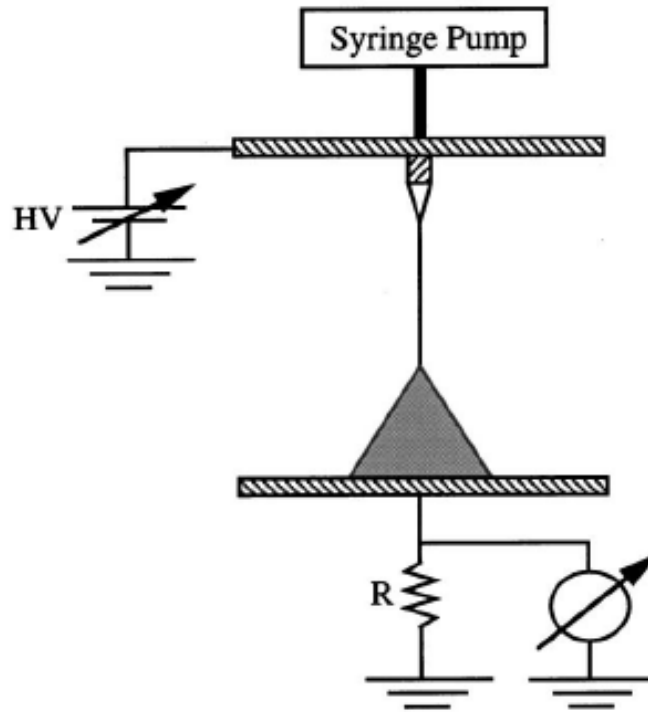
Figure 1-1 Schematic of electrospinning experimental setup.
The polymer jet moves toward the plate and the bending instability region
is indicated by the grey triangle (Shin, et. al., 2001).

Dripping   Microdripping   Spindle   Multispindle

Cone-jet   Oscillating-jet   Precession   Multijet
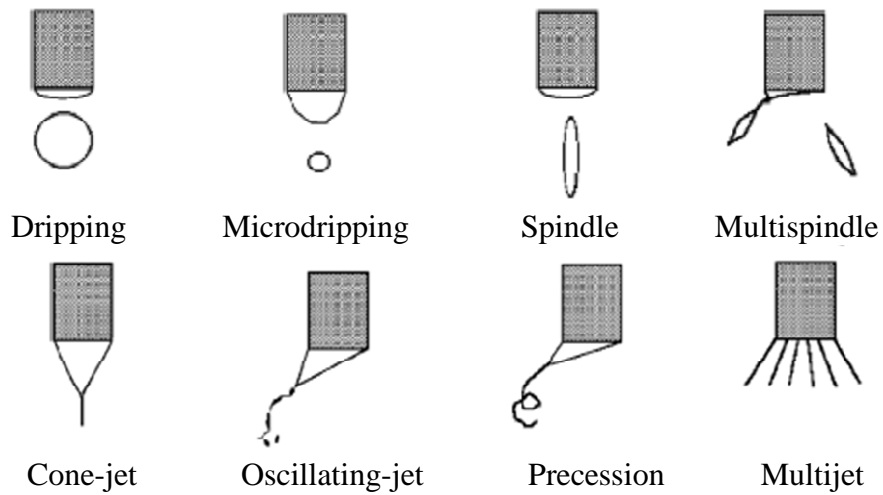
Figure 1-2. Modes of droplet and liquid jet formations
in the electrohydrodynamic (EHD) spraying (Jaworek and Krupa, 1999).

Figure 1-3 Bending instability (Yarin et al., 2001).
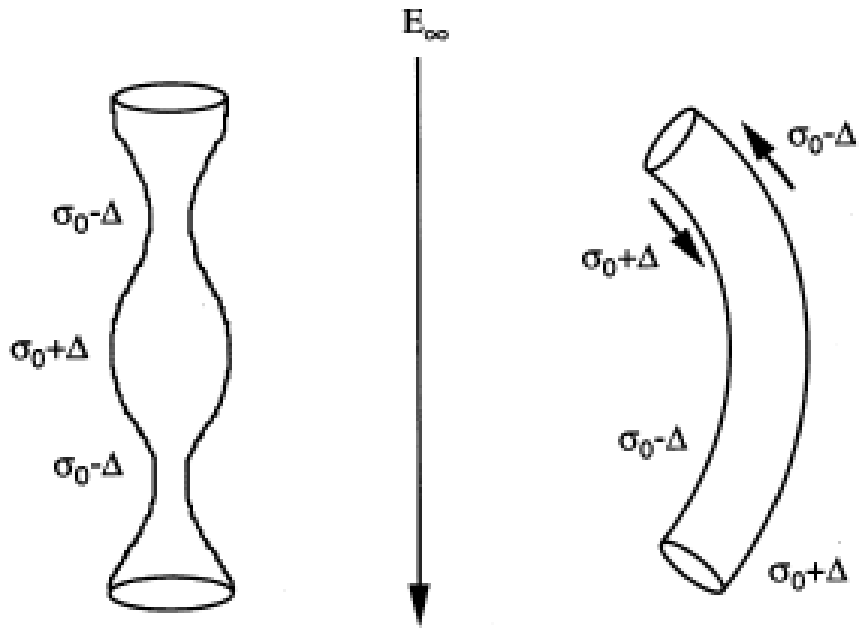
Figure 1-4. (a) Axisymmetric (b) non-axisymmetric instabilities. E_∞ is an external electric field, Δ denotes perturbations of the surface charge density (σ) (Shin et al., 2001).
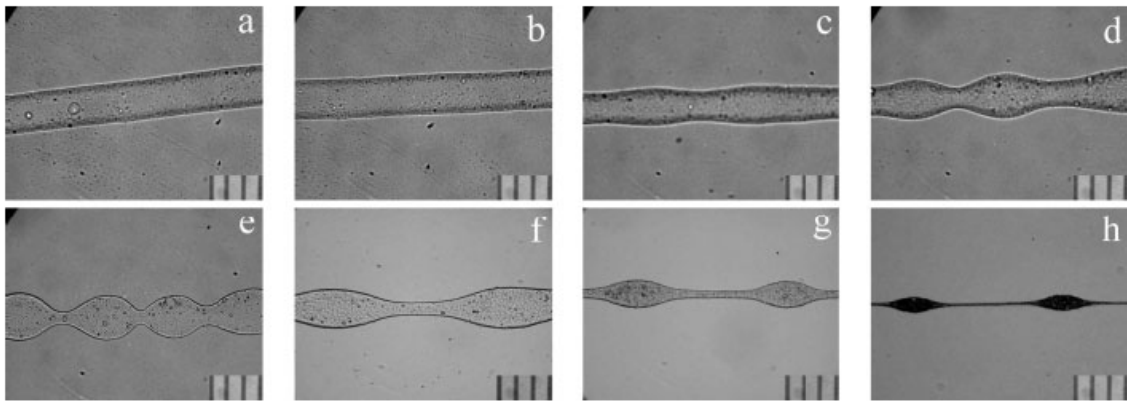
Figure 1-5 Bead formation process at different locations from the needle tip. Images from (a) to (h) correspond to 1, 3, 5, 7, 9, 12, 15, and 30 cm (Zuo et al., 2005).
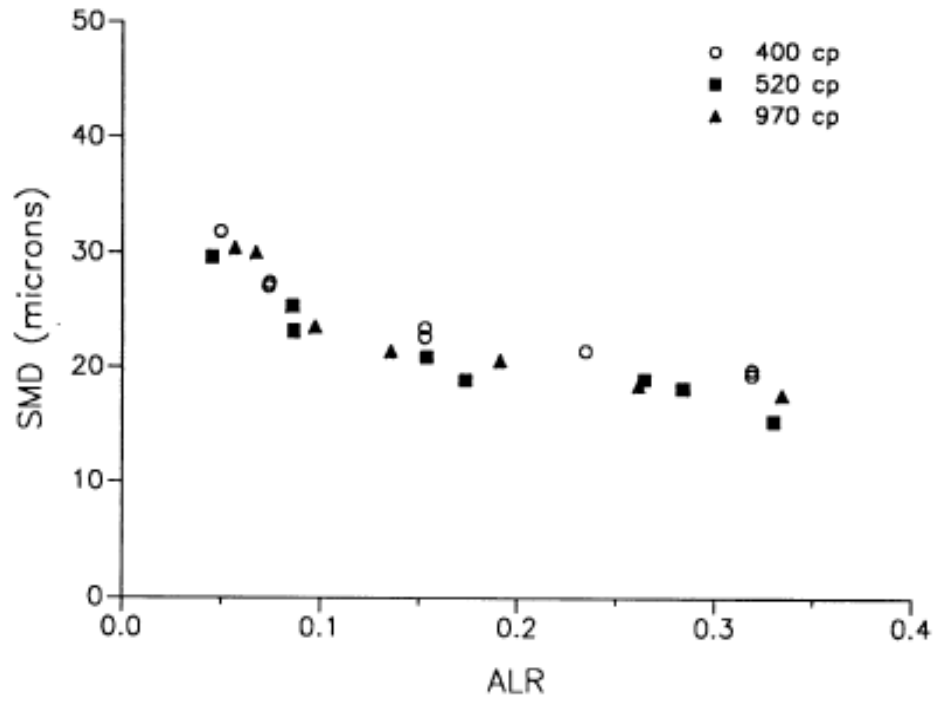
Figure 1-6 Influence of gas liquid ratio on mean drop-size
for three viscosities (Buckner et al., 1991).
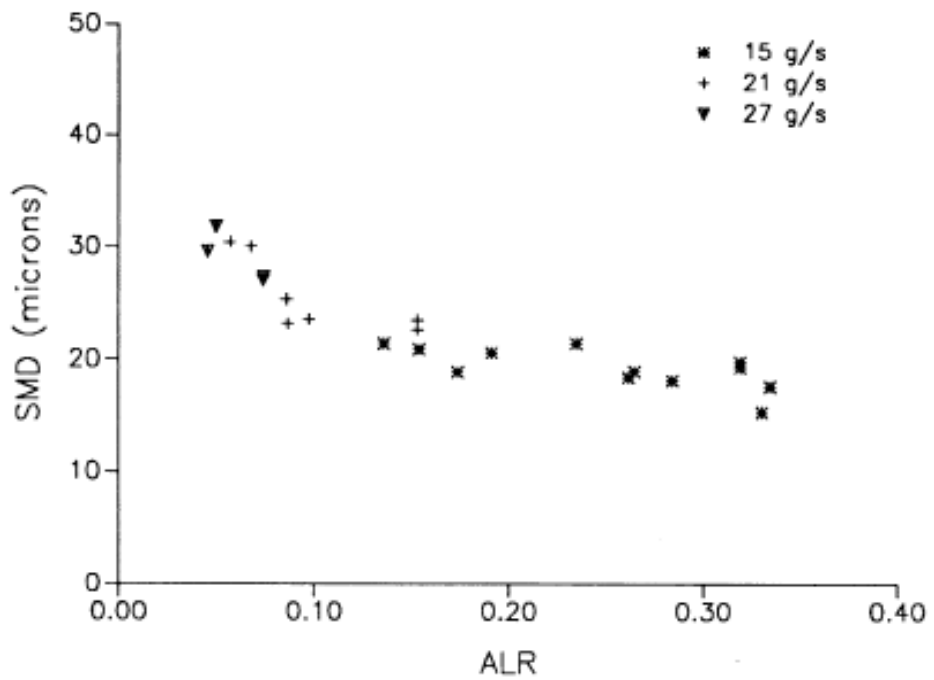
Figure 1-7 Influence of gas liquid ratio on mean drop-size
for three mass flow rates (Buckner et al., 1991).
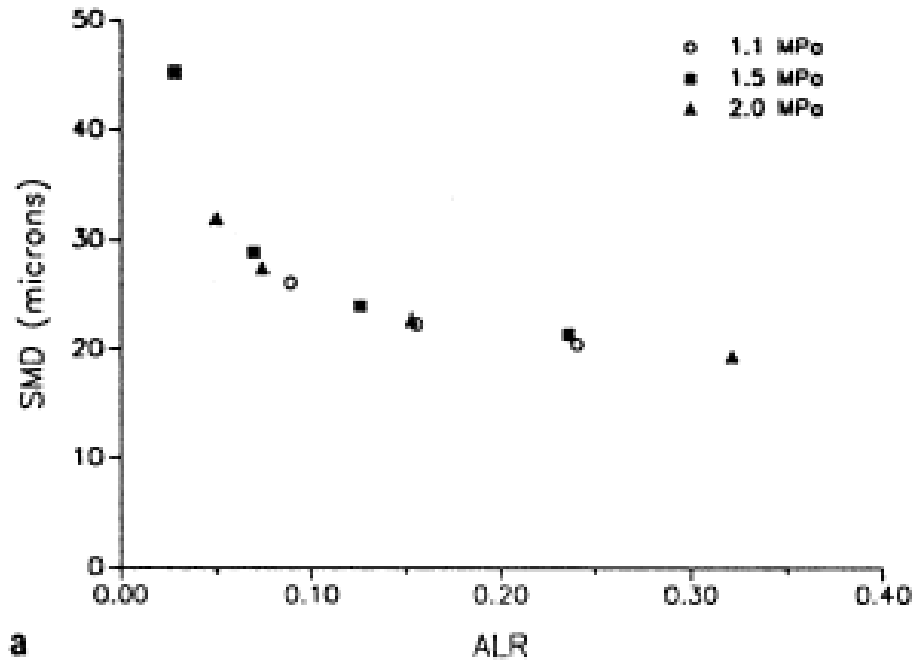
Figure 1-8 Influence of gas liquid ratio on mean drop-size
for three fluid supply pressure (Buckner et al., 1991).
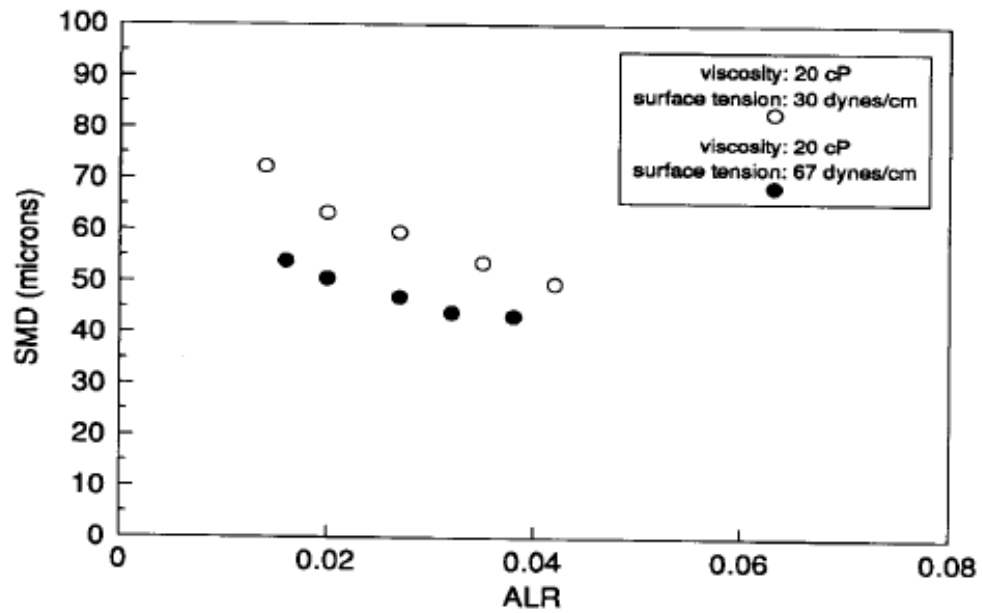
Figure 1-9 Influence of air liquid ratio on mean drop-size
for two surface tensions (Lund et al., 1993).
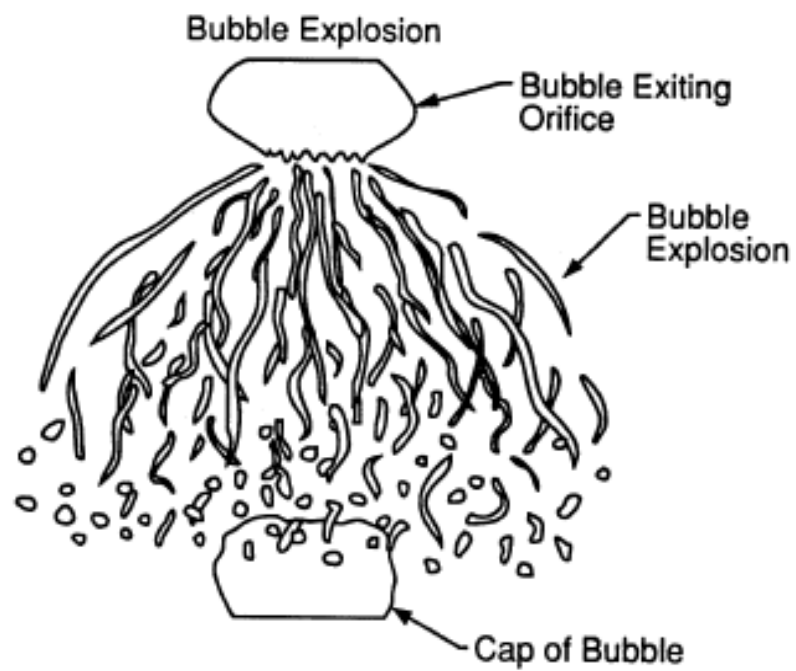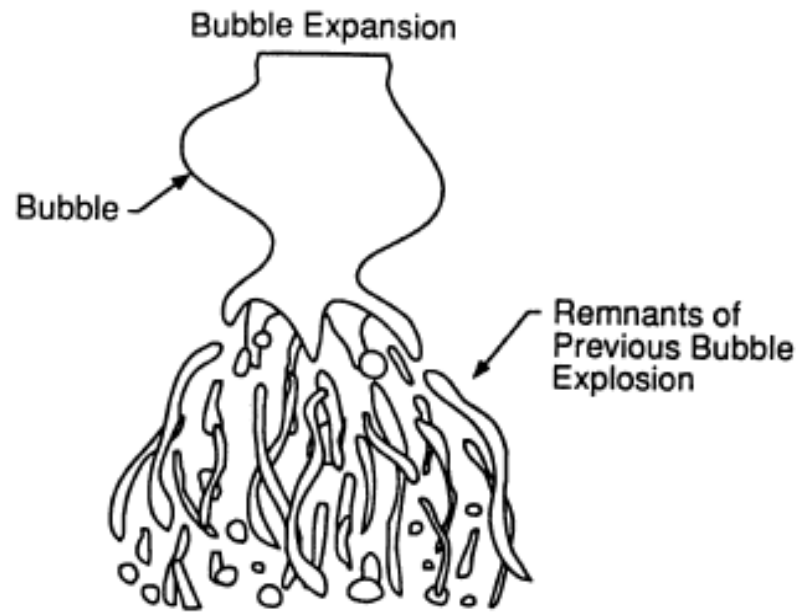
Figure 1-10 Sketch of bubbly flow regime near injector (Santangelo et al., 1995).
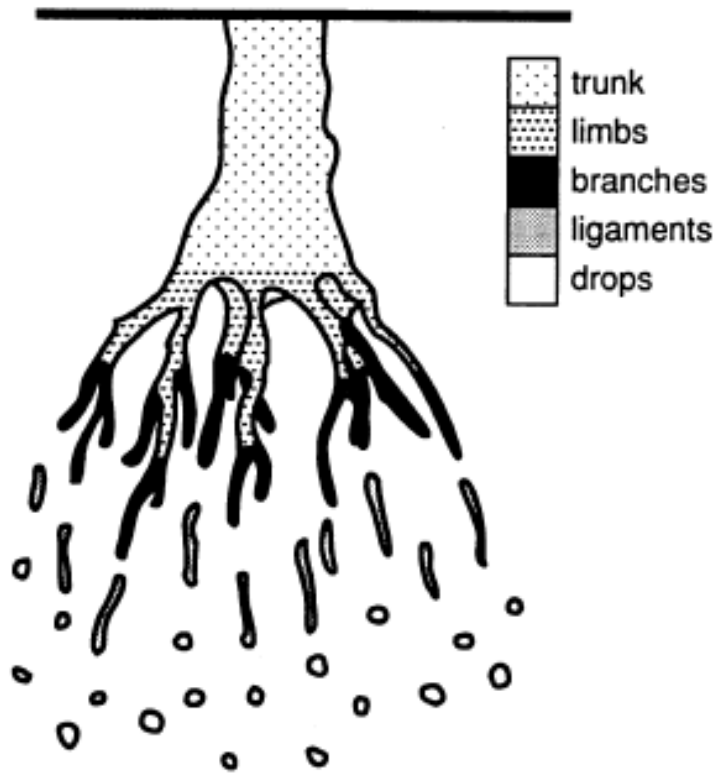
Figure 1-11 Sketch of tree regime near nozzle structure (Santangelo et al., 1995).
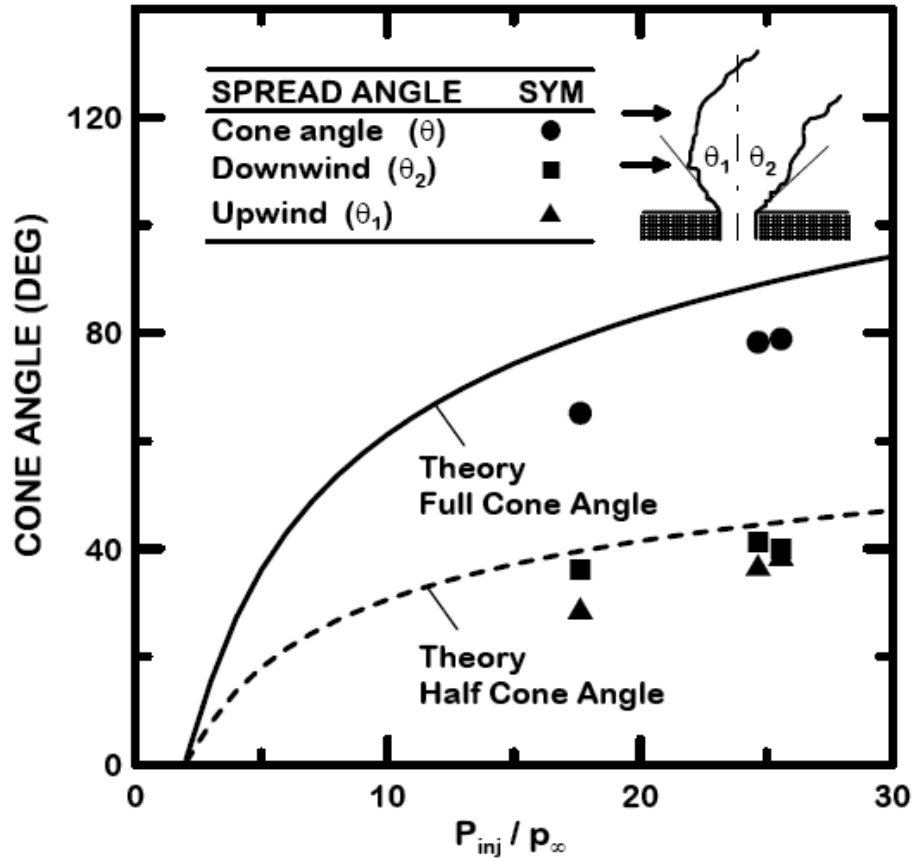
Figure 1-12 Cone angle of aerated liquid jets for the injector pressure ratio
(Sallam et al., 2006).
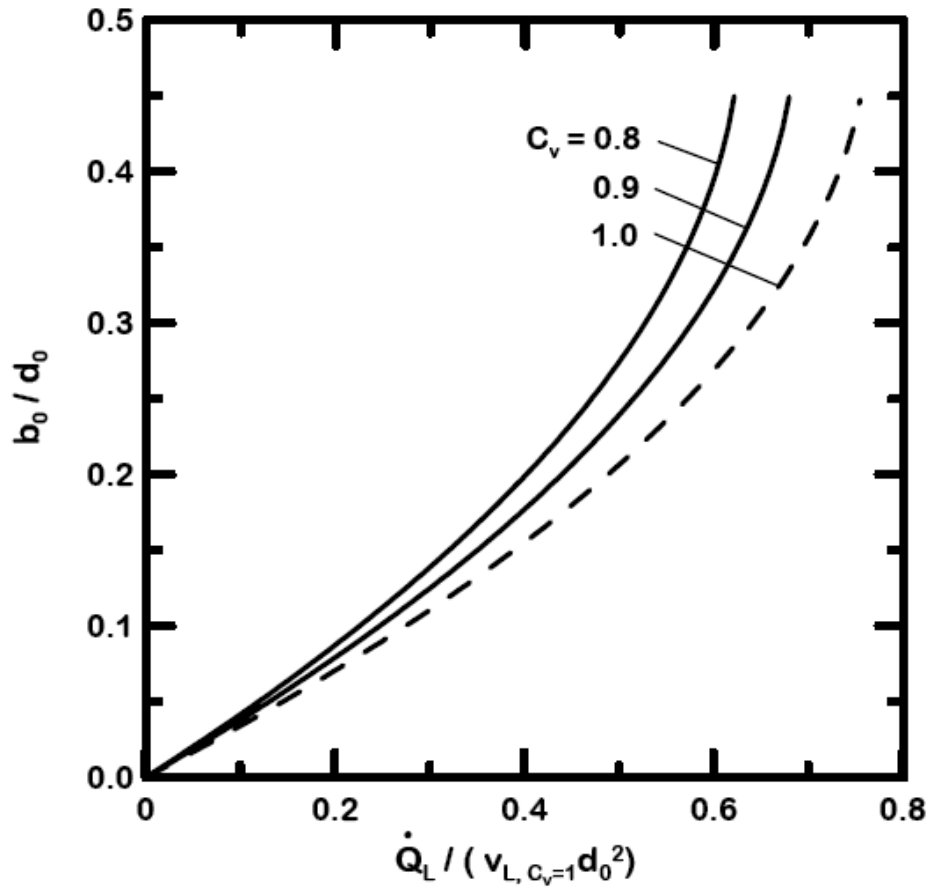
Figure 1-13 Effects of the velocity coefficient on initial liquid sheet thickness (Sallam et al., 2006).
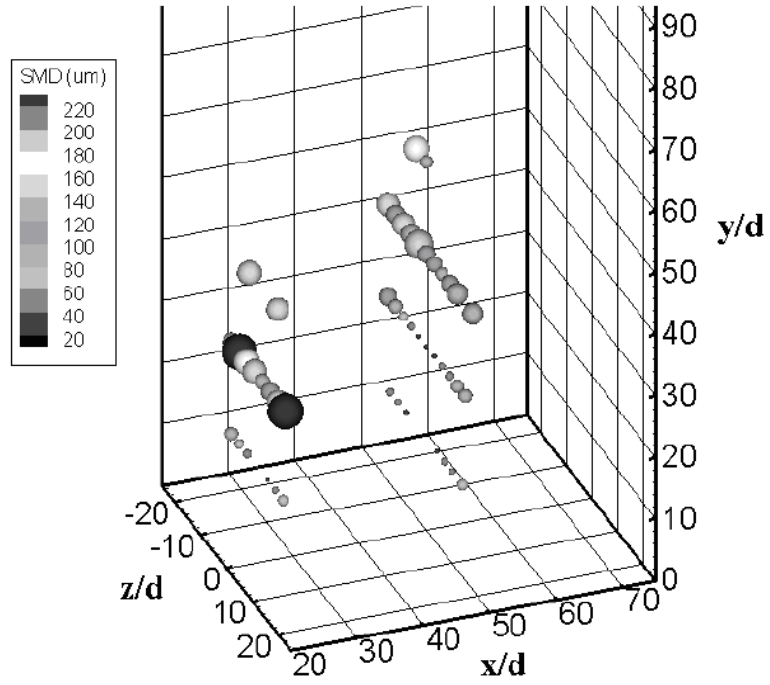
(a) GLR =4%
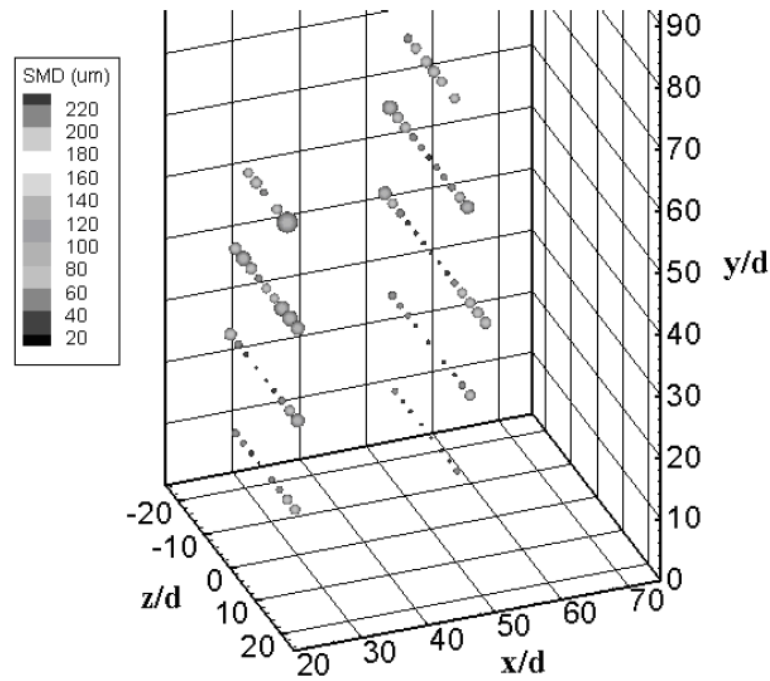
(b) GLR =8%

Figure 1-14 Influence of GLR on SMD distribution (Miller et al., 2008).

CHAPTER II

EXPERIMENTAL METHODS

Two different methods of digital holography were examined in the present study. The first was digital in-line holography (DIH), which relied on the use of either one collimated beam falling directly on the CCD sensor, or two collimated beams which were combined with a beam splitter and sent to the CCD in an inline configuration. The two beam setup can be used when the spray is dense and could block potentially the majority of the collimated beam passing through the spray. DIH could capture a large field of view and its experimental setup is simple. For higher magnification, but smaller field of view, digital microscopic holography (DMH) was used. DMH uses a single expanded beam falling on the CCD. This method provides higher resolution allowing smaller droplets to be seen. This technique removes two of the lenses that were necessary in the in-line setup which greatly reduces the aberration (i.e. an imperfection in image formation by an optical system) introduced by the lenses.

2.1 Optical Setup

2.1.1 Digital In-Line Holography (DIH)

The optical setup consisted of two frequency doubled Nd: YAG lasers (Spectra Physics

Model LAB-150, 532 nm wavelength, 7 ns pulse duration. The beams were combined using a polarized beam splitter cube. The resulting beam then passed through another polarized beam splitter cube, which only allows either the horizontal or vertical portion of polarized light to pass through while the other portion is reflected and directed to a beam dump located at the side of the cube. This combination of half wave plates and beam splitter cubes controls the intensity of the beam. The beam then passed through another half wave plate and polarized beam splitter cube to split the beam into object and reference beams. The reference and object beams then passed through a series of mirrors for positioning, and then passed through two 20x objective lenses and 76.2 mm diameter convex lenses with focal lengths of 150 mm. The object beam then passed through the test section and fell directly on the CCD as shown in Figure 2-1. The CCD that was first tested was a cooled interline transfer CCD camera (Cooke, Model: PCO 2000) having 2048 x 2048 pixels that were 7.4 μm wide by 7.4 μm tall. The reference beam passed under the test section and was then directed back up to the CCD and combined with the object beam by a beam splitter. The magnification was introduced by using a convex lens with a focal length of 300 mm as relay lens after the test section, and the magnified hologram was then captured by the CCD. After the hologram is recorded, it is reconstructed using the convolution type approach which solves the Rayleigh Sommerfeld formula for reconstruction of a wave field (Kreis et al., 1997).

The method of average intensity subtraction is used in the current setup to suppress the DC term when reconstructing the hologram, and the current setup neglects the out of focus virtual image because its effect is small enough that droplets can still be

resolved and measured accurately. When the smaller details need to be examined a relay lens must be introduced to provide magnification. This works adequately for low levels of magnification but aberrations in the relay lens begin to become a problem at higher levels of magnification. A reconstruction of a resolution target that was recorded using this method is shown in Figure 2-2 where the aberrations introduced from the relay lens can be seen clearly. The noise in this image poses a large problem for an automatic drop detection algorithm which is based on the intensity gradient within the image.

2.1.2 Digital Microscopic Holography (DMH)

For the digital microscopic holography (DMH) approach much of the same setup as described above was used except only one beam was used that was expanded, and then it passed directly through the test section to the CCD as shown in Figure 2-3. Digital microscopic holography can measure very small objects by employing a spherical reference beam instead of the collimated plane beam. For good resolution of holograms, the distance between CCD and the object has to be minimized. For good holograms of high magnification, the objective lens should be put near to the object and the CCD sensor should be placed far from the object. Despite this relationship between magnification and resolution of holograms, the total distance (Δd) from the objective lens to CCD sensor plays the primary role in reconstructing holograms. In this study the total distance (Δd) used for good focused holograms was 810 mm, and the distance between objective lens and the liquid jet was 560mm, and the distance between the jet and the CCD was 250mm. In the present experimental setup, two Nd:YAG lasers are used to generate two independent laser pulses. The intensity of two aligned lasers is controlled

by two ½ wave plates, and the laser beams are expanded through an objective lens (M 5x) and a 15 µm pinhole. The two lasers are fired by a pulse generator with different delay interval times (Δt) to measure the jet velocity. Initially the holograms were captured on a cooled interline transfer CCD camera (Cooke, Model: PCO 2000) having 2048 x 2048 pixels that were 7.4 µm wide by 7.4 µm tall. A commercial grade CCD (Nikon D-70 ~ $700) was then tested for holographic recording. Digital magnification can be introduced during the reconstruction after the hologram has been recorded. This is done by manipulating the equations used in reconstruction. The manipulation comes in the form of relocating the virtual source point used in reconstruction. However, this does not improve the actual resolution of the image. The actual resolution is controlled by the distance from the object to the CCD, the wavelength of the light, and the pixel size of the CCD. The equation for the resolution is given by Schnars and Jueptner (2005) as:

$$\Delta\xi = \lambda d \, / \, N\Delta x \qquad\qquad (2\text{-}1)$$

where $\Delta\xi$ (µm) is the resolution, λ (µm) is the wavelength of the light, d (µm) is the recording distance from the object to the CCD, N is the number of pixels, and Δx (µm) is the pixel size. The setup used in this study had typical resolutions on the order of $\Delta\xi$ = 10 µm. Figure 2-4 shows the reconstruction of the same resolution target that was recorded in Figure 2-2 using the DIH. The comparison between the resolutions of the two methods is in favor of DMH.

2.1.3 Double View DMH

Double view digital microscopic holography (DMH) was used to investigate the three dimensional motion of the polymer jets. To reduce the high uncertainty in the spatial measurements of the three dimensional trajectory, orthogonal double view DMH was employed. The optical setup of the orthogonal double view DMH is shown in Figure 2-5. A pulsed laser (Spectra Physics Model LAB-150, 532 nm wavelength, 7 ns pulse duration) was used as the light source and two CCD sensors (Nikon D-70, & D-80), were used to record two orthogonal holograms as illustrated in Figure 2-5. The laser beam was split to construct double view DMH. The orthogonal double view holograms were instantaneously recorded on the two commercial grade CCD sensors during the 7 ns pulse duration, and reconstructed numerically (Schnars and Jueptner, 2005).

2.2 Experimental Apparatus

2.2.1 Microjets

The water was first filtered with 0.2 μm pores to prevent the 100 μm orifice from clogging before it was used to fill the injector assembly. The internal geometry of the micro liquid injector is shown in Figure 2-6. Two washers are used to house the orifice and the two rubber rings used for sealing purposes. The water was injected through the orifice using compressed air which was stored in air tank upstream of the injector. The injection pressure was measured using a pressure gauge within 2% uncertainty. To measure the velocities of slow moving droplets one Nd:YAG laser (Spectra Physics Model LAB-150, 532 nm wavelength, 7ns pulse duration) and an external shutter were used. One laser can provide double pulses by using the shutter. However, double pulses

from one laser were not suitable for measuring velocities of fast moving droplets. The reason is that the delay time (Δt) between double pulses generated by one laser was 100ms limited by the laser repetition rate (10 Hz). The 100 ms is too large for the velocity measurement of the droplets resulting from the breakup of 100μm liquid jet. As a result, two Nd:YAG lasers are needed for velocity measurement of fast moving objects. The exposure time of the commercial-grade CCD was set at 2 seconds, and the delay time between the double pulses was controlled by a pulse generator. When two Nd:YAG lasers are controlled by using a pulse generator, the Q-switch delay time of each laser plays a role in determining delay time (Δt) between the double pulses. The Q-switch delay time was measured using an oscilloscope and a photo detector.

2.2.2 Electrospinning of Polymer Jets

The schematic of experimental apparatus is shown in Figure 2-7. A nozzle (capillary tube) with 0.5 mm diameter was attached to a cylindrical chamber (constructed of type 304 stainless steel) having the diameter of 100 mm and the height of 300 mm. The polymer solution is injected using air flow rate with constant suitable injection pressure controlled by a rotameter connected to the air pressure line. A high DC voltage power source (Glassman high voltage EL Series) was connected to an electrode attached to the nozzle. Electric fields ranging from 5 kV to 15 kV were applied to make stable cone jets at the nozzle tip and the distance between the nozzle and the grounded collector was 105 mm.

2.2.3 Aerated Liquid Jets in Crossflow

The aerated liquid jet breakup experiments were performed in a subsonic wind tunnel with a test section of 0.3 m (length) × 0.3 m (height) × 0.6 m (width). This test section had float glass side walls and floor, and acrylic ceiling to provide optical access. The range of air velocities was from 3 m/s to 60 m/s at normal temperature and pressure. The wind tunnel's contraction ratio is 16:1, and the velocity inside the test section has a variation within ± 1% of the mean free-stream velocity. Air velocities in the wind tunnel could be measured within ± 2%. The test liquid was supplied from a cylindrical chamber (constructed of type 304 stainless steel) having a diameter of 100 mm and a height of 300 mm, and the aerating gas for mixing with the liquid was provided from a stainless steel static pressure tank with a volume of 0.18 m^3 and an air pressure limit up to 5000 kPa. An aerated injector has been installed on the acrylic ceiling of the test section to provide optical access. The exit diameter (d_o) of the aerated liquid injector used for this research was 1.0 mm. Aerating gas supplied from the storage tank comes in to meet with the liquid inside the nozzle by traveling through the inner tube and passing through 100 μm holes located near the end of the injector as shown in Figure 2-8. The jet, at sufficient GLR (the value of GLR at which the injector delivers an annular flow is design dependent), forms an annular-type spray of two-phase flow composed of a gas core surrounded by a thin liquid sheet. Air pressures up to 1.1 Mpa was used in the aerating gas, and water, also pressurized to 1.1 Mpa, was used as the liquid.

The schematic diagram of experimental apparatus including optical setup is shown in Figure 2-9. The flow rate of liquid and aerating gas for effective GLR was

controlled by a rotameter type flow meter. The reading error of air flow rate was within ± 3 cc/s, and that of water flow meter was within ± 0.02 cc/s. Therefore, the gas flow rate measurement has the maximum uncertainty of 28%, but the maximum uncertainty in the liquid flow rate measurement is decreased to 6%. An aluminum black breadboard was installed under the wind tunnel test section for easy routing of the double pulsed lasers from an optical table to the wind tunnel test section. Moreover, this breadboard has a rail that can be moved horizontally. This was used to traverse the CCD camera and the objective lens and the spatial filter assembly with 1 mm accuracy. The schematic of double pulsed inline digital microscopic holography is shown in Figure 2-3. Two laser beams were combined by a polarized beam splitter. Two different beams, reference beam and objective beam, are needed for the digital holography. However they can be within the same expanding beam as shown in Figure 2-3. In inline digital microscopic holography, the portions of the beam which are unaffected by the object can be used as the reference beam. The holograms were captured on a Cooke Corporation cooled interline transfer CCD camera (Model : PCO 2000) having 2048 × 2048 pixels. Two laser pulses were synchronized with the double exposure time of CCD by a pulse generator. Two frequency doubled Nd:YAG lasers (Spectra Physics Model LAB-150, 532 nm wavelength, 7 ns pulse duration, and up to 300 mJ optical energy per pulse) that could be fired with a pulse separation as small as 100 ns were used as the light source. The two laser beams were aligned with a polarized beam splitter cube, and their intensities were controlled by two half wave plates as shown in Figure 2-3. A photo detector and an oscilloscope (Lecroy model 9314L, 300Hz bandwidth, 1Mpt memory depth, 100Ms/s sample rate) were used to measure the separation time between the two pulses. An

34

objective lens (M 5x) and a 15 µm pinhole were used to expand the laser beam for digital microscopic holography. The distance from the light source to the CCD was recorded within 1 mm accuracy during the test since it is needed for the digital reconstruction process.

2.3 Instrumentation

When the digital hologram is stored on the CCD sensor, it can be easily reconstructed by a numerical algorithm (Schnars and Jueptner, 2005). After the reconstruction process, three-dimensional volume information is expressed by many reconstruction holograms focused on each two-dimensional plane. In ordinary 2-D techniques an image of an object of known dimensions would be captured and a global calibration could be applied. However, this same technique can not be used for the DMH because objects closer to the CCD sensor appear smaller than those farther away because of the use of expanding laser beam in the recording process. In the present study, four pins with the same diameter ($d_{pin} = 0.5$mm) as shown in Figure 2-10 were used to spatially calibrate the reconstructed holograms. The spacing among four pins was respectively 5 mm in the spanwise direction, i.e., laser beam direction. The hologram for spatial calibration was obtained with a distance of 550 mm between objective lens and CCD, and the Q-switch laser energy used was 52.8 mJ/pulse. Figure 2-11(a) shows the original hologram of four pins and reconstruction two-dimensional image at the depth of 76 mm. When a pin on the original hologram is reconstructed in a two-dimensional plane, the others are out of focus. The second pin in Figure 2-11(b) is very focused, but the other pins are out of focus because this hologram was reconstructed at the depth of 76 mm. Four pins have

been consecutively reconstructed with 3 mm distance interval of ranging from 70 mm to 79 mm as shown in Figure 2-11(b). In other words, actual distance (the spacing of four pins) is 5 mm, but each pin was reconstructed with the distance interval of 3 mm. The spanwise actual distance was determined by this ratio. Because of expanding laser beam diameter, the reconstructed image of each of the identical four pins had different diameter. Figure 2-12 shows the spatial calibration relationship used in the present study. The linear correlation of Figure 2-12 is as follows:

$$Y = -0.021X + 5.591 \tag{2-2}$$

where Y is the ratio of pin diameters (µm/pixels) and X is the reconstruction distance (mm). The streamwise actual distance and cross-sectional actual distance can be calibrated with this equation by counting pixel number for all reconstruction holograms. Thus, this equation becomes very useful for getting the actual distance in each reconstruction two-dimensional plane.

2.4 Test Conditions

2.4.1 Microjets

A micro injection system which is flexible to the alternation of different orifices with the diameters of 100µm, 25µm and 1µm was designed and installed into the shock tube test section of 60mm×40mm. Jet exit conditions were limited to jet exit Reynolds number (Re_L) of 2500~5800, jet exit Weber number (We_L) of 900~4900, liquid/gas density ratio of 690, liquid jet Ohnesorge numbers (Oh_L) of 0.013, and gaseous crossflow Weber

number (We_∞) of 13. Ohnesorge number indicates the ratio of an internal viscosity force to a surface tension force.

2.4.2 Electrospinning Polymer Jets

Two solutions with concentrations of 0.5% and 2.0% of polyethylene oxide (PEO) with an average molecular weight 9×105 g/mol in distilled water were used at room temperature. The surface tension and the dynamic viscosity of the solutions were measured with the less than 10% uncertainty using a tensionmeter and a viscometer. The test conditions used in this study are shown in Table 2-1.

2.4.3 Aerated Liquid Jets in Crossflow

Operating condition for aerated liquid jet in subsonic crossflow is shown in Table 2-2. An aerated injector with the exit diameter of 1 mm was tested at the GLR of 8%. To maintain a GLR of 8%, a water flow rate of 1.45cc/s and an air flow rate of 103cc/s were used. The injection pressure of 1.1MPa was used for the aerating gas and the liquid. The properties of the water used for aerated liquid jet were as follows: density = 999 kg/m^3, surface tension = 0.00734 N/m, kinematic viscosity = 1.12 x 10-6 m^2/s. To hold the jet-to-freestream momentum flux ratio (q_o) at 0.74, the wind tunnel was set to a speed of u_∞ = 61 m/s. The averaged jet velocity was 30.0 m/s, and free stream Mach number (M) was 0.18.

Holograms were digitally recorded at the range of x/d_o= 0 ~ 22.5 and y/d_o= 0 ~ 27 to probe the near injector region of the aerated liquid jet. The field of view of the

37

holograms with high resolution was 9 mm × 9 mm. To overcome this limited field of view, the dense spray region of x/d_o= 0 ~ 22.5 and y/d_o= 0 ~ 27 was divided into several investigation windows. At each of the investigation windows holograms were recorded starting at the top of the test section and then moving the CCD sensor and the objective lens down in 9 mm increments which is the height of the CCD sensor. The CCD sensor continued to be lowered until no more droplets appeared.

After the holograms were digitally recorded, they were then reconstructed at spanwise distances at increments of ± 0.17 mm throughout the spray volume. The reconstruction range was determined such that it could cover all the droplets in the spray at that particular location. The maximum range of reconstruction depth of spanwise direction was ± 13mm. In each of the reconstruction holograms the focused droplets were used to measure droplet diameters, locations, and three-dimensional velocities. The SMD was then calculated by averaging the droplet diameters over five spanwise incremental distances equaling 0.83 mm.

2.5 Validity of the DMH in the Near Injector Region

2.5.1 Hologram Reconstruction

A single pulse hologram for 100 µm liquid jet generated with injection pressure of 345 kPa was digitally recorded by commercial grade CCD (Nikon D-70) and numerically reconstructed. Figure 2-13(a) shows the recorded hologram which was obtained using a 5x objective lens and a pinhole of 15 µm. The distance from the light source to the micro liquid jet was 550 mm, and the distance between the jet and CCD was 220 mm. The

black area at the top of the hologram is the edge of the injector. Figure 2-13(b, c, and d) shows the reconstructed two-dimensional images at depth of 301mm, 306mm, and 311mm, respectively. These images have been cropped for clarity, but the original images were squares with size of 2000×2000 pixels. The images reconstructed at 301mm and 306mm are visible but out of focus. However the image reconstructed at 311mm is focused and the edge of the liquid jet is very sharp. These reconstructed images demonstrate how the droplets come into focus at different depths. In addition, the image reconstructed at a depth of 311 mm shows that liquid jet is straight because the column as a whole is well focused at a specific distance from the CCD.

2.5.2 Velocity Measurement

The reconstruction of a double-pulsed hologram captured on the same frame using a commercial-grade CCD camera is shown in Figure 2-14. The time interval between the double pulses was controlled by a pulse generator and measured by a photo detector and an oscilloscope as 4 μs. For velocity measurement the displacement of the drops between the double pulses was determined with the center of mass of drops, and divided by the time interval between the pulses. The displacement in mm was determined using the scale calibration graph. The velocities of the drops were measured with uncertainty of less than 10% in all cases. The drop velocities increased with the increase in injection pressure as shown in Figure 2-15. Velocities measured by DMH were almost similar to the assumed jet velocity given by the Bernoulli equation (2-3) (Munson et al., 2006):

$$V_j = (2\Delta P/\rho)^{1/2} \qquad\qquad (2\text{-}3)$$

where ΔP is pressure difference across the nozzle and ρ is the liquid density. The assumption of Equation 2-3 are incompressible fluid, very thin walled orifice, and negligible viscous losses

2.5.3 Breakup of Liquid Jets in the Near Injector Region

The different breakup modes of micro liquid jets for jet exit Reynolds numbers (Re_L) ranging from 2500 to 5800 and jet exit Weber number (We_L) ranging from 900 to 4900 are shown in Figure 2-16 (a~f). The breakup structures of micro liquid jets for the variation of jet exit Weber numbers were different due to the effects of increases in the velocities of liquid discharge as shown in Figure 2-16 (a~f). Figure 2-16 (a) shows the capillary structure with axisymmetric wave. The liquid jets become more deformed with the increase in jet exit Weber number. The breakup of micro liquid jet in still air was characterized by rapid fluctuations of the jet cross sectional area as shown in Figure 2-16 (b~f). The bag breakup mode of macro liquid jet in gaseous crossflow ($We_\infty=8$) is shown in Figure 2-17 (a). Present micro liquid jet in gaseous crossflow ($We_\infty=13$) experiences bag breakup as shown in Figure 2-17 (b). This bag breakup mode is similar to that of macro liquid jets in crossflow with the formation of bag-drops with diameters $\approx 10\%$ of jet diameter for $We_\infty>5$.

2.6 Uncertainty Analysis of Single view DMH

2.6.1 General formulation

There are four kinds of experiments for measurement uncertainty analysis, which are the single measurement measurand experiment (e.g. a single measurement of pressure), the

single measurement result experiment (e.g. a single velocity measurement of an object on the basis of time and displacement measurements), the multiple measurement measurand experiment that determines averaged value with many repeated measurements (e.g. the mean pressure determined from the repeated measurements), and the multiple measurement result experiment (e.g. the mean surface tension of a liquid determined by the repeated surface force and length measurements) (Dunn, 2005). In the present study, all the measurements were conducted at least three times under the same operating conditions. The uncertainties from the repeated measurements were determined by the analysis of Crow et al. (1960) on the basis of the t-distribution. By assuming that the sample is a random one with the measurements following a normal distribution, the uncertainties can be calculated using the following equation:

$$u = \pm t_{\alpha/2, n-1} \frac{s}{\sqrt{n}} \qquad (2\text{-}4)$$

where s is standard deviation, n is the number of samples of data, t denotes the t-distribution, and $(1-\alpha)$ is the confidence level. All the uncertainties reported in the present study are taken at 95% confidence level.

Uncertainties resulting from the image analysis of reconstruction holograms have been performed on the basis of the single measurement analysis of Moffat et al. (1985). In the analysis, variables Z consist of functions of n other independent variables, z_i, as follows;

$$Z = f(z_1, z_2, z_3, \cdots\cdots, z_i) \tag{2-5}$$

The uncertainty of the result Z is then given by the following expression;

$$\frac{\Delta Z}{Z} = \left[\sum_{i=1}^{n} \left(\frac{\partial \ln Z}{\partial z_i} \Delta z_i \right)^2 \right]^{\frac{1}{2}} \tag{2-6}$$

when Δz_i is the uncertainty value of a variable z_i. The overall uncertainty of Z depends on the individual uncertainty of each measured variable, Δz_i. All the uncertainties measured in the present study are taken to be those for the 95% confidence level.

2.6.2 Spatial calibration uncertainties

All the measured quantities should be compared with a true, known value for the accuracy of the measurement. In the present study, systematic errors that arose from the image analysis process could be reduced using the spatial calibration. All measurements of reconstruction holograms were at first performed in pixel dimension, but converted to metric dimension using the spatial calibration. The reconstruction distances could be calibrated into actual distance in spanwise direction by the spatial calibration. Two conversion factors are needed for the spatial calibration. A conversion factor, R, is given by the following equation.

$$R = \frac{D_m \, (\mu m)}{D_p \, (pixels)} \tag{2-7}$$

where D_m is the known pin diameter measured in metric dimension and D_p is the diameter measured by counting the pixel numbers of calibration pin images focused at each different spanwise distance. The factor, R, is the function of the reconstruction distance (or spanwise distance) because of the use of the expanding laser beams. The uncertainty of the conversion factor, R, varied with the different reconstruction distances as shown in Figure 2-18. The uncertainties of the conversion factor, R, for different spanwise locations were determined by the following equation.

$$\Delta R/R = -0.0085X + 2.2366 \qquad (2\text{-}8)$$

where X is the reconstruction distance (mm). The other conversion factor, S, is the ratio of the gap distance between each pin to the difference between reconstruction distances where each pin was focused.

$$S = \frac{G_m(\text{mm})}{G_R(\text{mm})} \qquad (2\text{-}9)$$

G_m is the known gap distance between each calibration pin and G_R is the reconstruction distance difference between the planes where each pin was focused. The conversion factor, S, resulted from the numerical reconstruction program. The distance from the CCD sensor to the objective lens is used for the numerical reconstruction process. Without the accurate measurement of the distance in millimeters, the reconstruction distances produced during the numerical reconstruction process would be incorrect. The

43

factor, S, was used for the conversion of the reconstruction distance to actual distance in the spanwise direction (normal to camera) and determined the accuracy of measurement of droplet locations in spanwise direction. The uncertainty of R is estimated from 1.56 to 1.64% within the given reconstruction distance ranges from 70 to 79 as shown in Figure 2-16.

2.6.3 Spherical drop size uncertainties

The diameter of a spherical droplet is given by the following equation

$$d_m \, [\mu m] = f \, (d_p \, , \, R) = d_p \, [\text{pixels}] \times R \, [\mu m/\text{pixels}] \qquad (2\text{-}10)$$

where d_m is diameter in metric dimension, d_p is the diameter in pixels. Applying Equation 2-6, the overall uncertainty of a spherical droplet can be obtained using the following equation:

$$\frac{\Delta d_m}{d_m} = \left[\left(\frac{\partial \ln(d_m)}{\partial d_p} \Delta d_p \right)^2 + \left(\frac{\partial \ln(d_m)}{\partial R} \Delta R \right)^2 \right]^{\frac{1}{2}} \qquad (2\text{-}11)$$

The measurement error of ±1 pixel on each boundary was indicated with repeated measurements of the size of a single drop. Thus, the error results in an uncertainty of ±2 pixels in the diameter measurement.

$$\frac{\Delta d_m}{d_m} = \left[\left(\frac{\pm 2}{d_p} \right)^2 + \left(\frac{\Delta R}{R} \right)^2 \right]^{\frac{1}{2}} \qquad (2\text{-}12)$$

The overall of uncertainty of Δd_m then becomes:

$$\Delta d_m = \left[\left(\pm 2R \right)^2 + \left(d_p \cdot \Delta R \right)^2 \right]^{\frac{1}{2}} \qquad (2\text{-}13)$$

The uncertainty in size measurements of a drop is affected by the uncertainty of the calibration measurement as shown in Equation 2-13. The uncertainty given by Equation 2-13 can be used to calculate the volume-averaged uncertainty of the spherical droplet size measurements.

2.6.4 Equivalent drop size measurement

Most droplets are non-spherical in dense spray region near the injector. In the present study, the non-spherical droplets were assumed to be ellipsoidal droplets and measured with major and minor axes in pixels. For the three dimensional drop distribution the spherical equivalent diameter was used. The equivalent spherical diameter was determined with the diameter of a circle with the same area as an ellipsoidal drop. The equivalent diameter of a drop is given by the following equation

$$d_{eq.m} \, [\mu m] = f(d_{1p}, d_{2p}, R) = R(d_{1p} \times d_{2p})^{1/2} \qquad (2\text{-}14)$$

where $d_{eq.m}$ is an equivalent drop size in metric dimension, and d_{1m} and d_{2m} are respectively the major and minor diameters of an elliptic drop in metric dimension. Applying Equation 2-6, the overall uncertainty of the equivalent diameters can be obtained using the following equation:

$$\frac{\Delta d_{eq.m}}{d_{eq.m}} = \left[\left(\frac{\partial \ln(d_{eq.m})}{\partial d_p} \Delta d_p \right)^2 + \left(\frac{\partial \ln(d_{eq.m})}{\partial R} \Delta R \right)^2 \right]^{\frac{1}{2}} \qquad (2\text{-}15)$$

The measurement error of ±1 pixel on each boundary was indicated with repeated measurement of the size of a single drop. Thus, the error results in an uncertainty of ±2 pixels in the diameter measurement.

$$\frac{\Delta d_{eq.m}}{d_{eq.m}} = \left[\left(\frac{1}{d_{1.p}} \right)^2 + \left(\frac{1}{d_{2.p}} \right)^2 + \left(\frac{\Delta R}{R} \right)^2 \right]^{\frac{1}{2}} \qquad (2\text{-}16)$$

The average uncertainty obtained by Equation 2-16 was 9.8% and the maximum and minimum uncertainties in the equivalent drop size measurements were 36% and 3%, respectively. The overall of uncertainty of $\Delta d_{eq.m}$ then becomes:

$$\Delta d_{eq..m} = \left[\frac{d_{2.p}}{d_{1.p}} R^2 + \frac{d_{1.p}}{d_{2.p}} R^2 + d_{1.p} \cdot d_{2.p} \cdot \Delta R^2 \right]^{\frac{1}{2}} \qquad (2\text{-}17)$$

46

The uncertainty obtained by Eq. 2-17 was used to calculate the uncertainty representative (volume-averaged equivalent uncertainty) of the equivalent drop size measurement.

$$\overline{\Delta d_{eq..m}} = \frac{\sum_{i=1}^{n} d_i^3 \Delta d_{eq..m.i}}{\sum_{i=1}^{n} d_i^3} \qquad (2\text{-}18)$$

where n denotes total number of drops measured. The maximum volume-averaged uncertainty calculated by Equation 2-18 was found to be approximately 6 µm.

2.6.5 Drop position uncertainty

The drop locations in streamwise and cross-stream directions were measured relative to the tip of the aerated liquid injector, and have the same uncertainties as the spherical drop diameter measurement. The maximum and minimum uncertainties in drop location measurement were 8% and 1.6%, but the average uncertainty was 1.7%. The drop locations in spanwise direction (normal to camera) were determined by the reconstruction distance in which the drop appears in focus on the reconstruction hologram. The uncertainty of drop location measurements in spanwise direction is related to the minimum reconstruction distance used in the present study for the drop position measurements. The minimum change of the reconstruction distance was 0.167 mm. Thus, the uncertainty of droplet locations in spanwise direction would be at least ±167 µm and the average error of the spanwise displacement of the drops was found to be 33%. The uncertainty of drop locations can be neglected due to the large values of x/d_o employed in the present study.

2.6.6 Drop velocity uncertainty

Three dimensional velocities of the spherical drops (streamwise, cross-stream, and spanwise velocities) were calculated by the following equation. The cross-stream velocity was calculated by the following equation.

$$u_m \ (m/s) = \frac{d_m}{\Delta t} = \frac{d_p \times R}{\Delta t} \tag{2-19}$$

where u_m is cross-stream velocity in metric dimension. The pulse separation time, Δt, was determined with an oscilloscope and a photo detector. The error in measuring a pulse spacing of $47\mu s$ was negligible in the present measurements. Therefore, the uncertainty in measurements of the three dimensional velocities is the same as the droplet position uncertainty. The drop positions in the streamwise and cross-stream directions were measured relative to the tip of the aerated injector, and have the same uncertainties as the spherical droplet diameter. The overall uncertainty of cross-stream velocity was calculated by the following equation.

$$\frac{\Delta u_m}{u_m} = \left(\left(\frac{2}{d_p} \right)^2 + \left(\frac{\Delta R}{R} \right)^2 \right)^{1/2} \tag{2-20}$$

The maximum uncertainty of cross-stream velocity was 2% and the average uncertainty was 1.9%. The same process can be applied to the streamwise and spanwise velocities of

droplets. The maximum uncertainty of streamwise velocity was 7% and the average uncertainty was 2.0%. However, the average uncertainty of spanwise velocities was 33%.

$$\Delta u_m = \left(\left(\frac{2R}{\Delta t} \right)^2 + \left(\frac{d_p}{\Delta t} \Delta R \right)^2 \right)^{1/2}$$

(2-21)

The volume-averaged uncertainty of the cross-stream velocities was calculated by Eq. 2-21. The volume-averaged uncertainty is the uncertainty representative of velocities for the entire drop size distribution at a specific position. The volume-averaged uncertainty of the cross-stream velocities was found to be approximately $\pm$ 0.35m/s (8% max). The same process applied to the streamwise velocities and the volume-averaged uncertainty of streamwise velocities was found to be approximately $\pm$ 0.38m/s (5% max).

2.6.7 Sauter mean diameter uncertainty

The SMD of a drop size distribution is a diameter which is defined by the following equation:

$$SMD = \sum_{i=1}^{n} d_{eq.i}^3 \Bigg/ \sum_{i=1}^{n} d_{eq.i}^2$$

(2-22)

By Equation 2-7, the uncertainty of SMD becomes:

$$\frac{\Delta \text{SMD}}{\text{SMD}} = \left[\left(\frac{\partial(\ln\text{SMD})}{\partial d_{eq.p}}\Delta d_{eq.p}\right)^2\right]^{1/2} \qquad (2\text{-}23)$$

From Equation 2-23,

$$\frac{\partial(\ln\text{SMD})}{\partial d_{eq.p}} = \frac{3}{\text{SMD}} - 2\sum_{i=1}^{n}d_{eq.pi}^3 \bigg/ \sum_{i=1}^{n}d_{eq.pi}^2 \qquad (2\text{-}24)$$

The uncertainties from the image analysis could be quantified at each position in the spray, yielding a maximum uncertainty of the SMD of approximately 20%. However there exists another uncertainty source due to finite sample sizes. Thus, the overall uncertainty of SMD becomes:

$$\frac{\Delta \text{SMD}}{\text{SMD}} = \left[\left(\frac{\partial(\ln\text{SMD})}{\partial d_{eq.p}}\Delta d_{eq.p}\right)^2 + \left(\left(\frac{\Delta \text{SMD}}{\text{SMD}}\right)_{sample}\right)^2\right]^{1/2} \qquad (2\text{-}25)$$

where $(\Delta \text{SMD}/\text{SMD})_{sample}$ is the uncertainty resulting from the finite sample sizes. To quantify the uncertainty from the finite sample sizes, the SMD measurements were repeated four times for the near-injector region. The maximum uncertainty from four samples was calculated by Equation 2-4. The maximum uncertainty in the repeated SMD measurements for the near-injector region was 8.1%. Thus, the overall maximum uncertainty of SMD was found to be approximately 21.5%.

When it comes to the number density of the drops in a measuring volume, another uncertainty source exists. The uncertainty results from the lack of data due to the limited depth-of-focus (DOF) in spanwise direction. In digital inline holography (DIH), the depth-of-focus can be determined by the following relationship, which is defined as the distance in which the drop image would appear sharp enough for a good size measurement (Meng et al., 2004 and Vikram, 1992).

$$\tau \sim \frac{d^2}{\lambda} \qquad (2\text{-}26)$$

where d and λ are the droplet diameter and the laser wavelength, respectively. For instance, a droplet diameter of 50 µm and a wavelength of 532 nm result in τ of ~ 4.7mm, or 94d. The depth-of-focus, however, of the digital microscopic holography (DMH) is at least one order of magnitude smaller than that of the inline digital holography (Sheng et al., 2006). They found that the depth-of-focus decreased from 10 to 2 particle diameters with the increase in the magnification using objective lenses of 10x, 18x, and 40x. The depth-of-focus decreased from 4 µm to 2.5 µm with the decrease in the particle diameter for particle diameters of 3 µm and 0.75 µm at 40x magnification. The smallest drop diameter measured in the present study was 16 µm with a depth-of-focus of 180 µm using 5x magnification. Some of the drops with diameters less than 14 µm could have been measured incorrectly because their depth of focus corresponds to the reconstruction distance increments employed in the present study in spanwise direction (167µm). However the present SMD measurements were scarcely affected by such small drops because the SMD for each location ranged from 57 to 100 µm.

2.7 Double view DMH

The single view DMH worked well for the measurements of droplet sizes, locations, and velocities in streamwise and cross-stream directions, but increased uncertainties in measurements of droplet locations and velocities in spanwise direction. To reduce the uncertainties which arise from the measurements in spanwise direction, the depth-of-focus of reconstructed objects should be decreased and smaller reconstruction increments should be used in the spanwise distance. Accurate measurements of three dimensional droplet locations and motions can be accomplished by double view DMH.

In the present study, the double view DMH was used to reduce uncertainty in the measurements of the spatial growth of the three dimensional bending instability of electrospinning polymer jets and to increase the spatial resolution in spanwise direction. The spanwise uncertainty of single view DMH was compared to double view DMH.

Front views of the bending instabilities are shown in Figure 2-19 for the following test conditions: (a) 0.5% PEO solution and (b) 2.0% PEO solution at 5 kV applied voltage and zero injection pressure. The black parts of the (a) and (b) are the Talyor cones on the nozzle tips, and the electrospinning jets move down. The original holograms were recorded with the field of view of 9.35×9.35 mm^2 during the laser pulse duration of 10ns. The front views shown in Figure 2-19 are made by patching many reconstruction holograms focused at different spanwise distances. Three dimensional trajectory of the polymer jet could be measured with the single view hologram as shown in Figure 2-20. The uncertainty in the spatial measurements was found to be approximately 2% for the

front view and 30% for the span view. To reduce the uncertainty in the span view direction, orthogonal double view holograms were simultaneously recorded using the double view optical setup shown previously in Figure 2-5 at the conditions of 7 kV applied voltage and zero injection pressure. Two CCD sensors of Nikon D-70 and 80 were used to record the holograms. The original holograms were recorded with the field of view of D70 (11.36×11.36 mm^2) and 80 (12.25×12.25 mm^2) during the laser pulse duration of 10ns. Two reconstruction holograms of double view DMH are shown in Figure 2-21. Three dimensional trajectories of polymer jets were tracked with double view holograms and are shown in Figure 2-22. The uncertainty in spanwise direction could be reduced qualitatively as shown in Figure 2-22. The uncertainty of the measurement in spanwise direction was found to be approximately 2%. Additionally, the jet splaying due to the bending instability and the bead formation of polymer jets in-flight are shown in Appendix B.

Table 2-1 Operating conditions for electrospinning process.

PEO(g)	Water(g)	Solution Concentration(%)	Surface Tension (dyne/cm)	Dynamic Viscosity (mm2/s)	Temp. (°C)	Applied Voltage (kV)
0.5	99.5	0.5	61.58	6.46	24	5~10
2	98	2	58.23	126	24	5~10

Table 2-2 Operating conditions for aerated liquid jet.

d_0 (mm)	1.0
M (-)	0.18
q_0 (-)	0.74
GLR (%)	8
x/d_0 (-)	0 ~ 22.5
y/d_0 (-)	0 ~ 27
z/d_0 (-)	-13 ~ 13

Table 2-3 Summary of test conditions for 0.5 mm injector (Miller et. al., 2008).

d_0 (mm)	0.5	0.5	0.5	0.5	0.5	0.5	0.5	0.5
M (-)	0.16	0.16	0.07	0.07	0.16	0.16	0.07	0.07
x/d_0 (-)	25	25	25	25	50	50	50	50
q_0 (-)	0.74	0.74	4	4	0.74	0.74	4	4
GLR (%)	4	8	4	8	4	8	4	8
$Q_{L,injected}$ (cc/s)	0.33	0.33	0.33	0.33	0.33	0.33	0.33	0.33
$Q_{G,injected}$ (cc/s)	10.8	21.7	10.8	21.7	10.8	21.7	10.8	21.7

Table 2-4 Summary of present test conditions for 1.0 mm injector
(Present test conditions and (a) from Miller et al. 2008).

| d_0 (mm)	1.0	1.0	1.0	1.0[a]	1.0[a]	1.0[a]	1.0[a]	1.0[a]	1.0[a]	1.0[a]	1.0[a]
M (-)	0.18	0.18	0.18	0.18	0.18	0.075	0.075	0.18	0.18	0.075	0.075
x/d_0 (-)	0	9	18	25	25	25	25	50	50	50	50
q_0 (-)	0.74	0.74	0.74	0.74	0.74	4	4	0.74	0.74	4	4
GLR (%)	8	8	8	4	8	4	8	4	8	4	8
$Q_{L,injected}$ (cc/s)	1.45	1.45	1.45	1.45	1.45	1.45	1.45	1.45	1.45	1.45	1.45
$Q_{G,injected}$ (cc/s)	103	103	103	49	103	49	103	49	103	49	103
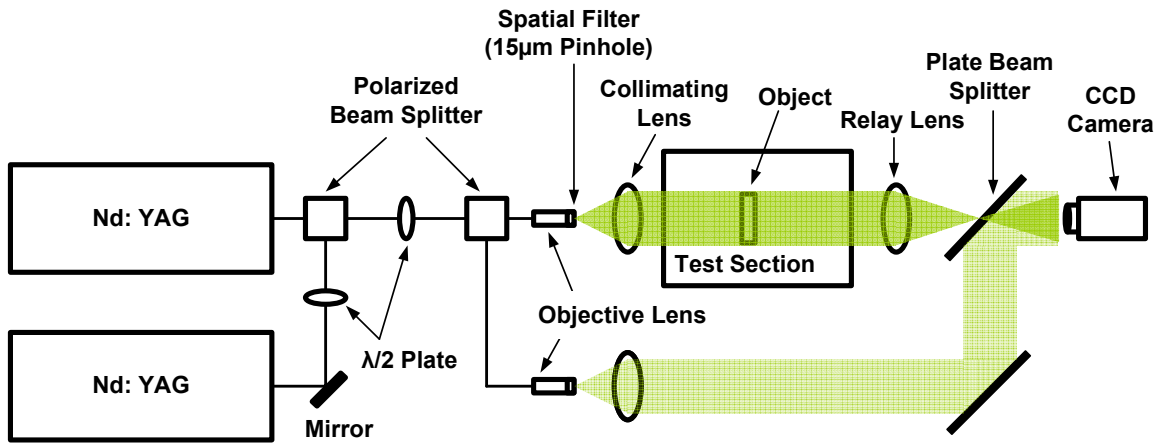
Figure 2-1 Digital in-line holography (DIH) setup with additional reference beam.
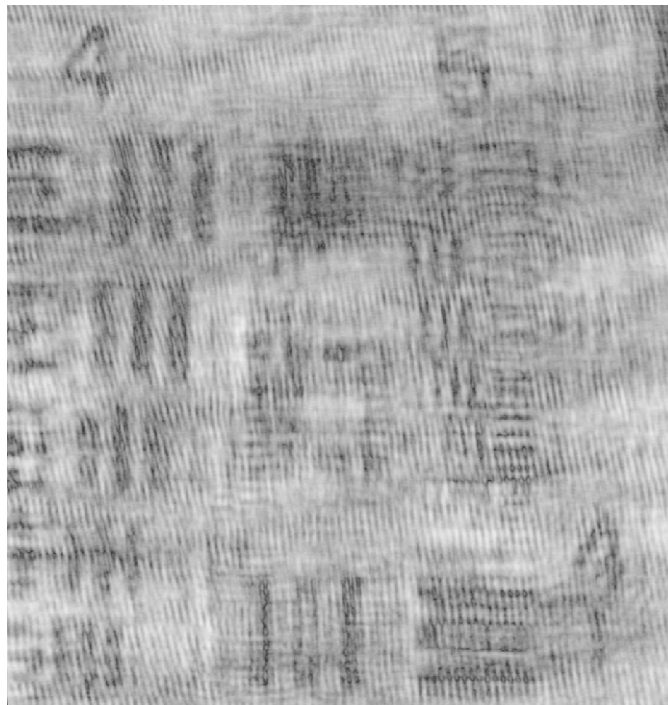

Figure 2-2 Reconstruction of a resolution target using the digital in-line
holographic method with magnification from a relay lens (PCO-2000).
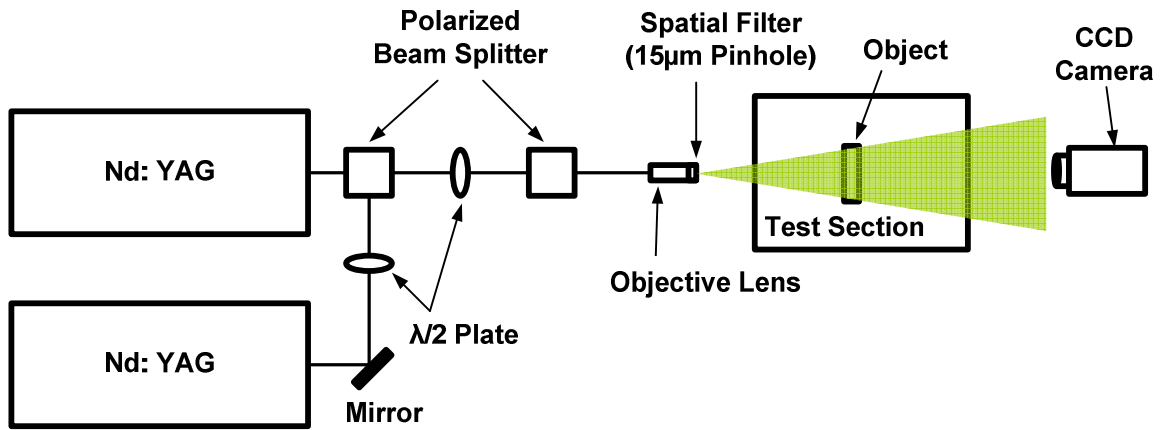
Figure 2-3 Digital microscopic holography (DMH) setup.

<div align="center">(a)   (b)</div>
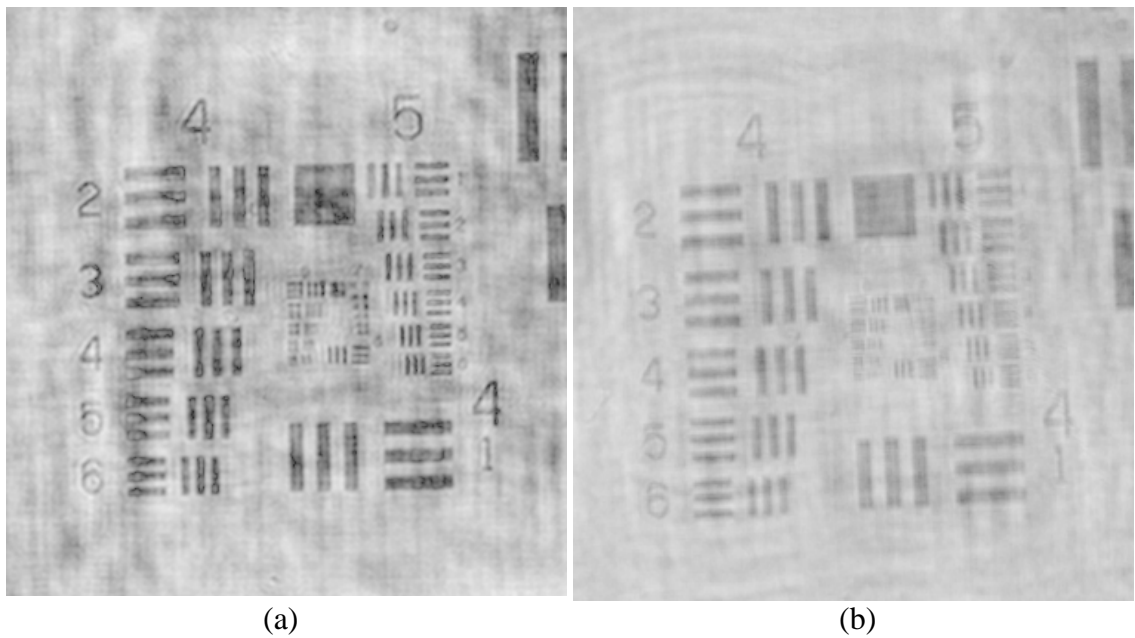
Figure 2-4 Reconstruction of a resolution target using digital microscopic holography method: (a) PCO-2000, (b) Nikon D-70.
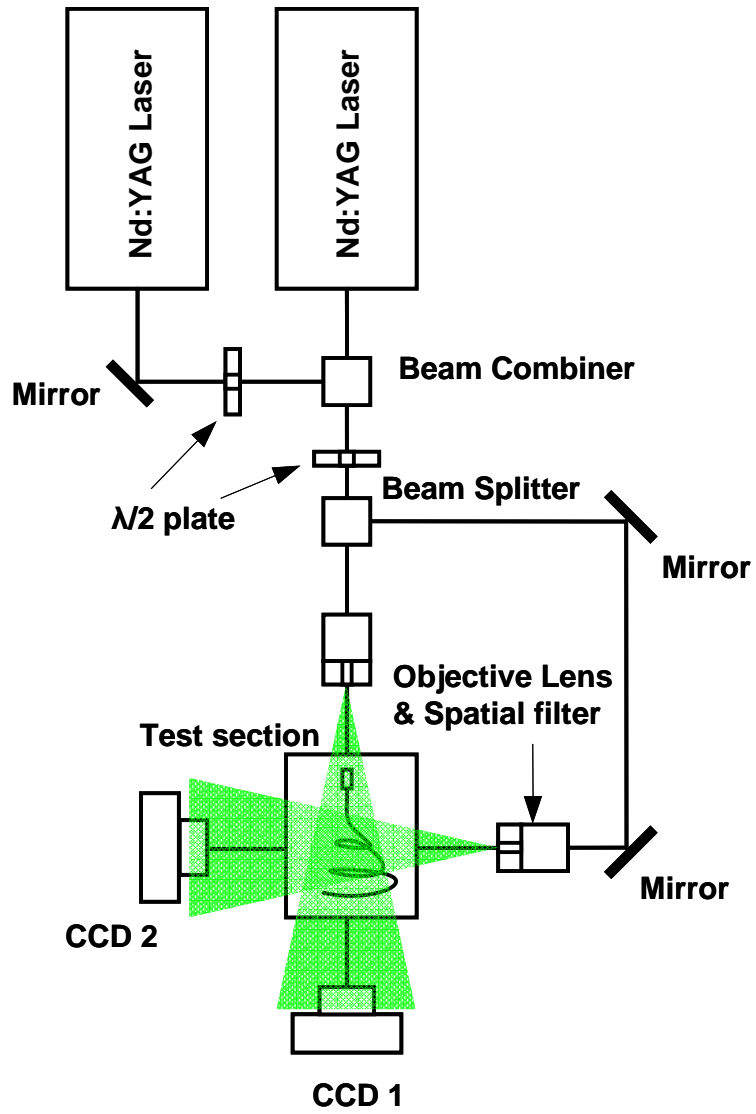
Figure 2-5 Optical setup of double view digital microscopic holography (DMH).

6.35mm 2.032mm

Pipe

Water

Washer → ← Ø 2mm 0.635mm

Rubber sealing ring Ø 2mm

Washer → ← Ø 3mm

Rubber sealing ring 0.635mm

Cap

Orifice with 100µm
hole in the center
Orifice thickness: 0.075mm

Straight Liquid
Jet
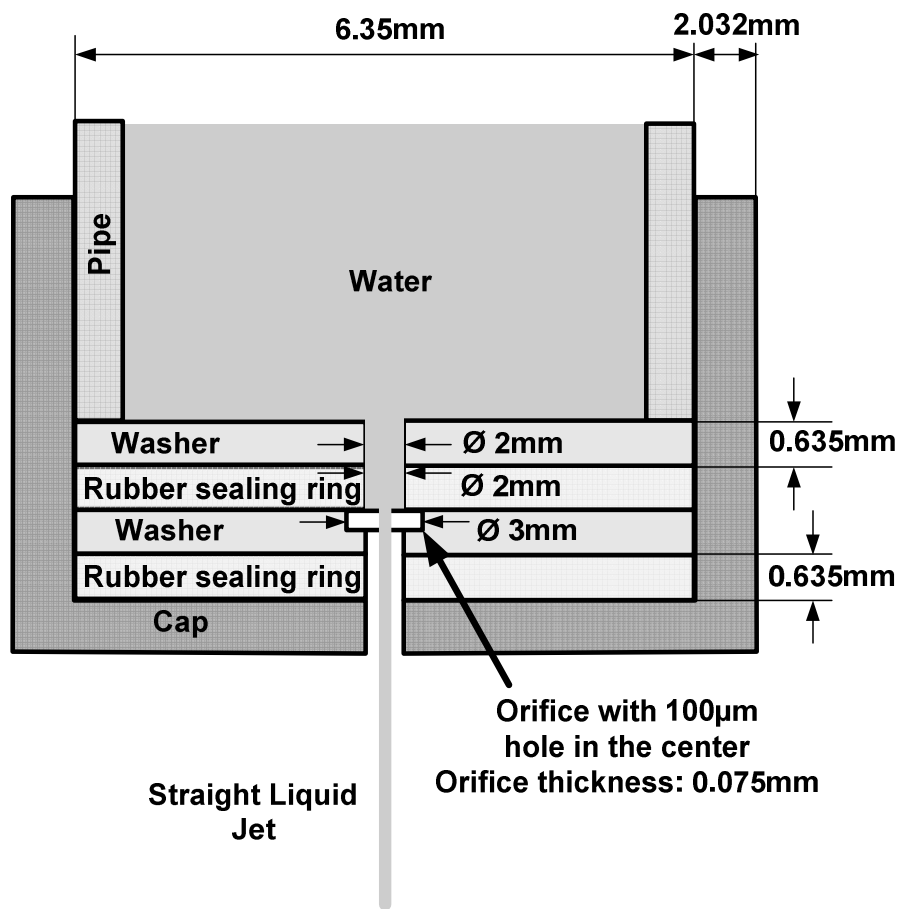
Figure 2-6 Microjet injector
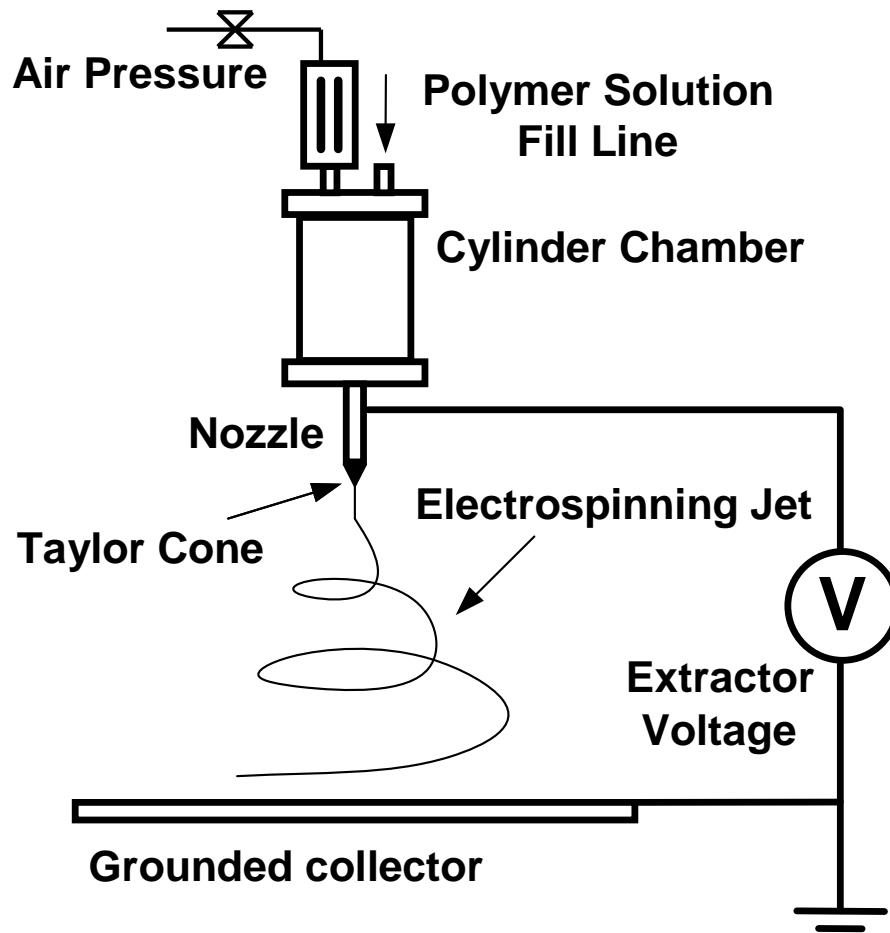
Figure 2-7 Polymer jet during electrospinning process.
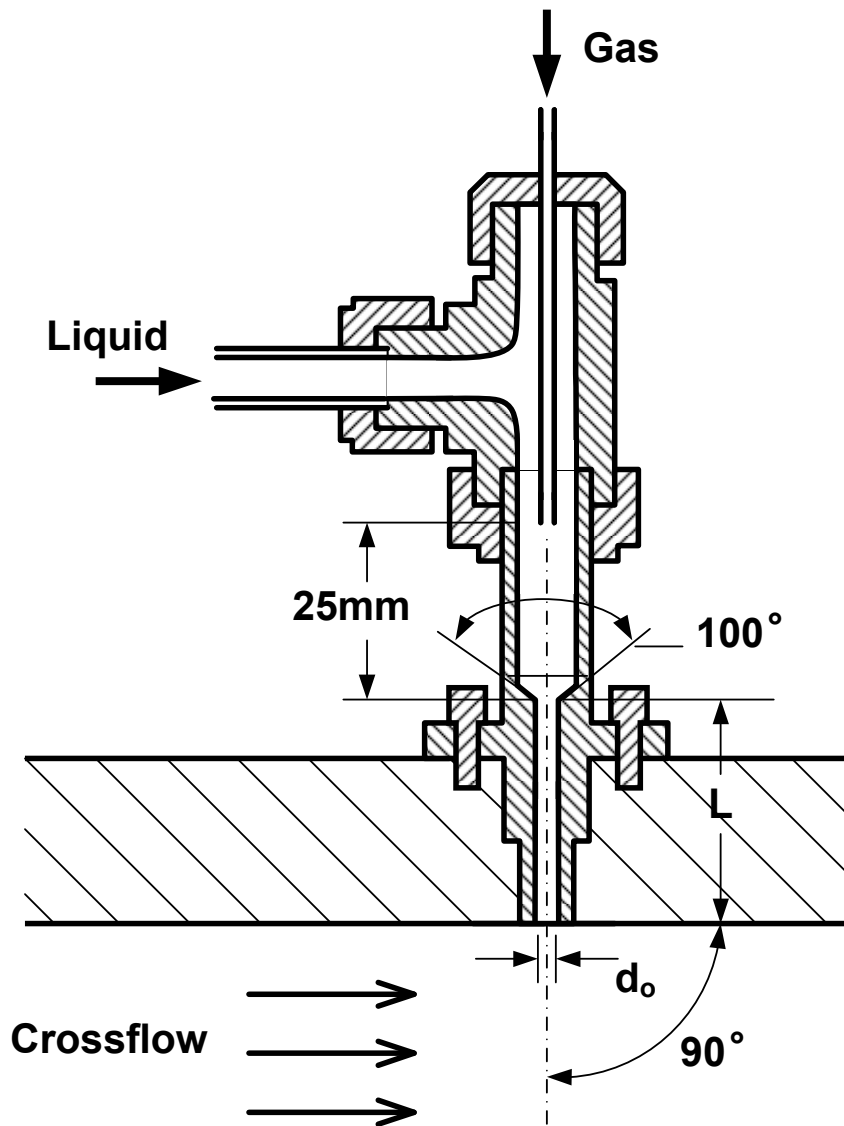
Figure 2-8 Schematic of an aerated injector
(inside out setup shown from Lin et al., 2001).
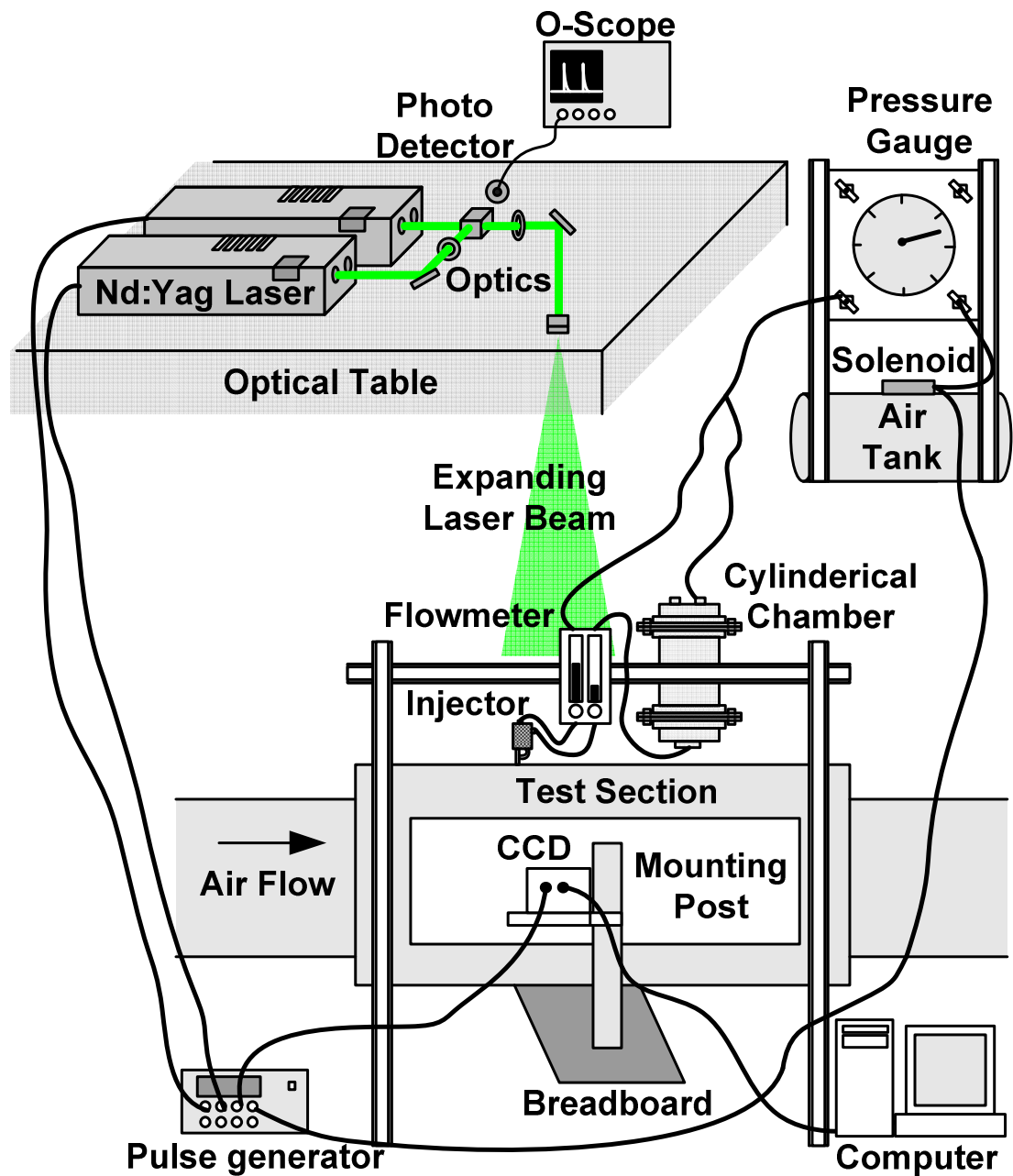
Figure 2-9 Experimental apparatus.
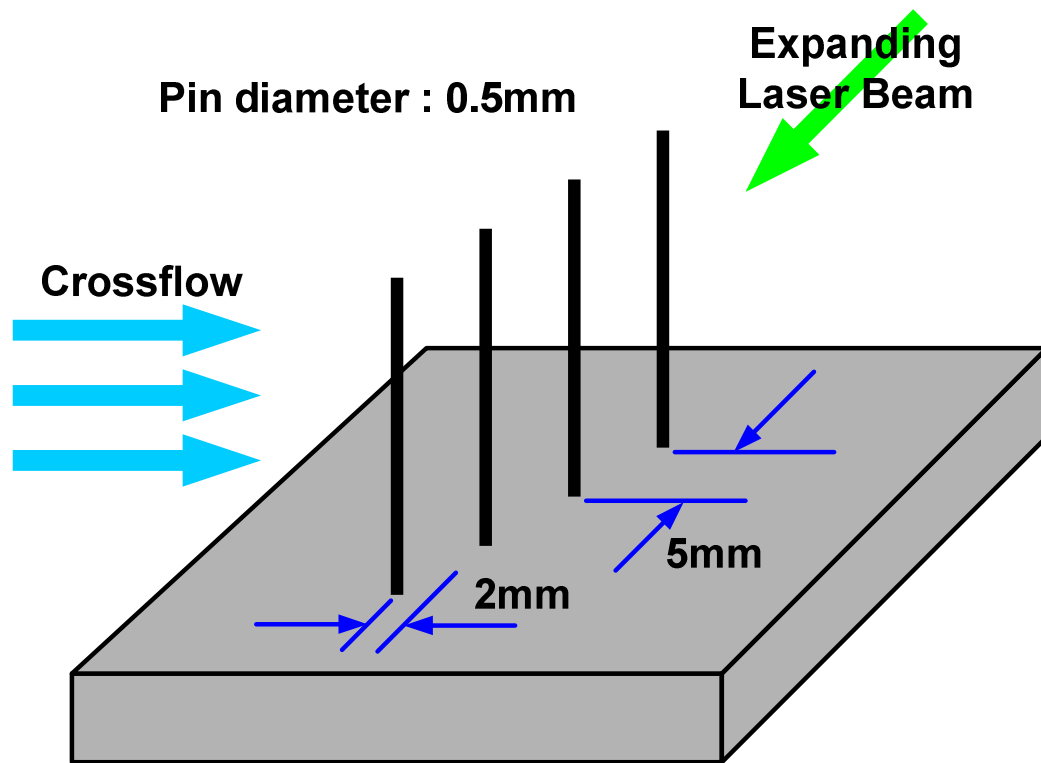
Figure 2-10 Schematic of four pins for spatial calibration.

(a)


79mm   76mm Focused   73mm   70mm
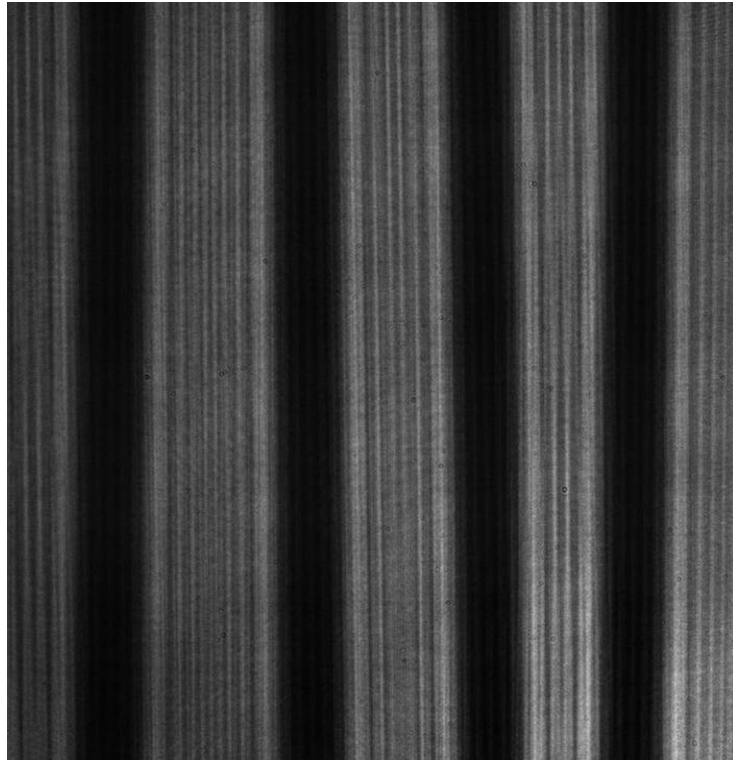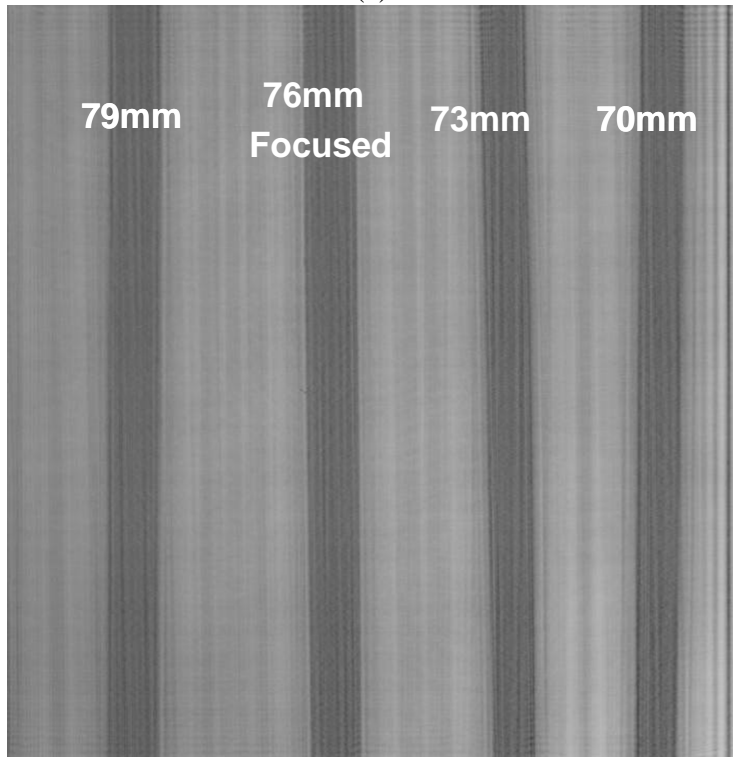
(b)

Figure 2-11 Hologram (a) recorded for spatial calibration and
(b) reconstructed at the spanwise depth of 76 mm from CCD sensor.
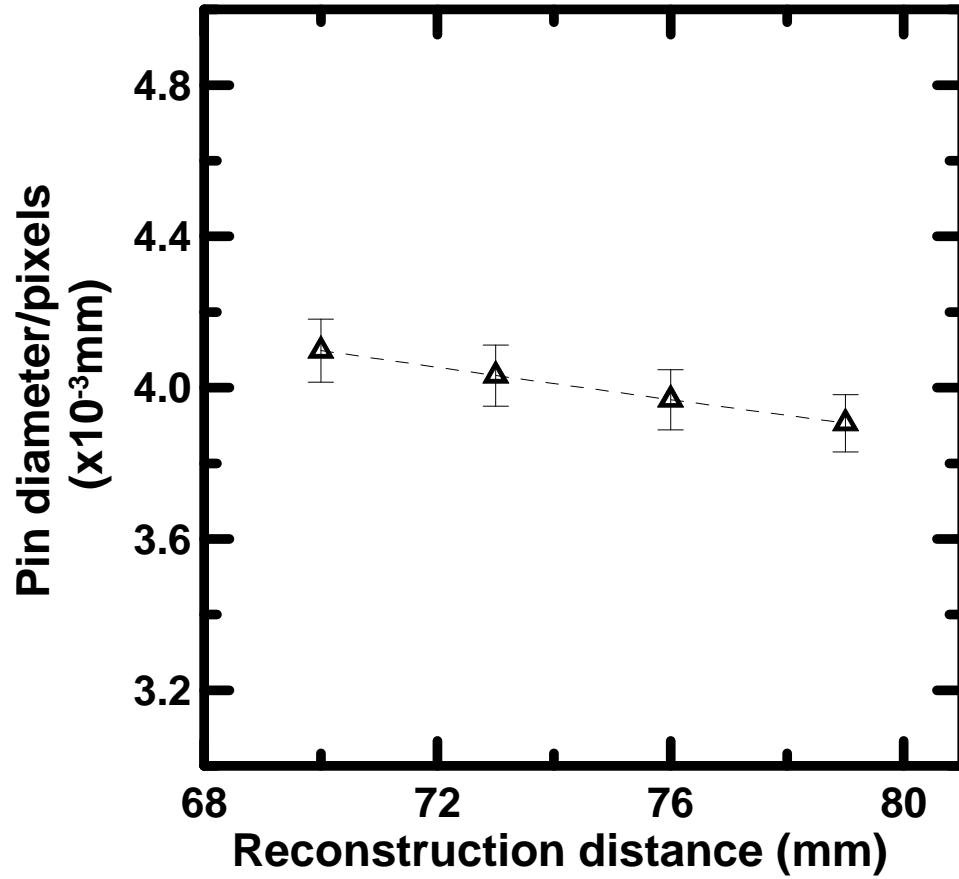
Figure 2-12 Spatial calibration between actual distance and pixel numbers
for all reconstruction distances within the field of view
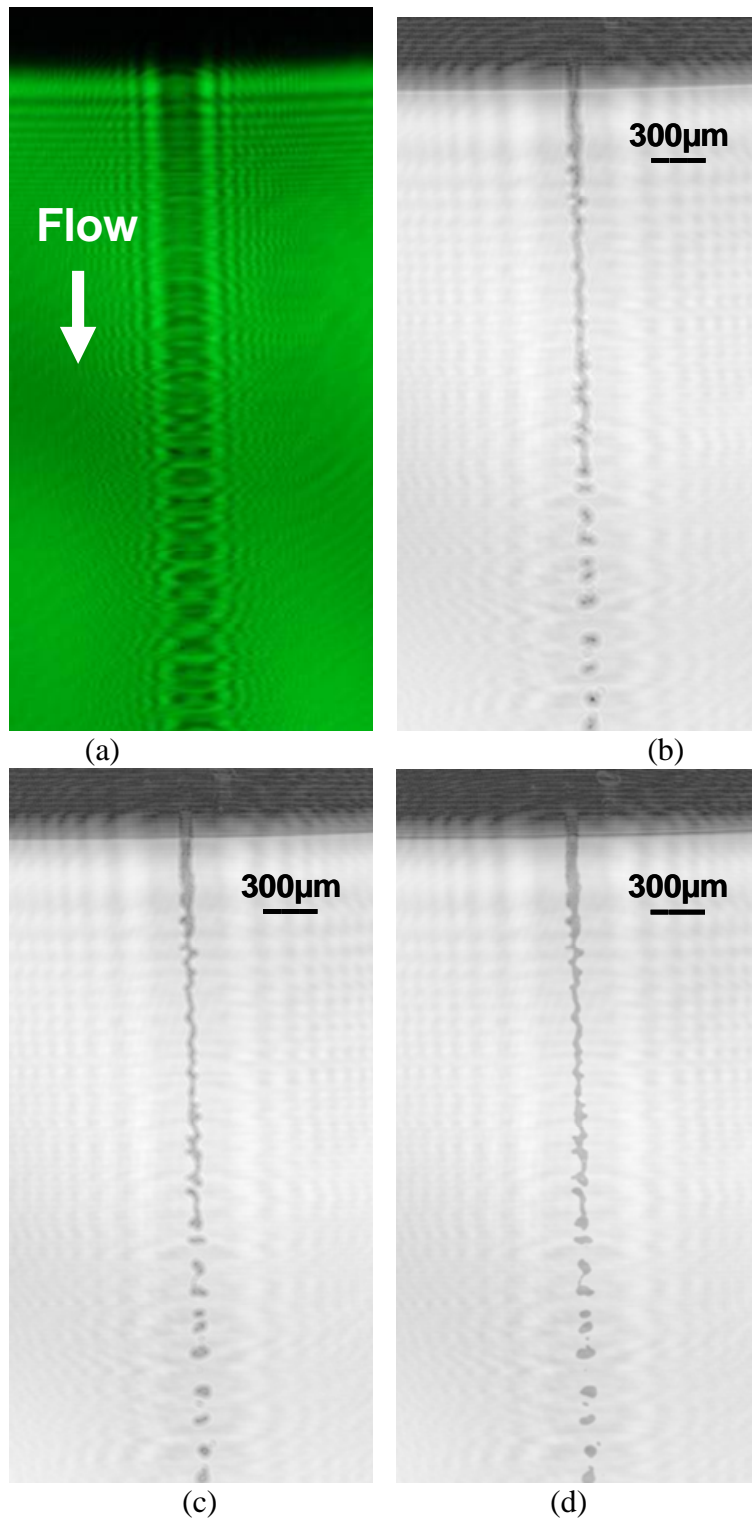
Figure 2-13 Digitally recorded holograms and reconstructed holograms
at different depths. (a) Recorded hologram, (b) Depth: 301 mm,
(c) Depth: 306 mm, and (d) Depth: 311 mm.
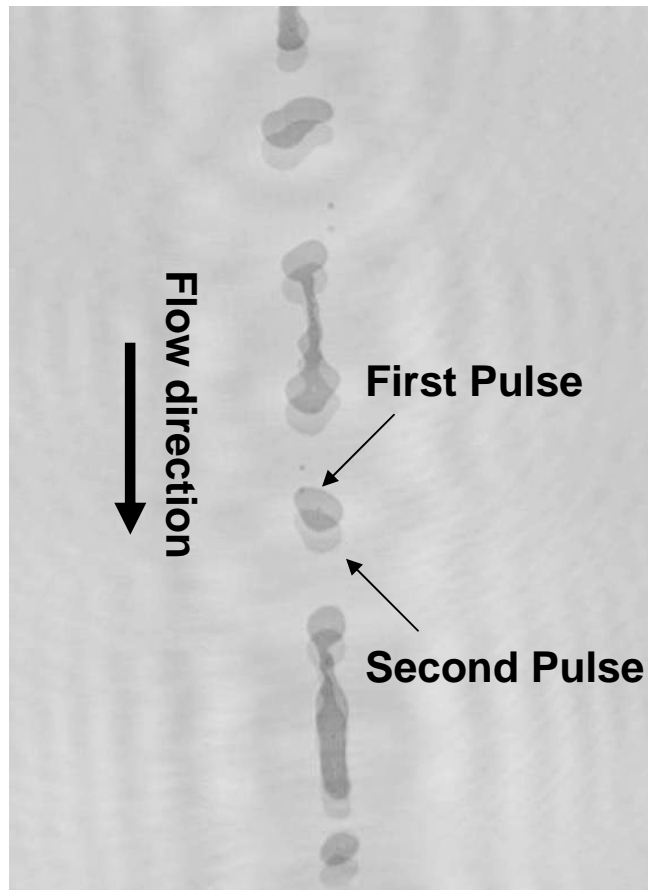
Figure 2-14 Double pulsed reconstructed images on the same frame with 4 µs delay between the two laser pulses (The 100 µm water jet is moving from top to bottom).
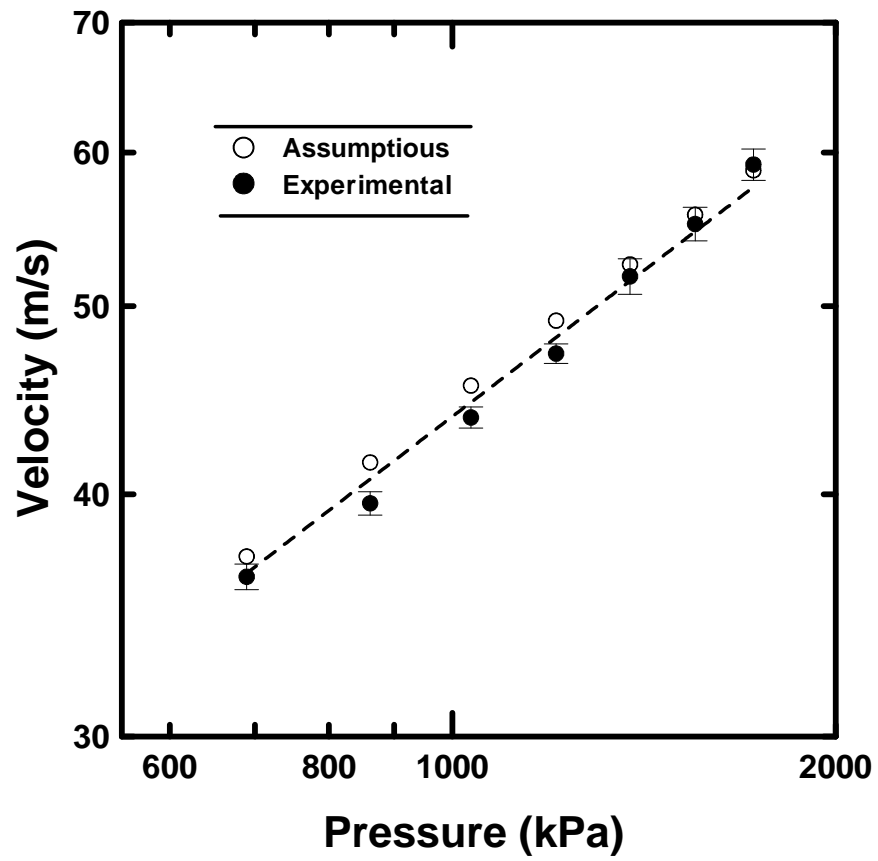
Figure 2-15 Experimental velocities measured by DMH method and
the theoretical velocities for different injection pressures.
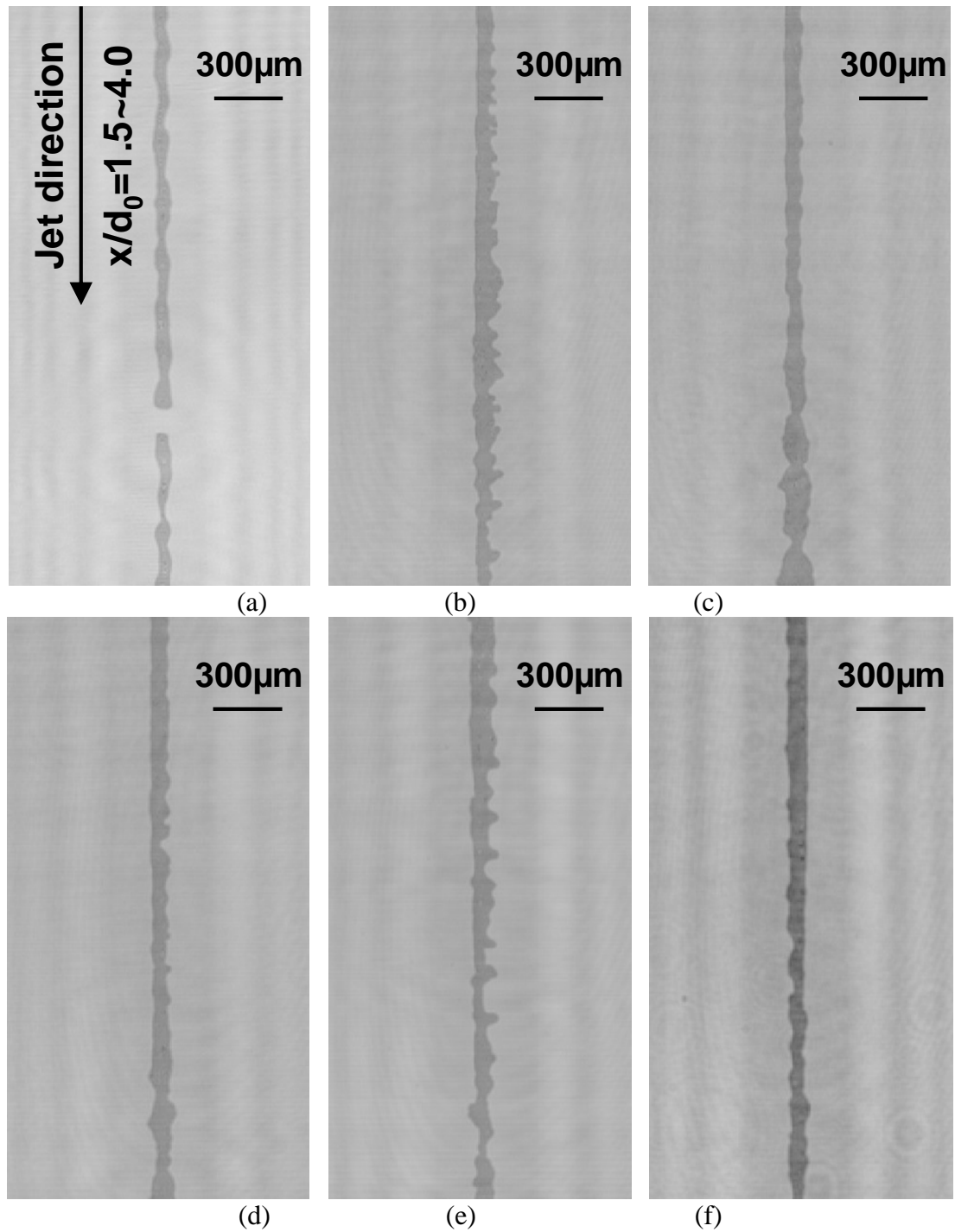
Figure 2-16 Breakup regime of micro liquid jet at the location of $x/d_0 = 1.5 \sim 4.0$
(The 100 μm water jet is moving from top to bottom.): Images (a) through (f) correspond
to $We_L = 900, 3000, 3400, 3900, 4400, 4900$ and
$Re_L = 2500, 4600, 4900, 5200, 5500, 5800$.
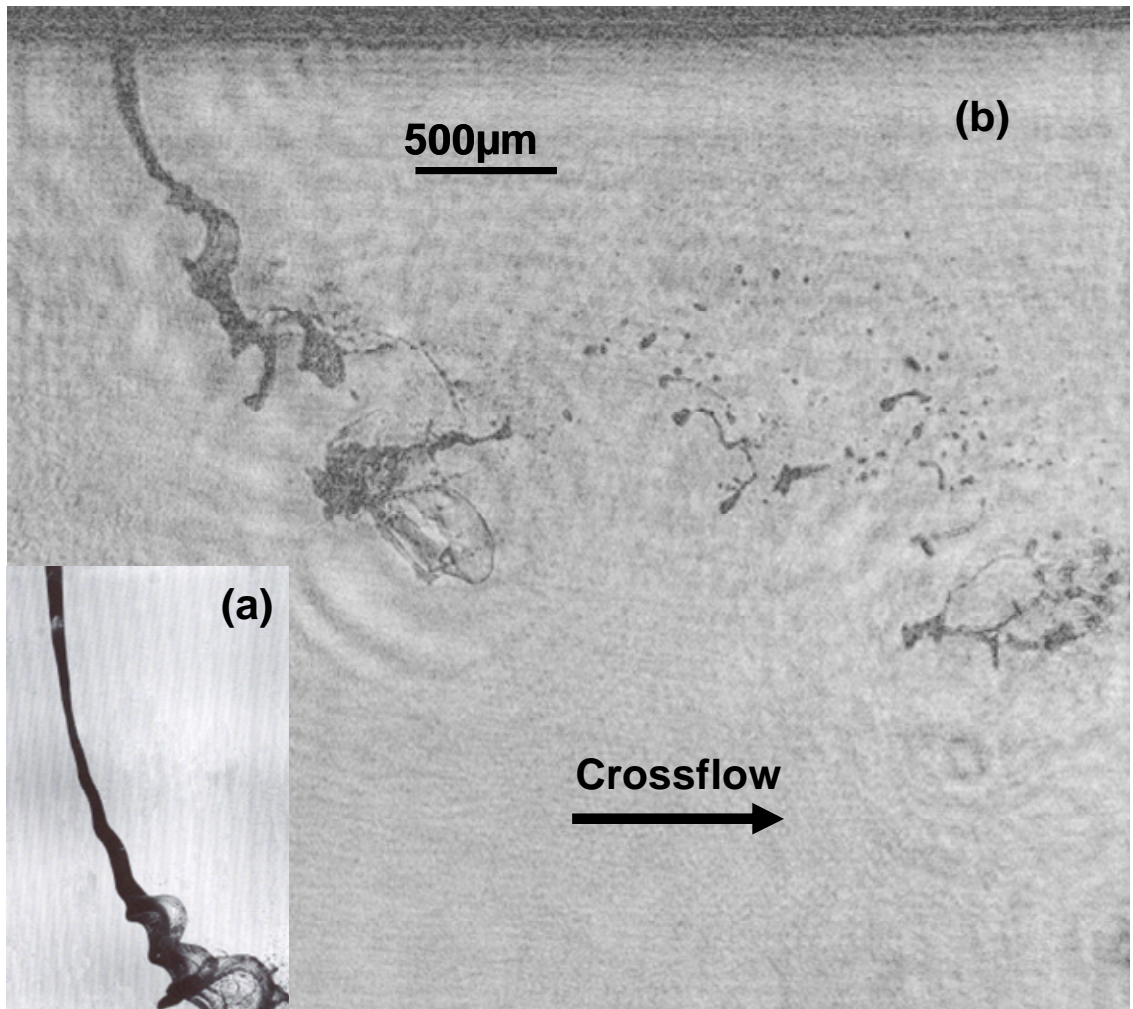
Figure 2-17 Micro liquid jet breakup in gaseous Crossflow:
(a) Sallam et al. ref [13]: d_0= 1 mm, We_∞= 8
(b) present: d_o= 100 μm, We_∞= 13, We_L= 900, Re_L=2500
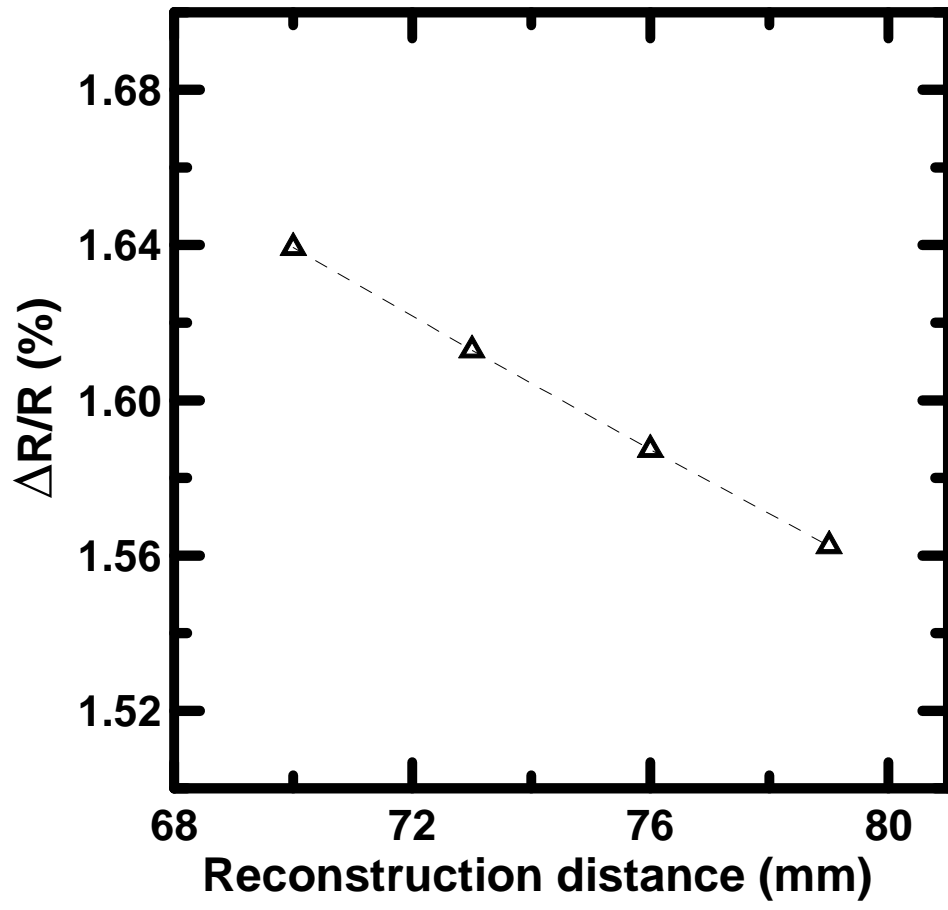
Figure 2-18 Maximum uncertainty of the spatial calibration
for all reconstruction distances within the field of view
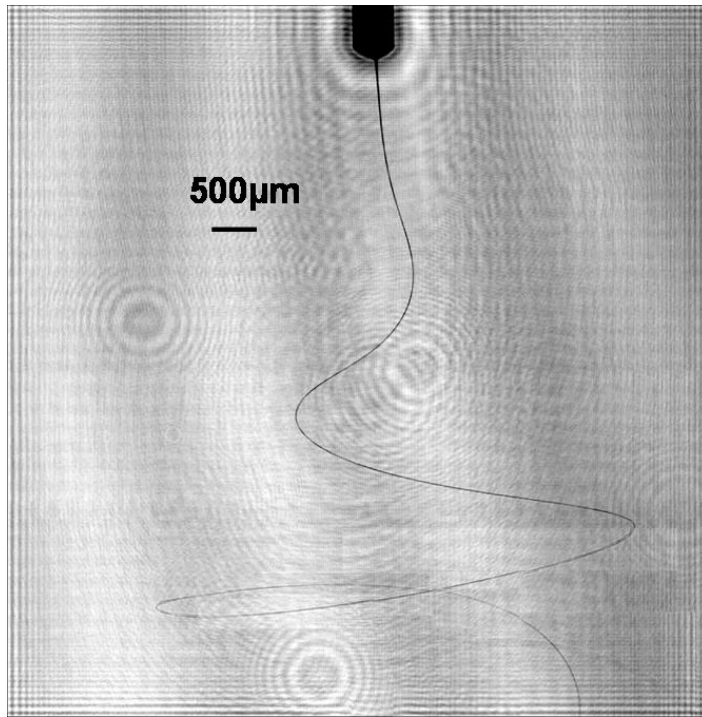
(a)
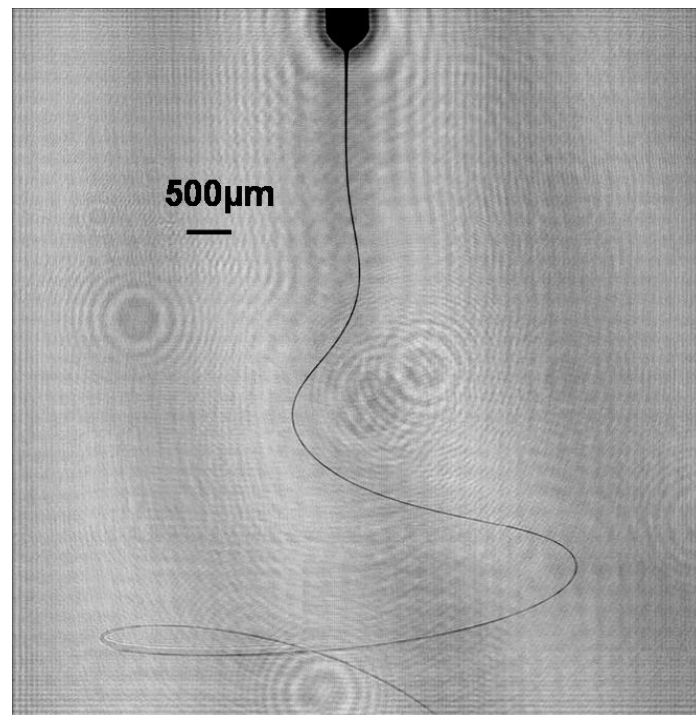
(b)

Figure 2-19. Reconstruction holograms of electrospun jet trajectories with the single front view for two different polymer concentrations, (a) 0.5% PEO solution and (b) 2.0% PEO solution. Test condition: 5 kV applied voltage and zero injection pressure
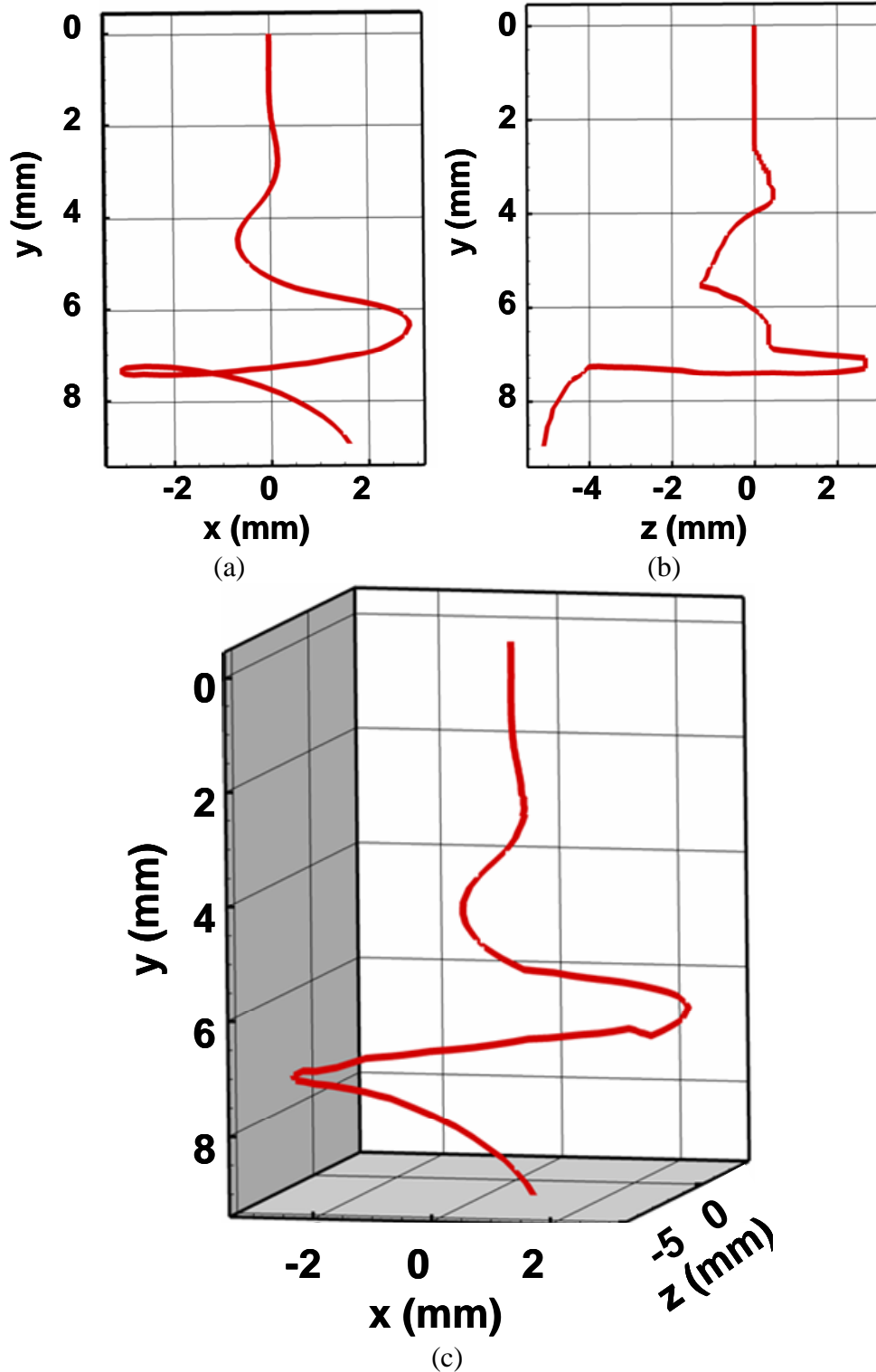
Figure 2-20 Three dimensional trajectory of the electrospun jet measured with the single front view hologram of Figure 19 (b). The results (a) and (b) show the front and span views of the three-dimensional jet trajectory, respectively. The result (c) shows the three-dimensional jet trajectory.
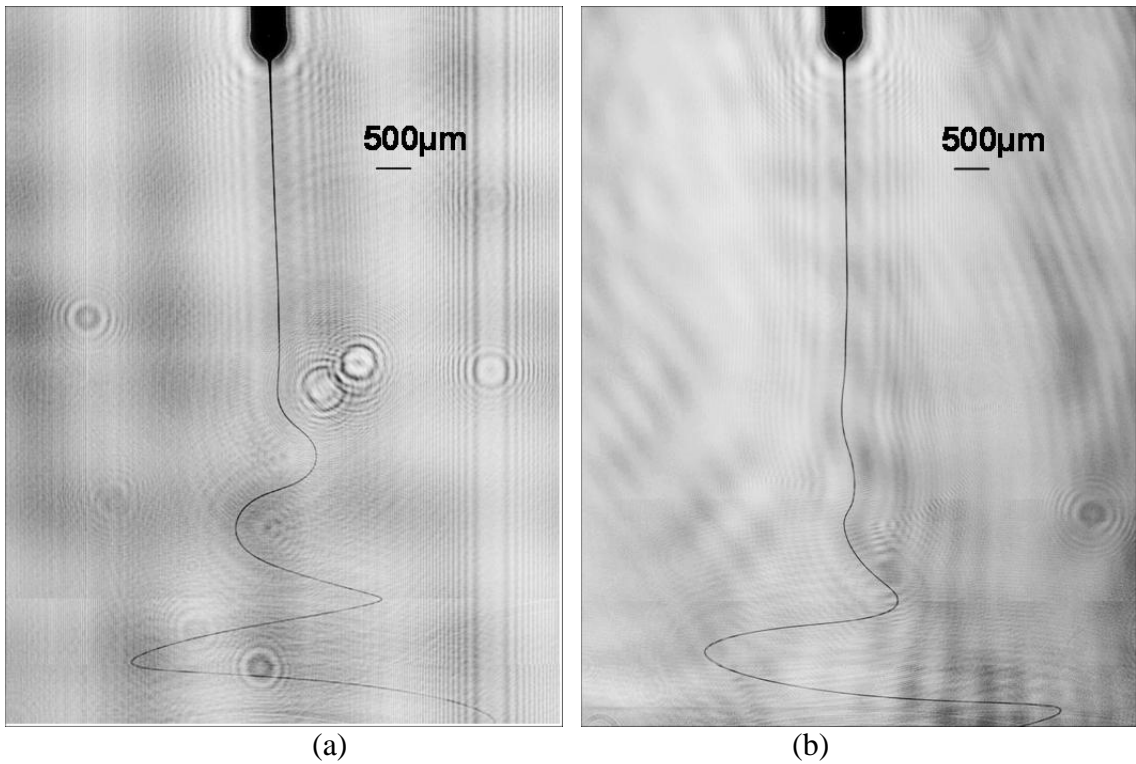
Figure 2-21 Reconstruction holograms of electrospun jet trajectories with double view, (a) front view (Nikon D-70) and (b) span view (Nikon D-80) for 0.5%PEO solution. Test conditions: 7 kV applied voltage and zero injection pressure
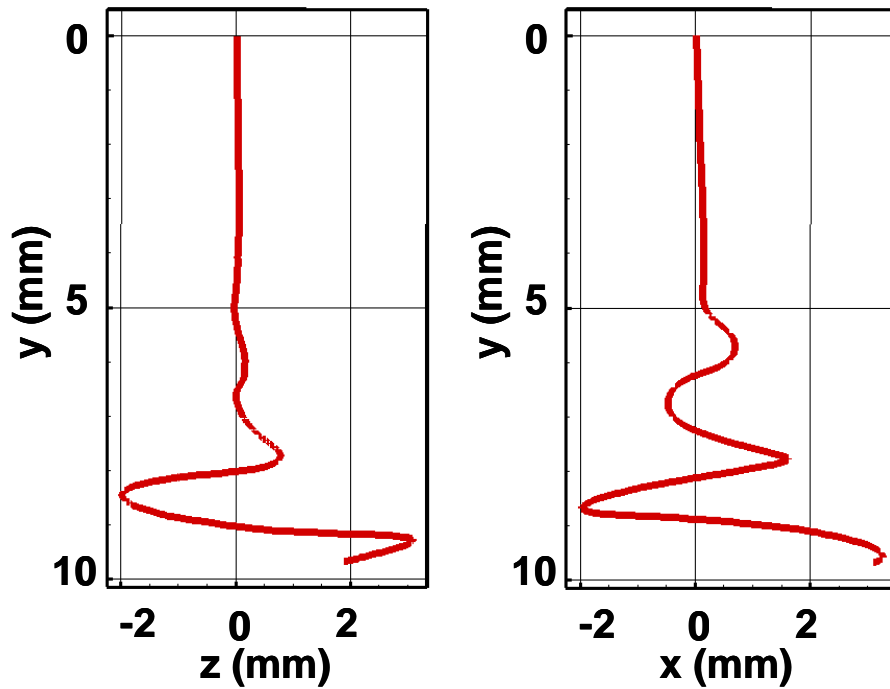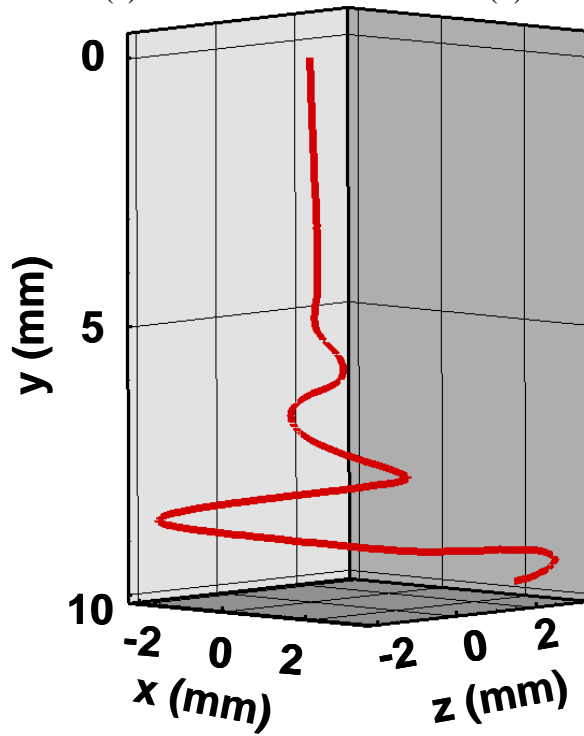
Figure 2-22 Three dimensional trajectory of the electrospun jet measured with the double view holograms of Figure 21 (a) & (b). The results (a) and (b) show the front and span views of the three-dimensional jet trajectory, respectively. The result (c) shows the three-dimensional jet trajectory.

CHAPTER III

RESULT AND DISCUSSION

3.1 Aerated Liquid Jets

Double-pulsed digital microscopic holography (DMH) was used for probing the dense-spray near-injector region of aerated liquid jet in crossflow. To overcome the limited field of view, the dense-spray region has been divided into nine investigation windows. Droplet diameters, locations, and three-dimensional velocities were measured in these nine investigation windows. For the flow visualization of the dense-spray region the spray structure map has been constructed by patching six high resolution holograms reconstructed at the same spanwise (distance from the camera) depth. Droplet sizes and three-dimensional velocities could be expressed together on the same plot. The majority of the droplets in the near-injector region were elliptical, and they were characterized using the equivalent diameter which is the diameter of a circle with the same area as an ellipsoidal drop. Mass averaged velocities were successful to describe the structure of aerated liquid jets.

3.1.1 Flow Visualization

A pulsed shadowgraph of aerated liquid jet in subsonic crossflow is shown in Figure 3-1.

76

This shadowgraph was obtained at the test conditions shown in Table. 2-1. Despite the high resolution achieved by using large format (127mm×127mm) film, this shadowgraph has limited depth of field, typical of large magnification shadowgraphy. The shadowgraph projects three-dimensional spray structure into two-dimensional spray with many drops out of focus due to the limited depth of field. To overcome the limited depth of field, digital microscopic holography (DMH) was used for the visualization. United States Air Force (USAF) resolution target was used to determine spatial resolution of the DMH. With the higher levels of magnification the three bar pattern could be seen as small as 5 μm. The dense spray region of the aerated liquid jet was divided into several investigation windows, and double-pulsed holograms were recorded for each window with the double exposure CCD sensor. Holograms digitally recorded on the CCD sensor have complete three-dimensional information. With the digital reconstruction process, three-dimensional information can be easily expressed with many two-dimensional slices. Thus, the entire flow field for any spanwise distance could be investigated by numerical reconstruction of original holograms. The original hologram and reconstruction hologram focused at the injector center plane are shown in Figure 3-2. The entire spray structure of the dense spray region of $x/d_o<13.5$ could be visualized with six high resolution holograms reconstructed at the same spanwise depth as shown in Figure 3-3. The aerated jet was injected into subsonic crossflow and bent in the crossflow direction. Most droplets detached from the liquid column of the aerated jet were non–spherical. Non-spherical droplet distribution near the injector is shown in Figure 3-2(b). The non-spherical droplet distribution explains why diagnostics like PDPA were not successful in

probing the dense spray region of the aerated liquid jets because the PDPA is usually based on the assumption of spherical droplets.

3.1.2 Jet Surface Velocity

Streamwise liquid surface velocities, v_s, were measured at the test conditions shown in Table 2-1. The liquid surface velocities were measured with several double-pulsed holograms. The liquid surface velocities of aerated liquid jets as the function of streamwise distance from the injector exit are shown in Figure 3-4. The first jet surface velocity measurement was conducted at a distance of $1.5d_o$ and was almost $0.6v_j$. This is plausible because the jet surface velocity immediately after the jet exit should be close to zero due to injector wall effects. The liquid velocity profile inside the injector would have a zero velocity near the wall due to the effect of no-slip condition between the liquid and the injector wall, and reaches maximum near the gas core. The surface velocities increase within the streamwise location of $y/d_o=1.5\sim5.5$ and then becomes nearly constant as the jet approaches the location of $y/d_o=5.5$. Liquid surface velocity obtained at $y/d_o=6$ was taken as the jet mean velocity (v_j).

3.1.3 Drop Sizes

The spatial resolution of the current setup was 5 µm which allowed the size measurement of most droplets in the dense spray region. Droplet sizes together with three-dimensional velocities were plotted as function of x-y-z location with different view angles. The expanding annular spray structure along the center plane ($z/d_o=0$) is illustrated in Figure 3-5. Many droplets are distributed at near-injector region and the rim region of the

annular spray structure. Few droplets are scattered near the gas core further away from the aerated injector. Non-spherical droplet diameter in the near-injector region was expressed by equivalent spherical diameter. The equivalent diameters were calculated as follows:

$$d_{eq} = (d_{max} \times d_{min})^{1/2} \hspace{2cm} (3\text{-}1)$$

where d_{max} and d_{min} are the major axis and the minor axis for an elliptical droplet, respectively. The sphericity for all droplets in the near-injector region could be expressed by dividing the major axis by the minor axis as shown in Figure 3-6. The droplets in the near-injector region were mainly non-spherical which makes them inaccessible for techniques like PDPA. The sphericity is large near the injector exit, but decreases in the downstream region due to the aerodynamic effects. Moreover, most droplets at the downstream region have relatively small diameter possibly due to the secondary breakup effect. The SMD reduced with the increase in downstream distance as shown in Figure 3-7. The reduction of the SMD in downstream region could have resulted from the secondary breakup. At each vertical plane, the SMD was observed to have smaller values near the gas core and higher values near the outer rim of the spray, following the annular spray structure typical of the aerated liquid jet with 8% GLR.

Droplet sizes normalized by their mass median diameter (MMD) satisfy Simmons' universal root normal distribution with MMD/SMD = 1.2 when plotted on a root-normal graph as shown in Figure 3-8. This means that a complete description of the

drop size distribution of aerated liquid jet in crossflow can be expressed by the SMD alone. The present study's data and previous data of Miller et al. (2008) are shown in Figure 3-8. The majority of these points fall on the line where the MMD/SMD = 1.2 (Simmons, 1977). This agreement helps to validate the present experimental method. Other drop size distributions including Rosin-Rammler & log-normal distributions were tested but did not produce satisfactory description of the spray. Those trials are shown in Appendix A.

3.1.4 Droplet velocities

The droplet velocities in the streamwise and the crossflow direction could be measured by observing the displacements of the center of each droplet between the double pulses. The spanwise velocity could be measured by observing the change of the planes of focus measured between the double pulses. The time interval between the two laser pulses was controlled by a delay generator. An oscilloscope and a photo detector were used to measure the time interval between the double pulses. Typical double-pulsed hologram used for three dimensional velocities measurement is shown in Figure 3-9. The time interval between these two laser pulses was 47 µs. The double-pulsed hologram was obtained at the following location: x/d_o=4.5~13.5 and y/d_o=18~27. Three individual droplets marked with three capital letters ("A," "B," and "C") on two holograms reconstructed at the different spanwise distances have different displacements in the streamwise and cross-stream directions. The droplets marked with the letter "C" and the letter "C'" were respectively focused at two different spanwise depths of z/d_o= -1 and z/d_o= -1.167. Droplet spanwise velocities were obtained by measuring the spanwise

distance between the two focused planes and the time interval between the double pulses. The droplet marked with "C" has negative spanwise velocity, because the droplet has receded from the injector center plane during the double pulses. It is plausible because the liquid sheet of the aerated jet with hollow-type structure spreads toward both positive and negative direction away from the injector center plane. This three-dimensional velocity measurement was performed for all individual droplets in nine investigation windows in the near-injector region.

The cross-stream droplet velocity distribution as function of droplet sizes is shown in Figure 3-10. The cross-stream droplet velocity, u, was normalized by the mass averaged cross-stream velocity, $\tilde{u}$, and droplet sizes are normalized by the SMD. The cross-stream velocities of smaller droplets are higher than the mass averaged cross-stream velocity, and the cross-stream velocities of bigger droplets are lower than the mass averaged velocity. This can be attributed to the effect of the mass of each droplet. The relationship between the cross-stream velocities normalized by the mass averaged cross-stream velocity and the droplet sizes normalized by the SMD is expressed as follows:

$$u/\tilde{u} > 1, \text{ for } d/SMD > 0.8 \qquad\qquad (3\text{-}2)$$

$$u/\tilde{u} = 1, \text{ for } 0.8 < d/SMD < 1.2 \qquad\qquad (3\text{-}3)$$

$$u/\tilde{u} < 1, \text{ for } d/SMD > 1.2 \qquad\qquad (3\text{-}4)$$

The streamwise droplet velocity distribution normalized by the mass averaged streamwise velocity, $\tilde{v}$, as the function of droplet sizes normalized by the SMD is shown

in Figure 3-11. The streamwise droplet velocities, $v/\tilde{v}$ is unity for droplet sizes normalized by the SMD greater than 0.4. Certainly one would expect the drop size effect to be the same as both the horizontal and vertical velocities. Any difference between Figure 3-10 and Figure 3-11 can be attributed probably due to the sample size limitation.

Mass averaged velocities in the streamwise and cross-stream directions, $\tilde{u}$ and $\tilde{v}$, have been measured within the spanwise distance of $z/d_o= -13\sim13$. The mass averaged cross-stream velocities normalized by the free crossflow velocity, $\tilde{u}/u_\infty$, are shown in Figure 3-12. The mass averaged streamwise velocities normalized by the mean aerated liquid jet velocity, $\tilde{v}/v_j$ are shown in Figure 3-13. The mass averaged streamwise velocities decrease further away from the injector exit due to drag force acting on the droplets causing them to lose their initial vertical momentum. The mass averaged cross-stream velocities increase with downstream distance due to the drag force of the crossflow on the droplets. Those drops should approach the crossflow velocity, u_∞, and lose completely the vertical momentum further away from the injector.

The spanwise droplet velocities normalized by the mass averaged spanwise velocity, $\tilde{w}$, as function of droplet sizes normalized by the SMD are shown in Figure 3-14. The large scattering of the data is probably due to the large uncertainty (33%) in the spanwise direction typical of single view DMH.
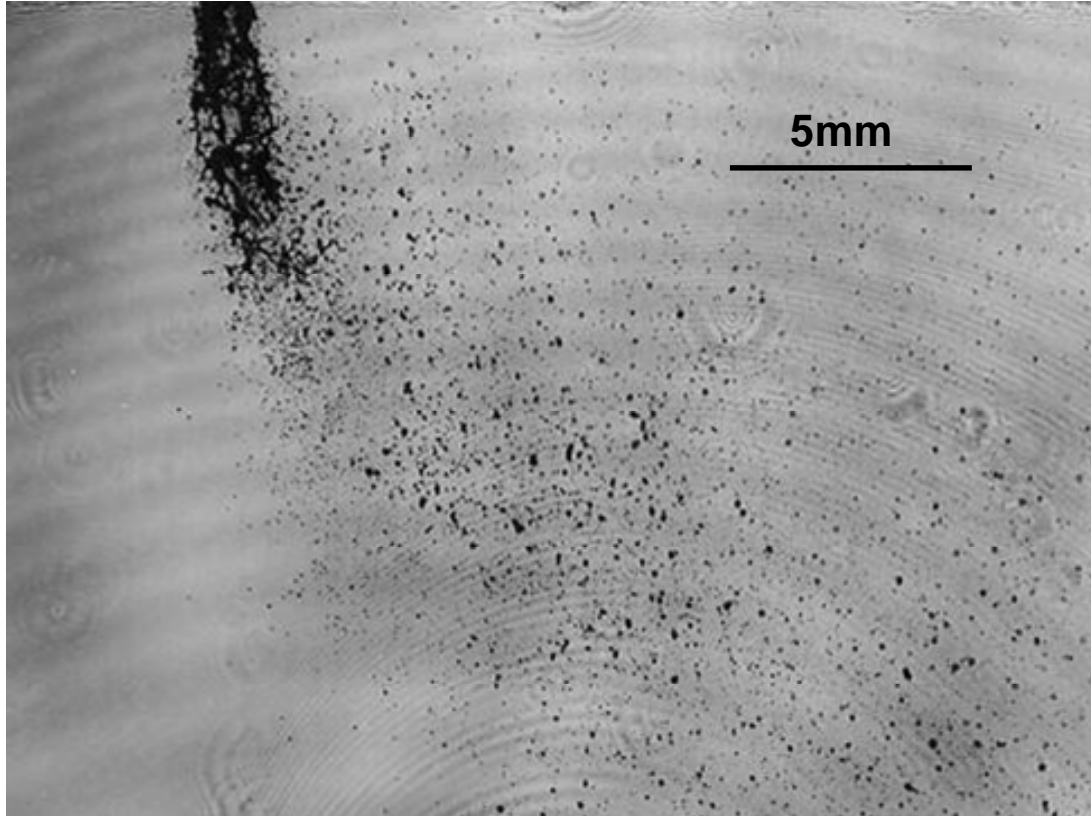
Figure 3-1 Pulsed shadowgraphy of aerated liquid jet in subsonic crossflow (Test condition: 1mm jet diameter, 8% GLR, and q_0=0.74).

(a)

1mm
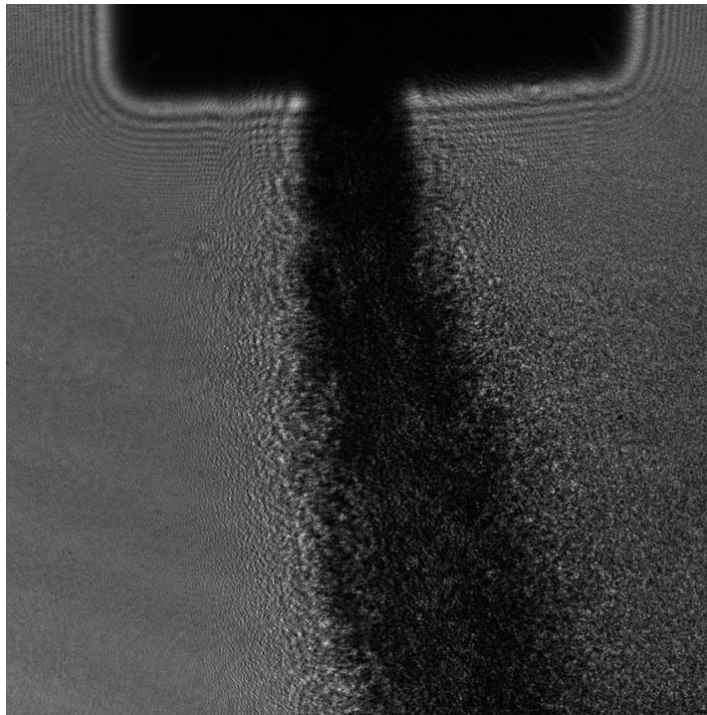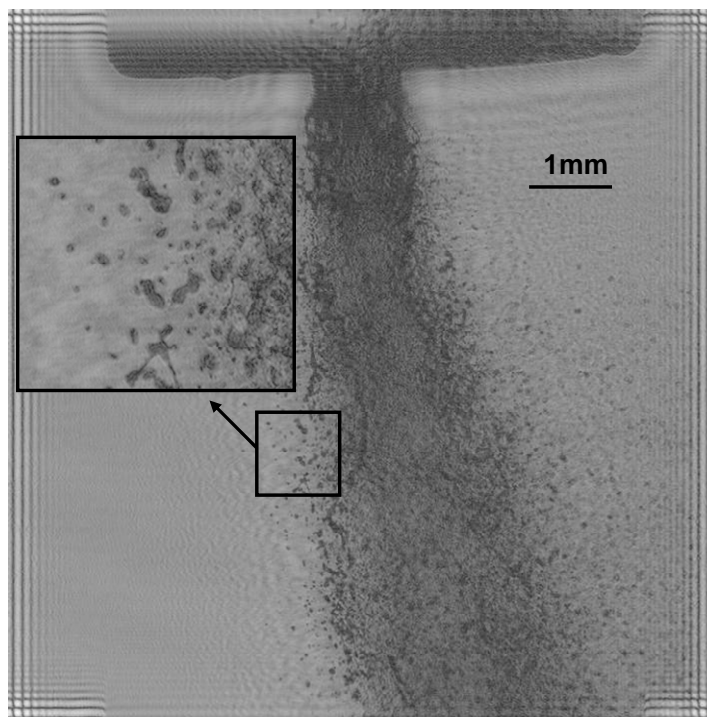
(b)

Figure 3-2 Hologram (a) recorded at the location of $x/d_0 = -4.5 \sim 4.5$ and $y/d_0 = 0 \sim 9$ (Test condition: 1mm jet diameter, 8% GLR, and $q_0=0.74$) and (b) reconstructed at the spanwise depth of 72 mm from CCD sensor: the inset shows an enlarged image of the small rectangular region.
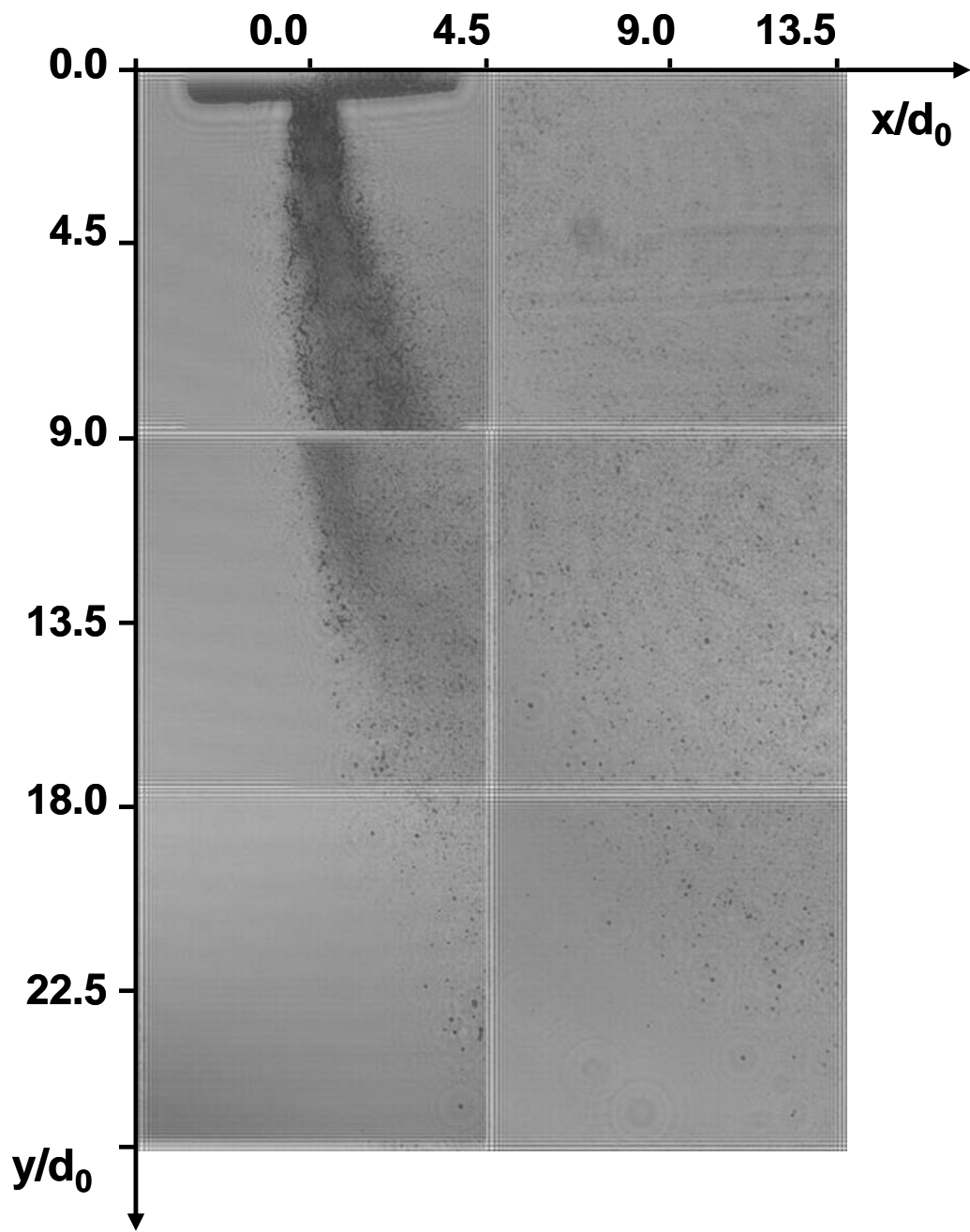
Figure 3-3 Aerated liquid jet spray structure near injector region.
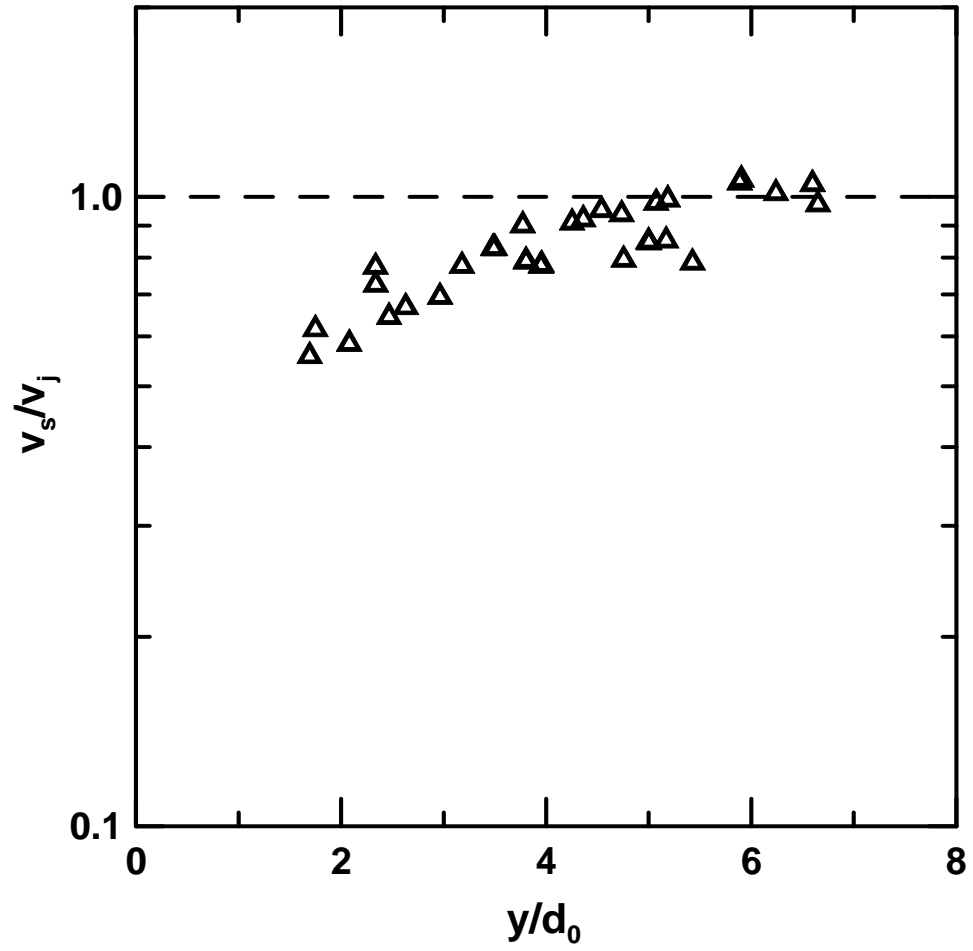
Figure 3-4 Variation of surface velocity of liquid sheet column ejected from the injector exit for streamwise distance.
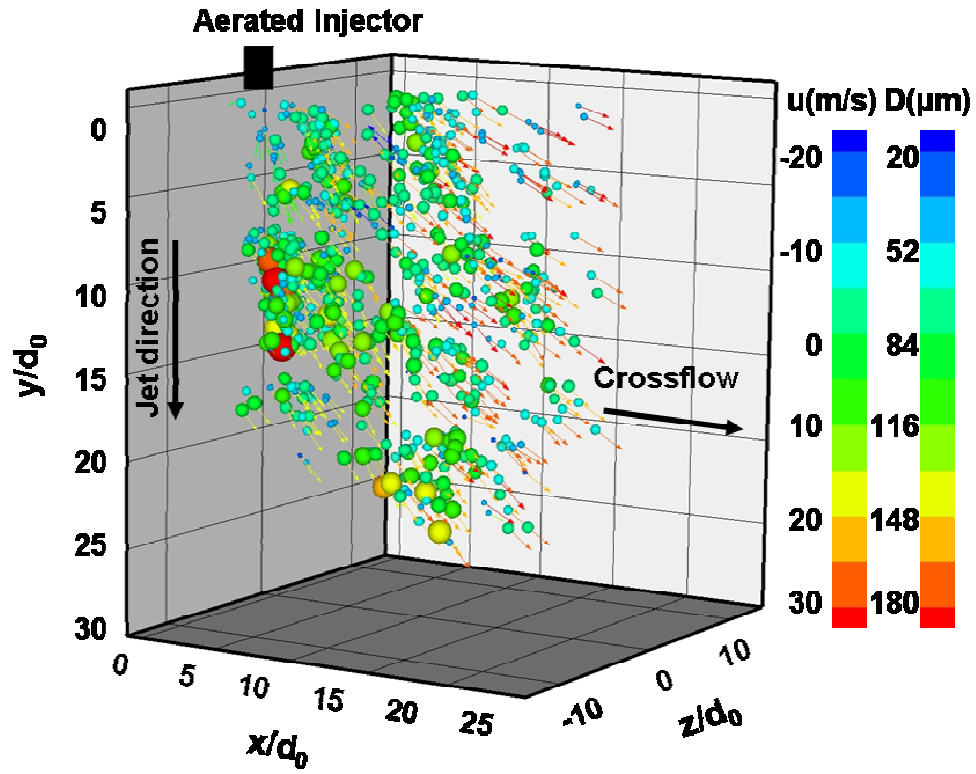
(a)
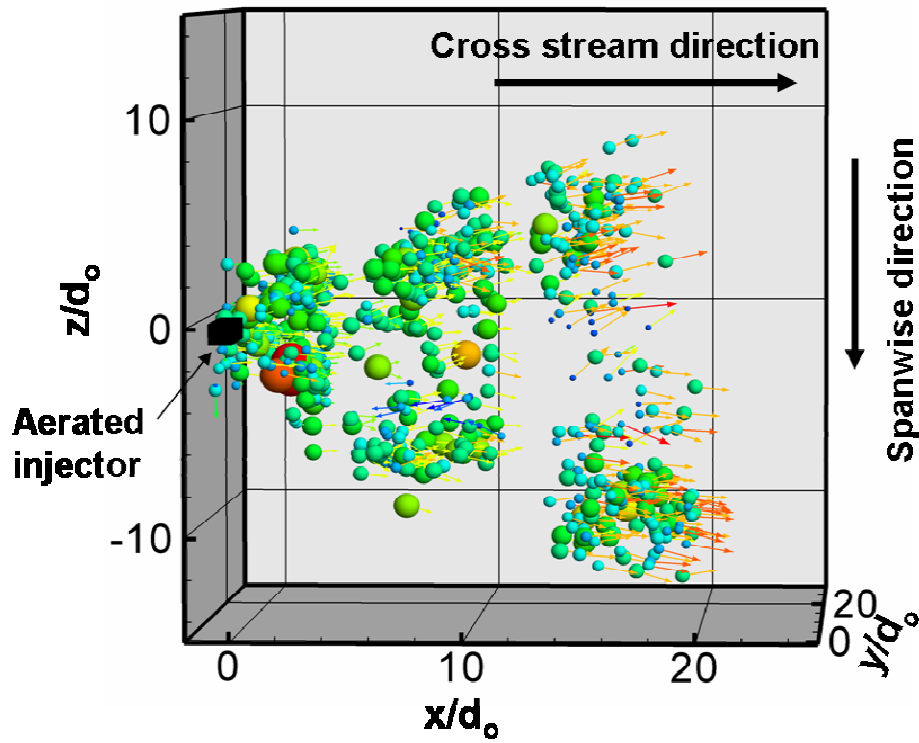
(b)

Figure 3-5 Drop size distribution and three-dimensional velocities near injector region for the different view angles (a) 3D view (b) top view.
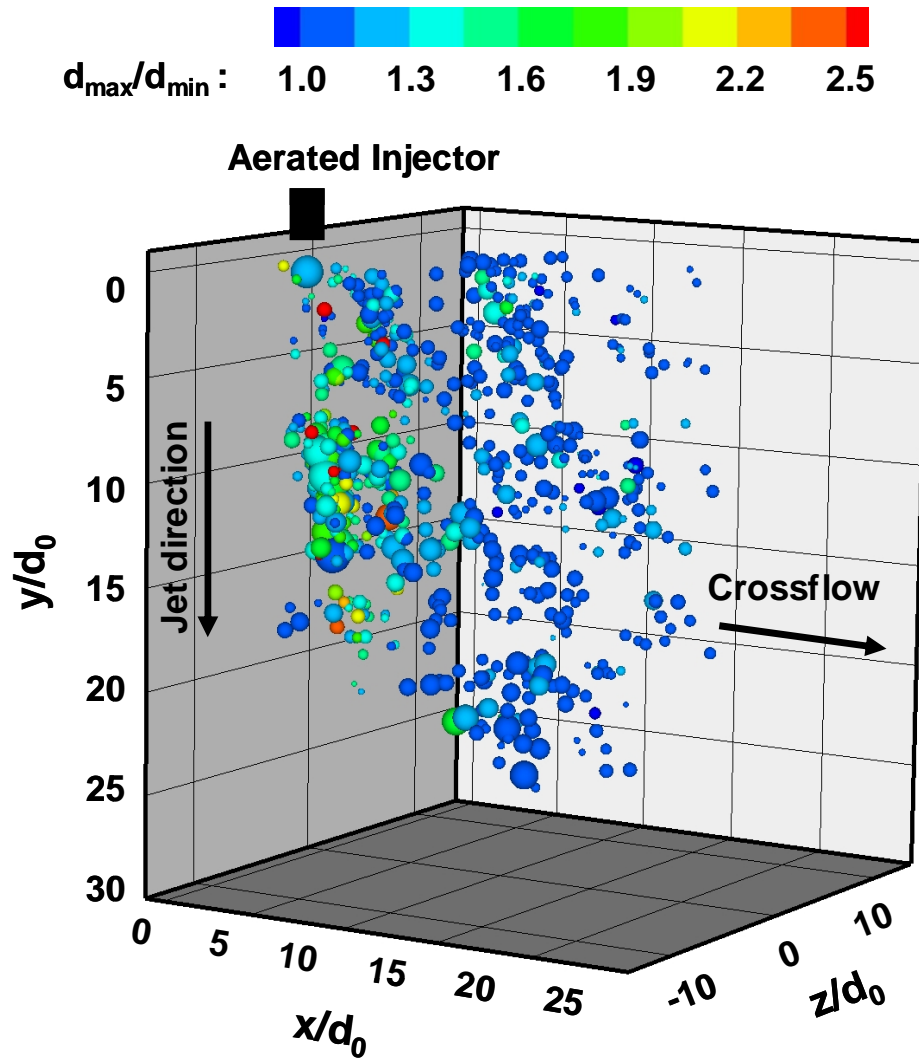
Figure 3-6 Sphericity of individual Droplets near very injector.
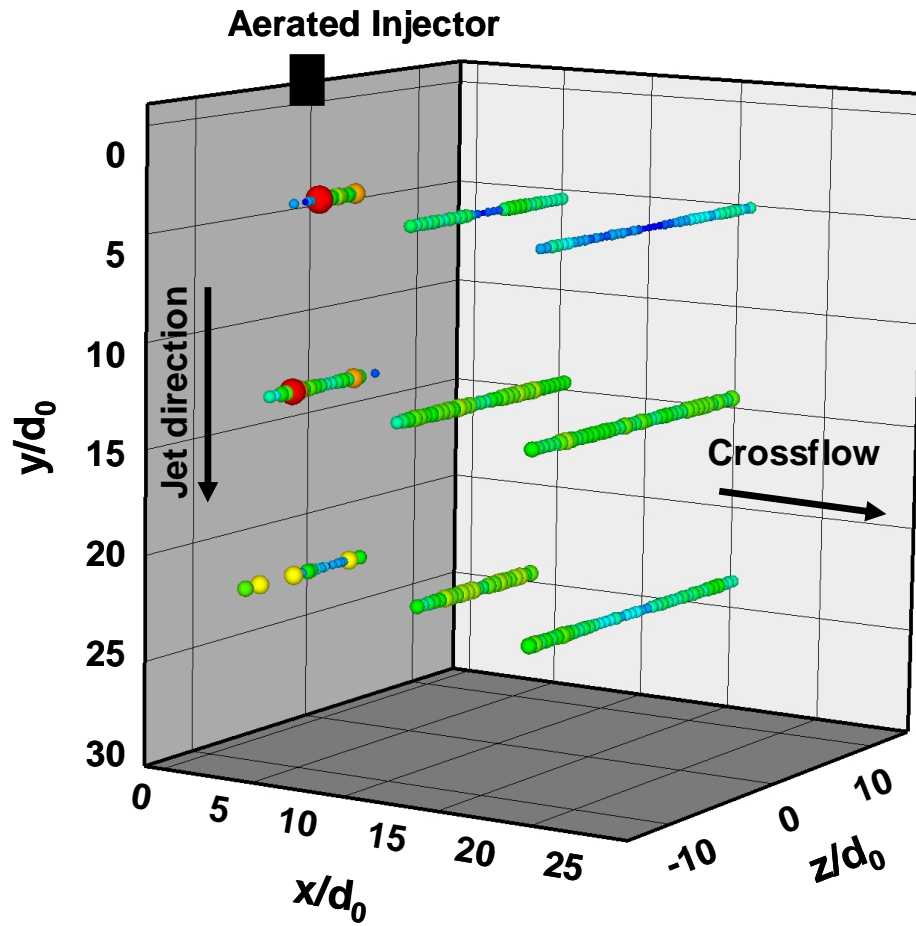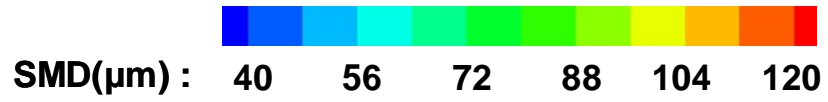
Figure 3-7 Sauter mean diameter (SMD) distribution near injector.
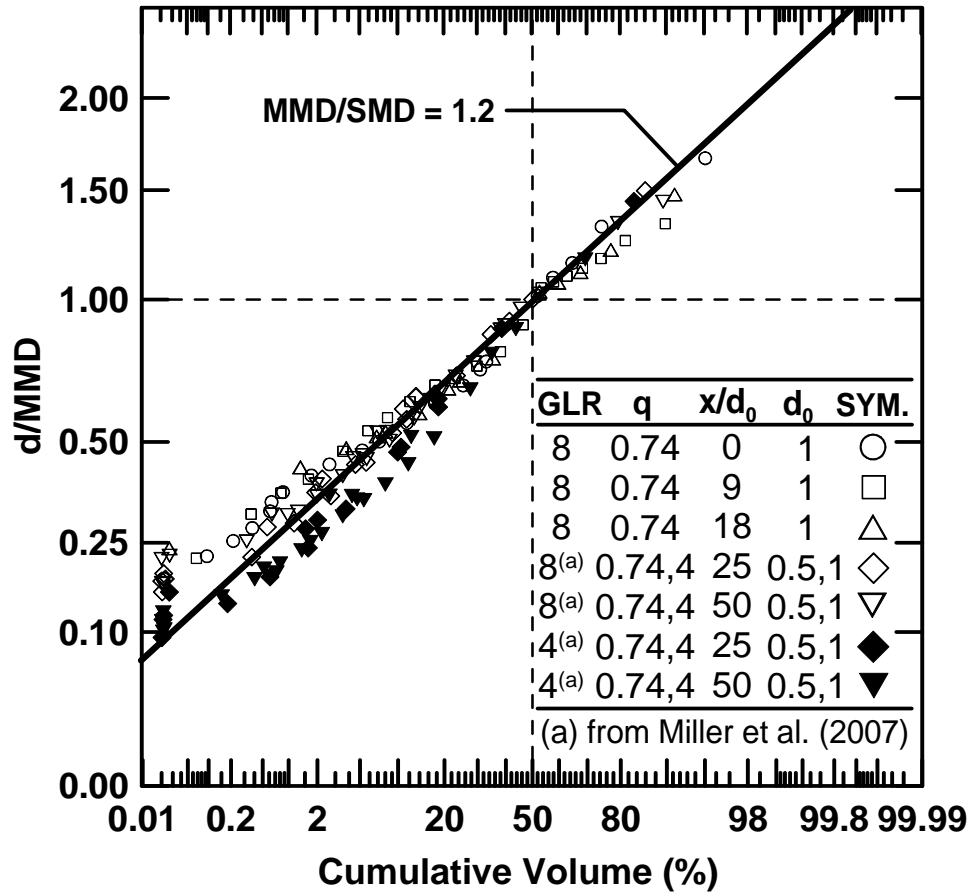
Figure 3-8 Droplet size distribution plotted on a root-normal scale.
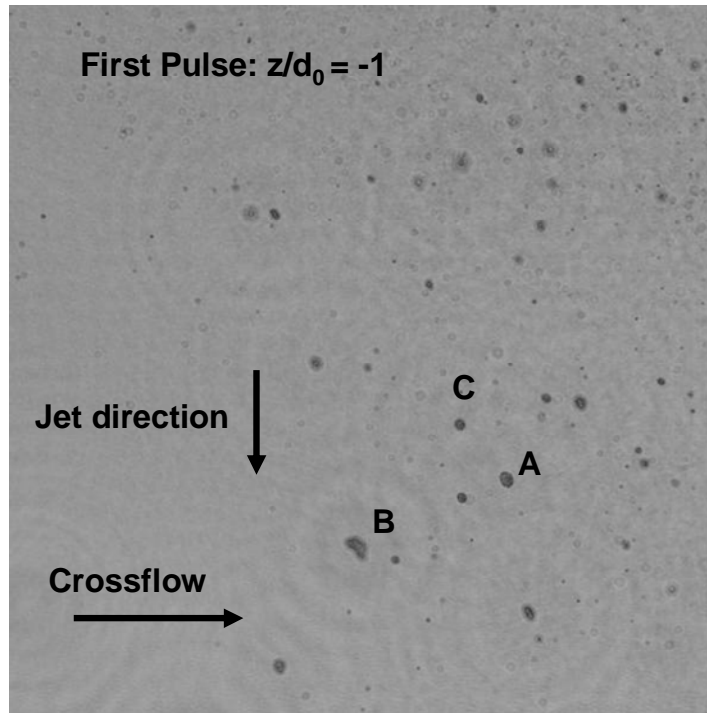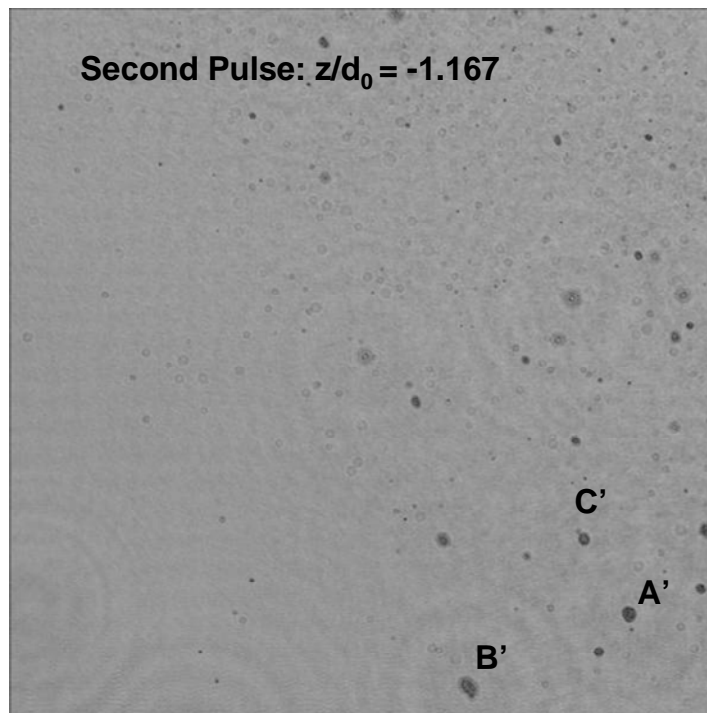
Figure 3-9 Double-pulsed reconstructed hologram at (a) t = 0 and (b) t = 47 µs. Test conditions are GLR = 8%, $q_0 = 0.74$ at $x/d_0 = 9$ and $y/d_0 = 22$. The letters "A," "B," and "C" refer to distinct droplets that are tracked between the two pulses to yield velocity information.
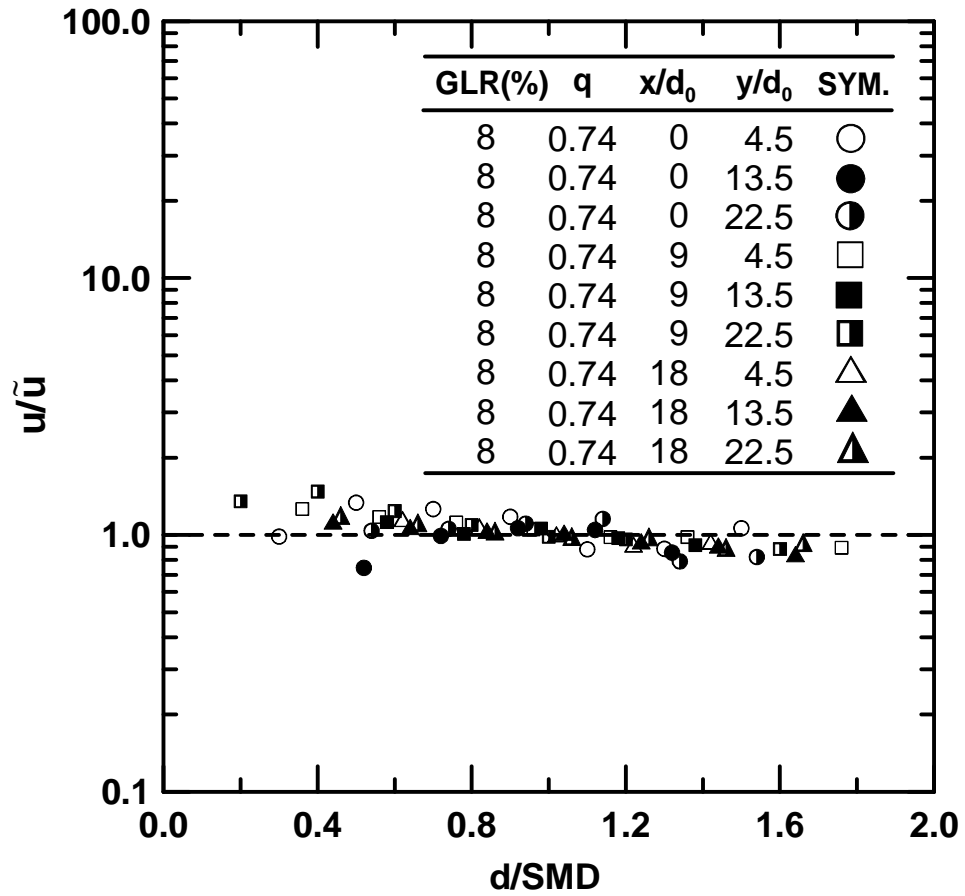
Figure 3-10 Cross-stream droplet velocities distribution normalized by mass averaged cross-stream velocity as function of droplet sizes.
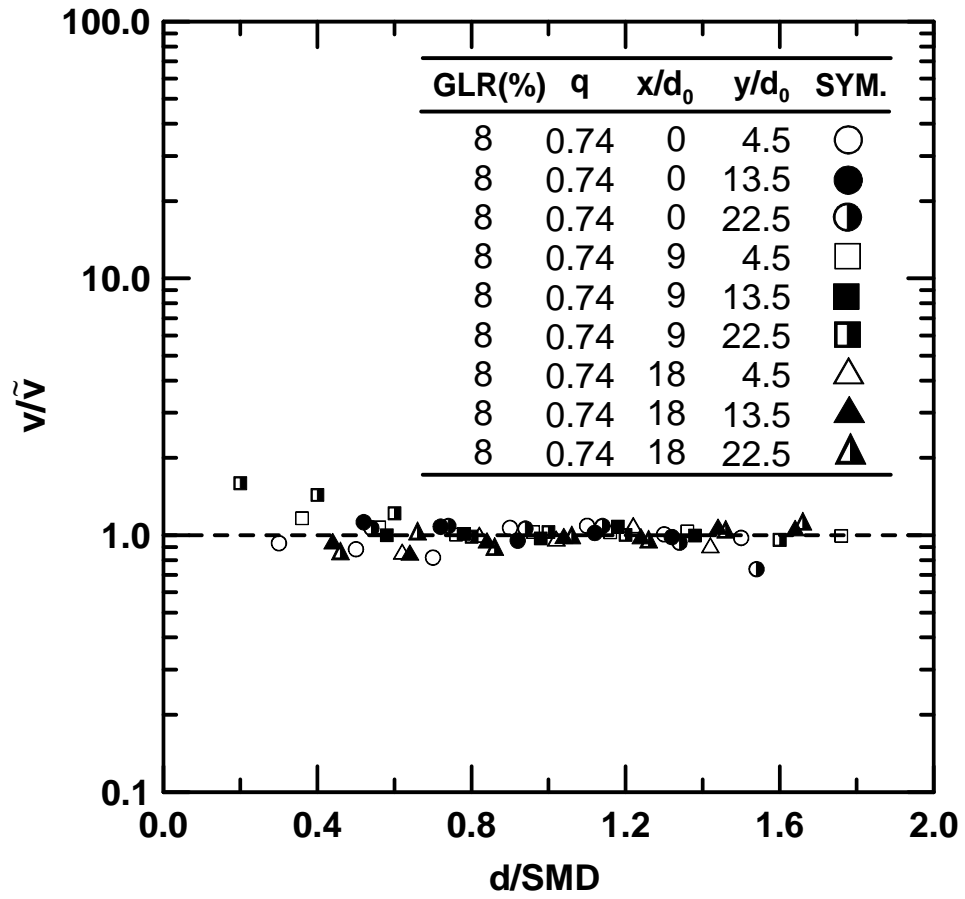
Figure 3-11 Streamwise droplet velocities distribution normalized by mass averaged streamwise velocity as function of droplet sizes.
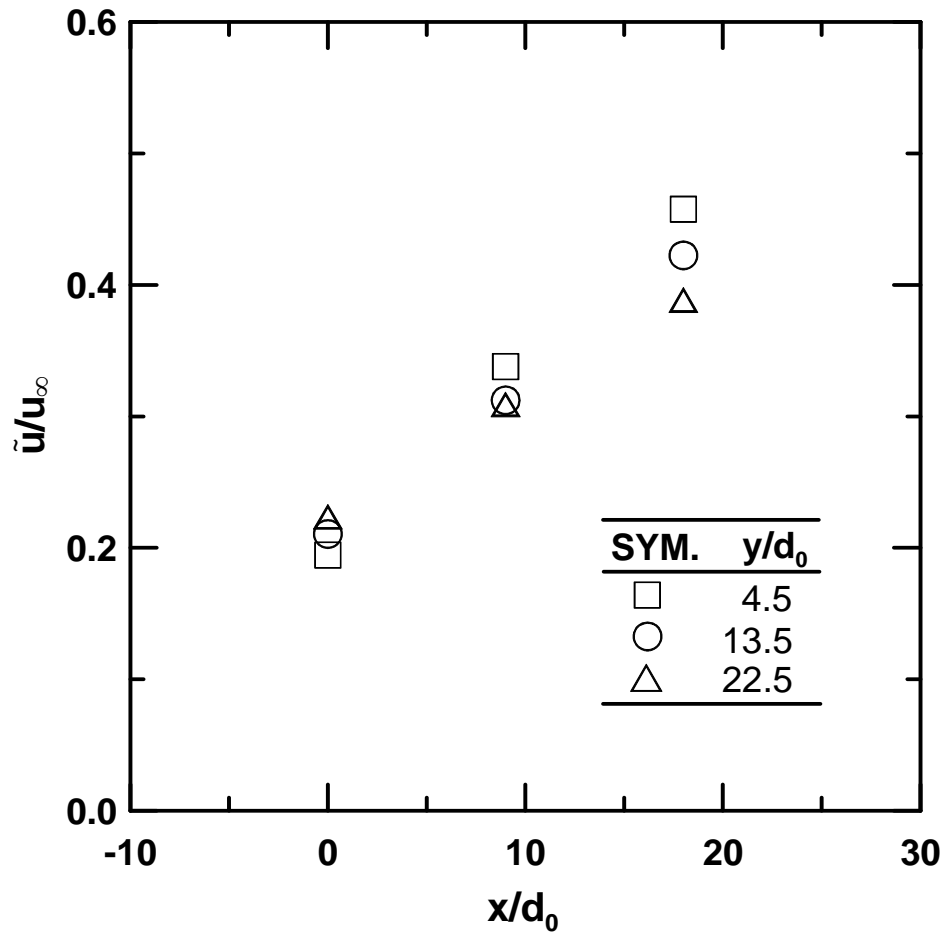
Figure 3-12 Mass averaged cross-stream droplet velocities for different x/d_0 locations.
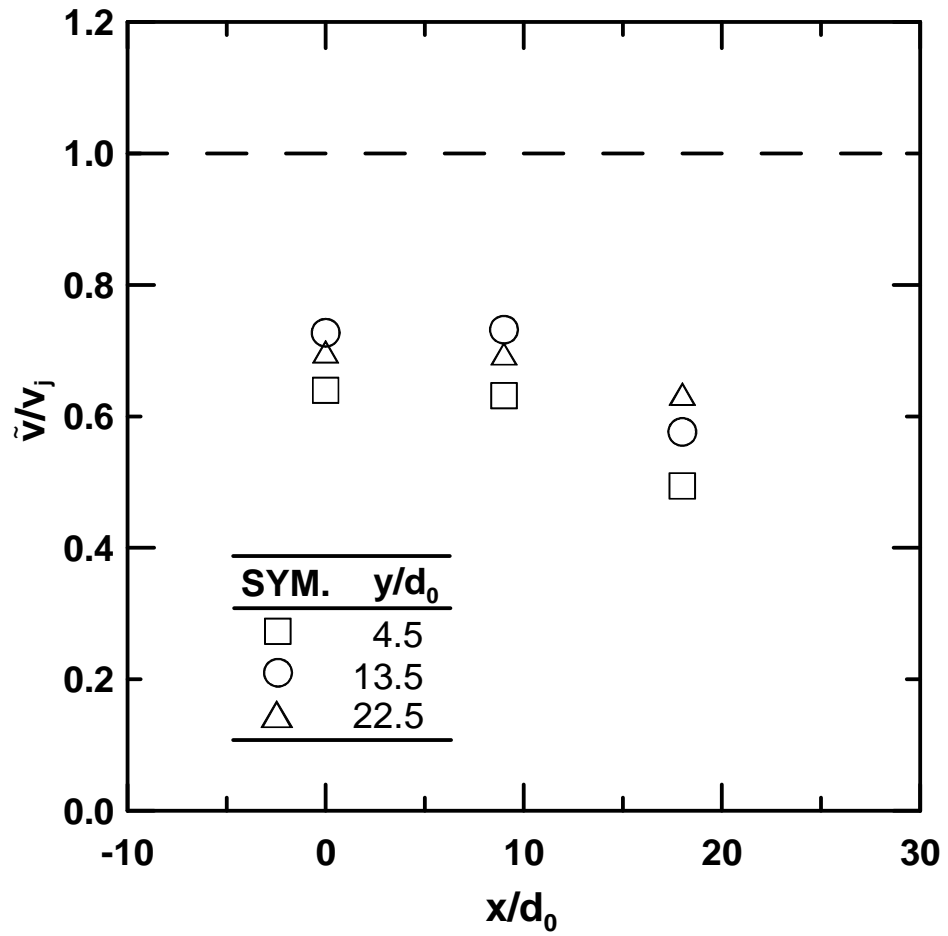
Figure 3-13 Mass averaged streamwise droplet velocities for different x/d_0 locations.

100.0

GLR(%)	q	x/d$_0$	y/d$_0$	SYM.
8	0.74	0	4.5	○
8	0.74	0	13.5	●
8	0.74	0	22.5	◐
8	0.74	9	4.5	□
8	0.74	9	13.5	■
8	0.74	9	22.5	◧
8	0.74	18	4.5	△
8	0.74	18	13.5	▲
8	0.74	18	22.5	◮

10.0

$|W|/\tilde{w}$

1.0

0.1

0.0   0.4   0.8   1.2   1.6   2.0

d/SMD
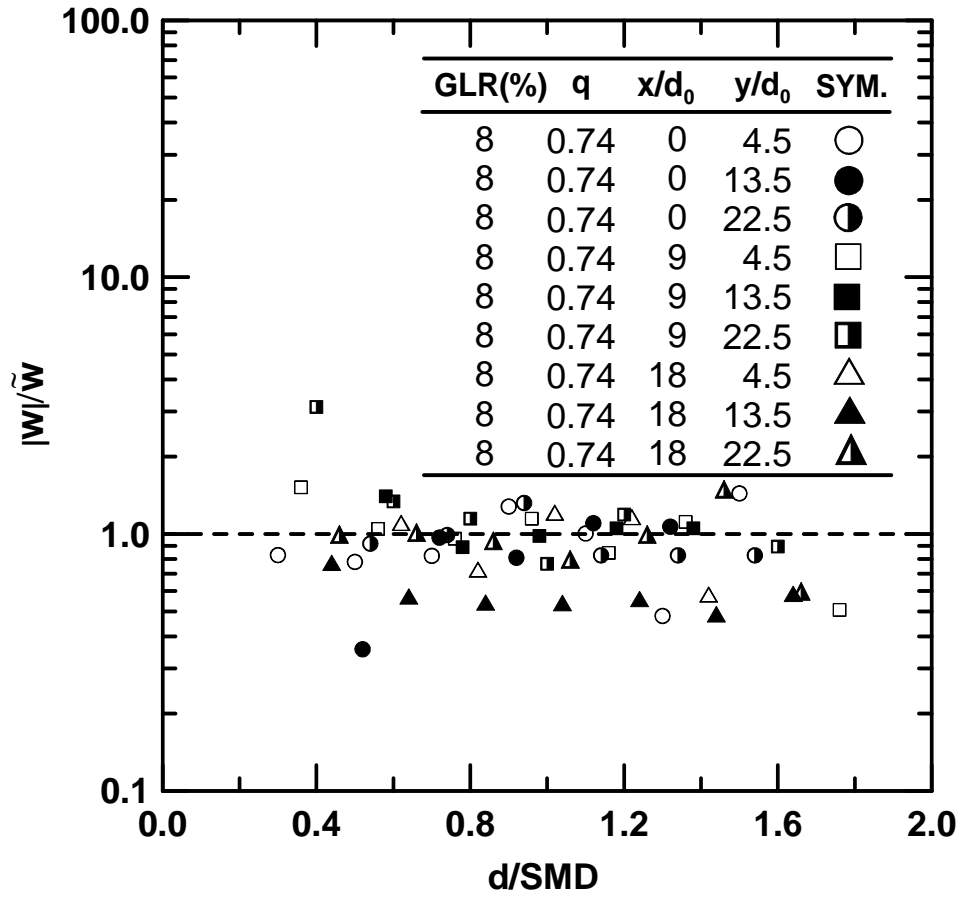
Figure 3-14 Spanwise droplet velocities distribution normalized by mass averaged spanwise velocity as function of droplet sizes.

CHAPTER IV

# SUMMARY, CONCLUSIONS AND FUTURE WORK

4.1 Summary

This study has managed to probe the spray generated by liquid jets using inexpensive color CCDs available in a consumer grade digital camera. The rapid progress in consumer grade digital cameras will allow larger holograms to be recorded which would possibly improve both the field of view and the resolution of the reconstructed hologram. The near-injector regions of micro liquid jets and aerated liquid jets in subsonic crossflow were investigated by double-pulsed digital microscopic holography (DMH). The holograms were recorded with a spatial resolution of 5 µm, and were numerically reconstructed at different spanwise distances. To overcome the limited field of view of DMH, the near-injector region has been divided into several investigation windows. To visualize the entire structure of the aerated liquid jet, a spray map was constructed by patching several reconstruction holograms with high resolution. Individual droplet sizes, locations, and three-dimensional velocities were measured. Mass averaged velocities distributions were obtained as function of droplet sizes normalized by the Sauter mean diameter (SMD). Three dimensional trajectories of bending instability of electrospinning polymer jets were tracked using orthogonal double view DMH. The uncertainty in spanwise jet trajectory measurements was reduced using double view DMH.

4.2 Conclusions

The conclusions of the use of DMH in the present study were as follows:

1. Digital microscopic holography (DMH) is a useful tool for examining the spray in the near injector region and can provide information other non-imaging methods can not. This is due to the fact that it is insensitive to non-spherical droplets and its inherent three-dimensional nature. This is particularly useful for sparse but spatially distributed sprays.

2. The cost of the DMH for liquid jets breakup can be reduced using commercial grade CCD. For the velocity measurement, double pulsed holograms were recorded on the same camera frame. To overcome the small field of view of the DMH, spray maps with the large field of view were obtained by simply patching several high resolution holograms.

3. Droplet velocities in three-dimensions were measured by tracking their displacements during the time interval between the double-pulses in the streamwise and cross-stream direction and by tracking the change in the plane of focus in the spanwise direction using single view DMH.

4. Single view DMH worked well for drop size, location, and velocity measurements in cross-stream and jet streamwise directions. The large uncertainty in spanwise drop location measurement of single view DMH can be reduced by employing

double view DMH. Using two orthogonal CCD sensors quantitatively reduced the uncertainty and qualitatively increased the spatial resolution in spanwise direction.

The conclusions of the spray structure study were as follows:

1. Most droplets in the probed region are non-spherical. The droplets were considered elliptical in shape and were characterized by their equivalent spherical diameter.

2. The distributions of the streamwise and cross-stream velocities were uniform in the near-injector region and could be characterized by the mass-average velocity except for very small and very large droplets.

3. The drop size distributions of aerated liquid jet in crossflow for the present test conditions (i.e., GLR 8%) followed Simmons' universal root normal distribution (Simmons13) and thus could be fully described by the SMD alone.

4.3 Recommendation for Future Work

1. In spite of the reduced cost of hologram recording by using an inexpensive CCD sensor, DMH is still expensive due to the cost of double-pulse Nd:YAG lasers typically used in the setup. A new DMH method using a commercial CCD and DPSS lasers has to be developed to reduce the cost of the system.

2. The image analysis process of measuring the droplet locations and sizes from many reconstruction holograms needs to be automated. Image processing techniques finding the focused plane of drops and tracking droplet sharp edges should be developed for the accurate measurement. The automated DMH would have a wide range of application to many sprays and particle measurements.

REFERENCES

Andrady, A. L., *Science and Technology of Polymer Nanofibers*, Wiley, New Jersey, 2008.

Buckner, H. N., and Sojka, P.E., "Effervescent Atomization of High-Viscosity Fluids: Part I. Newtonian Liquids," *Atomization and Sprays*, Vol. 1, 1991, pp. 239-252.

Burke, J., Hess, C. F., and Kebbel V., "Digital Holography for Instantaneous Spray Diagnostics on a Plane," *Particle & Particle Systems Characterization*, Vol. 20, 2003, pp. 183-192.

Deitzel, J. M., Kleinmeyer, J. D., Hirvonen, J. K., and Beck Tan, N. C., "Controlled Deposition of Electrospun Poly(ethylene oxide) Fibers," *Polymer*, Vol. 42, 2001, pp. 8163-8170.

Deitzel, J. M., Kleinmeyer, J. D., Harris, N. C., and Beck Tan, N. C., "The Effect of Processing Variables on the Morphology of Electrospun Nanofibers and Textiles," *Polymer*, Vol. 42, 2001, pp. 261-272.

Doshi, J. and Reneker, D., "Electrospinning Process and Applications of Electrospun Fibers," *Journal of Electrostatics*, Vol. 35, 1995, pp. 151-160.

Dzenis, Y., "Spinning Continuous Fibers for Nanotechnology," *Science*, Vol. 304, 2004, pp. 1917-1919.

Dunn, P. F., *Measurement and Data Analysis for Engineering and Science*, McGraw Hill, New York, 2005.

Fong, H., Chun, I., and Reneker, D. H., "Beadaed nanofibers formed during electrospinning," *Polymer*, Vol. 40, 1999, pp. 4585-4592.

Gabor, D. A., New Microscopic Principle, *Nature*, Vol. 161(4098), 1948, pp. 777-778.

Garcia-Sucerquia, J., "Immersion Digital In-line Holographic Microscopy," *Optics Letters*, Vol. 31, 2006, pp. 1211-1213.

Garcia-Sucerquia J., Xu, W., Jericho, S. K., Klages, P., Jericho, M. H, and Kreuzer, J, "Digital In-line Holographic Microscopy", *Applied Optics*, Vol. 45, 2006, pp. 836-850.

Goodman, J. W., and Lawrence, R. W., "Digital Image Formation from Electronically Detected Holograms", *Applied Physics Letters*, Vol. 11(3), 1967, pp. 77-79.

Hariharan, P., *Basics of Holography*, Cambridge U. Press, Cambridge, 2002.

Hohman, M. M., Shin, M., Rutledge, G., and Brenner M. P., "Electrospinning and electrically forced jets: II. Applications," *Physics of Fluids*, Vol. 13, 2001, pp. 2221-2236.

Hohman, M. M., Shin, M., Rutledge, G., and Brenner, M. P., "Electrospinning and Electrically Forced Jets. I. Stability theory," *Physics of Fluid*, Vol. 13, 2001, pp. 2201-2220.

Jaworek, A., and Krupa, A., "Classification of the Modes of EHD Spraying," *J. Aerosol Sci*, Vol. 30, 1999, pp. 873-893.

Jones, A. R., Sarjeant, M., Davis, C. R., and Denham, R., "Application of In-line Holography to Drop Size Measurement in Dense Fuel Sprays," *Applied Optics*, Vol. 17(3), 1977, pp. 328-333.

Koombhongse, S., Liu, W., and Reneker, D. H., "Flat Polymer Ribbons and Other shapes by Electrospinning," *Journal of Polymer Science Part B: Polymer Physics*, Vol. 39, 2001, pp. 2598-2606.

Kreis, T. M., Adams, M., and Jüptner, W. P., "Methods of Digital Holography: A Comparison," *SPIE*, Vol. 3098, 1997, pp. 224-233.

Kim, J. Y., and Lee, S. Y., "Dependence of Spraying Performance on the Internal Flow Pattern in Effervescent Atomizers," *Atomization and Sprays*, Vol. 11, 2001, pp. 735–756.

Lee, J., Sallam, K. A., Lin, K.-C., and Carter, C.D., "Spray Structure in Near-Injector Region of Aerated Jet in Subsonic Crossflow," *Journal of Propulsion and Power*, Vol. 25, 2009, pp. 258-266.

Lee, J., Miller, B., and Sallam, K.A., "Demonstration of Digital Holographic Diagnostics for the Breakup of Liquid Jets Using a Commercial-Grade CCD Sensor," *Atomizatoin Sprays*, Vol. 19, 2009, pp. 445-456.

Lefebvre, A. H., Wang, X.F., and Martin, C. A., "Spray Characteristics of Aerated-Liquid Pressure Atomizers," *Journal of Propulsion*, Vol. 4, 1988, pp. 293-298.

Leith, E. N., and Upatniek, J., "Holograms: Their Properties and Uses," *Society of Photo-Optical Instrumentation Engineers Journal*, Vol. 4(1), 1965.

Lin, K.-C., Kennedy, P. J., and Jackson, T. A., "Spray Structures of Aerated-Liquid Jets in Subsonic Crossflows," *32nd AIAA Aerospace Sciences Meeting*, AIAA Paper 2001-0330, 2001.

Lin, K.-C., Kennedy, P. J., and Jackson, T. A., "Structures of Aerated Liquid Jets in High Speed Crossflows," *32nd AIAA Fluid Dynamics Conference*, AIAA Paper 2002-3178, 2002.

Lund, M. T., Sojka, P. E., Lefebvre, A. H., and Gosselin, P.G., "Effervescent Atomization at Low Mass Flow Rates Part 1: The Influence of Surface Tension," *Atomization and Sprays*, Vol. 3, 1993, pp. 77-89.

Mazallon, J., Dai, Z., and Faeth, G. M., "Primary Breakup of Nonturbulent Round Liquid Jets in Gas Crossflows," *Atomization and Sprays*, Vol. 9, 1999, pp. 291-311.

Meng, H., and Hussain, F., "In-line Recording and Off-axis Viewing Technique for Holographic Particle Velocimetry," *Applied Optics*, Vol. 34(11), 1995, pp. 1827-1840.

Meng, H., Anderson, W. L., Hussain, F., and Liu, D. D., "Intrinsic Speckle Noise in In-line Particle Holography," *Journal of the Optical Society of America*, Vol. 10(9), 1993, pp. 2046-2058.

Meng, H., Pan, G., Pu, Y., and Woodward, S. H., "Holographic particle image velcimetry: from film to digital recording," *Meas. Sci. Technol*, Vol. 15, 2004, pp. 673-685.

Munson, B. R., Young, D. F., and Okiishi, T. H., *Fundamentals of Fluid Mechanics*, John Wiley & Sons, 2006.

Miller, B., Sallam, K. A., Bingabr, M., Lin, K.-C., and Carter, C. D., "Breakup of Aerated Liquid Jets in Subsonic Crossflow," *Journal of Propulsion and Power*, Vol. 24, No. 2, 2008, pp. 253–258.

Miller, B., "Digital Holographic Diagnostics of Aerated-Liquid Jets in a Subsonic Crossflow," M.S. Thesis, Oklahoma State University, Fall 2006

Palero, V., Arroyo, M. P., and Sorica, J., "Digtial Holography for Micro-droplet Diagnostics," *Experiments in Fluids*, Vol. 43, 2007, pp. 185-195.

Reneker, D. H., Yarin, A. L., Fong, H., and Koombhongse, S., "Bending Instability of Electrically Charged Liquid Jets of Polymer Solutions in Electrospinning," *Journal of Applied Physics*, Vol. 87, 2000, pp. 4531-4547.

Reneker, D. H., and Chun, I., "Nanometre Diameter Fibres of Polymer, Produced by Electrospinning," *Nanotechnology*, Vol. 7, 1996, pp. 216-223.

Rutledge, G. C., and Fridrikh, S. V., "Formation of Fibers by Electrospinning," *Advanced Drug Delivery Reviews*, Vol. 59, 2007, pp. 1384-1391.

Santangelo, P. J., and Sojka, P. E., "A Holographic Investigation of an Effervescent Atomizer-Produced Spray," *Atomization and Sprays*, Vol. 5, 1995, pp. 137-155.

Sallam, K. A., Aalburg, C., Faeth, G. M., Lin, K.-C., Carter, C. D., and Jackson, T. A., "Primary Breakup of Round Aerated-Liquid Jets in Supersonic Crossflows," *Atomization and Sprays*, Vol. 16, No. 6, 2006, pp. 657–672.

Sallam, K. A., Aalburg, C., and Faeth, G. M., "Breakup of Round Nonturbulent Liquid Jets in Gaseous Crossflow," *AIAA Journal*, Vol. 42, 2004, pp. 2529-2540.

Sallam, K. A., Dai, Z., and Faeth, G. M., "Liquid Breakup at the Surface of Turbulent Round Liquid Jets in Still Gases," *International Journal of Multiphase Flow*, Vol. 28, 2002, pp. 427-449.

Sallam, K. A., Dai, Z., and Faeth, G. M., "Drop Formation at the Surface of Plane Turbulent Liquid Jets in Still Gases," *International Journal of Multiphase Flow*, Vol. 25, 1999, pp. 1161-1180.

Schnars, U., and Jueptner, W., *Digital Holography: Digital Hologram Recording, Numerical Reconstruction, and Related Techniques*, Springer, Berlin, 2005.

Schnars, U. and Jueptner, W., "Direct Recording of Holograms by a CCD Target and Numerical Reconstruction," *Applied Optics*, Vol. 33(2), 1994, pp. 179-181.

Simmons, H. C., "The Correlation of Drop-Size Distributions in Fuel Nozzle Sprays," *Journal of Engineering for Power*, Vol. 99, No. 3, 1977, pp. 309–319.

Sheng, J., Malkiel, E., and Katz, J., "Digital Holographic Microscope for Measuring Three-dimensional Particle Distributions and Motions," *Applied Optics*, Vol. 45(16), 2006, pp. 3893-3901.

Shin, Y. M., Hohman, M. M., Brenner, M. P., and Rutledge, G. C., "Experimental Characterization of Electrospinning; The Electrically Forced Jet and Instabilities," *Polymer*, Vol. 42, 2001, pp. 9955-9967.

Shin, Y. M., Hohman, M. M., Brenner, M. P., and Rutledge, G. C., "Electrospinning: A Whipping Fluid Jet Generates Submicron Polymer Fibers," *Applied Physics Letters*, Vol. 78, 2001, pp. 1149-1151.

Sutherland, J. J., Sojka, P. E., and Plesniak, M. W., "Entrainment by Ligament Controlled Effervescent Atomizer Produced Sprays," *Int. J. Multiphase Flow*, Vol. 23, 1996, pp. 865-884.

Vikram, C. S., *Particle Field Holography*, Cambridge U. Press, Cambridge, 1992.

Wade, R. A., Weerts, J. M., Sojka, P. E., Gore, J. P., and Eckerle, W. A., "Effervescent Atomization at Injection Pressures in the MPa Range," *Atomization and Sprays*, Vol. 9, No. 6, 1999, pp. 651-657.

Wannatong, L., Sirivat, A., and Supaphol, P., "Effects of Solvents on Electrospun Polymeric Fibers; Preliminary Study on Polystyrene," *Polymer International*, Vol. 53, 2004, pp. 1851-1859.

Wu, P. K., Kirkendall, K. A., Fuler, R. F., and Nejad, A. S., "Breakup Processes of Liquid Jets in Subsonic Crossflows," *Journal of Propulsion and Power*, Vol. 13, 1997, pp. 64-73.

Xu, W., Jericho, M. H., Meinertzhagen, I. A., and Kreuzer, H. J., "Digital Inline Holography for Biological Applications," *Proceedings of the National Academy of Sciences of the United States of America*, Vol. 98, 2001, pp. 11301-11305.

Xu, W., Jericho, M. H., Meinertzhagen, I. A., and Kreuzer, H. J., "Digital Inline Holography of Microspheres," *Applied Optics*, Vol. 41, 2002, pp. 5367-5375.

Yarin, A. L., Koombhongse, S., and Reneker, D. H., "Bending Instability in Electrospinning of Nanofibers," *Journal of Applied Physics*, Vol. 89, 2001, pp. 3018-3026.

Zuo, W., Zhu, M., Yang, W., Yu H., Chen, Y., and Zhang, Y., "Experimental Study on Relationship between Jet Instability and Formation of Beaded Fibers During Electrospinning," *Polymer Engineering and Science*, Vol. 45, 2005, pp. 704-709.

APPENDIX A
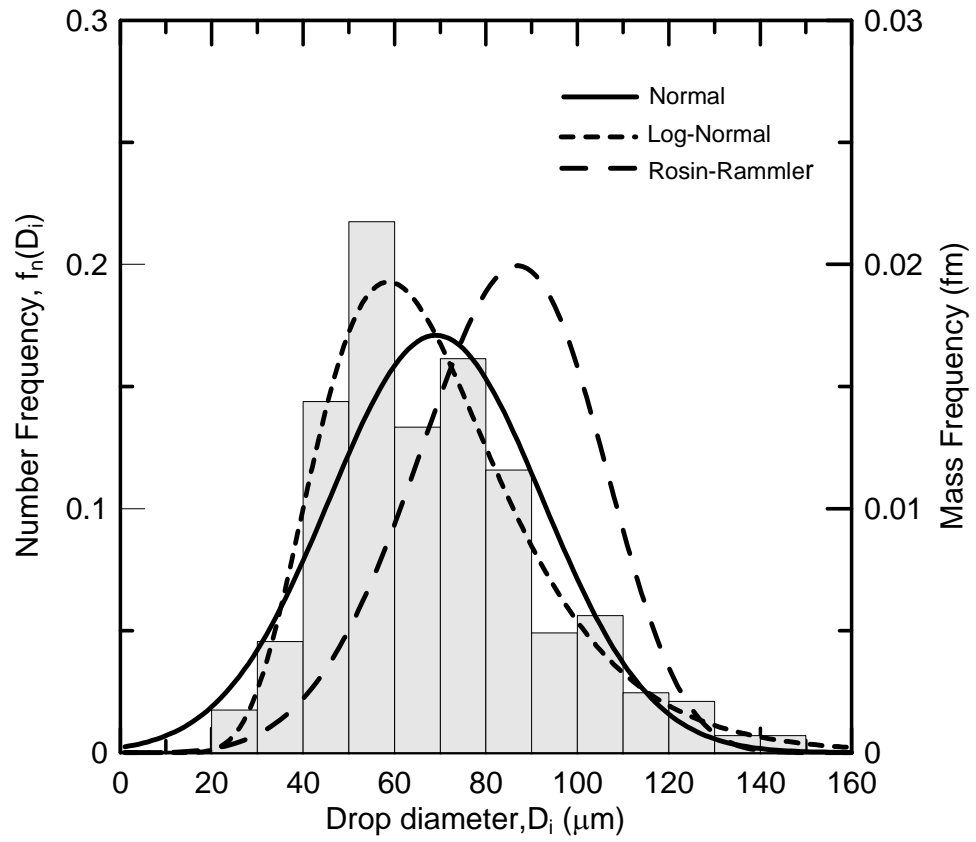
Figure A-1 drop size distribution (x/d$_o$=0)
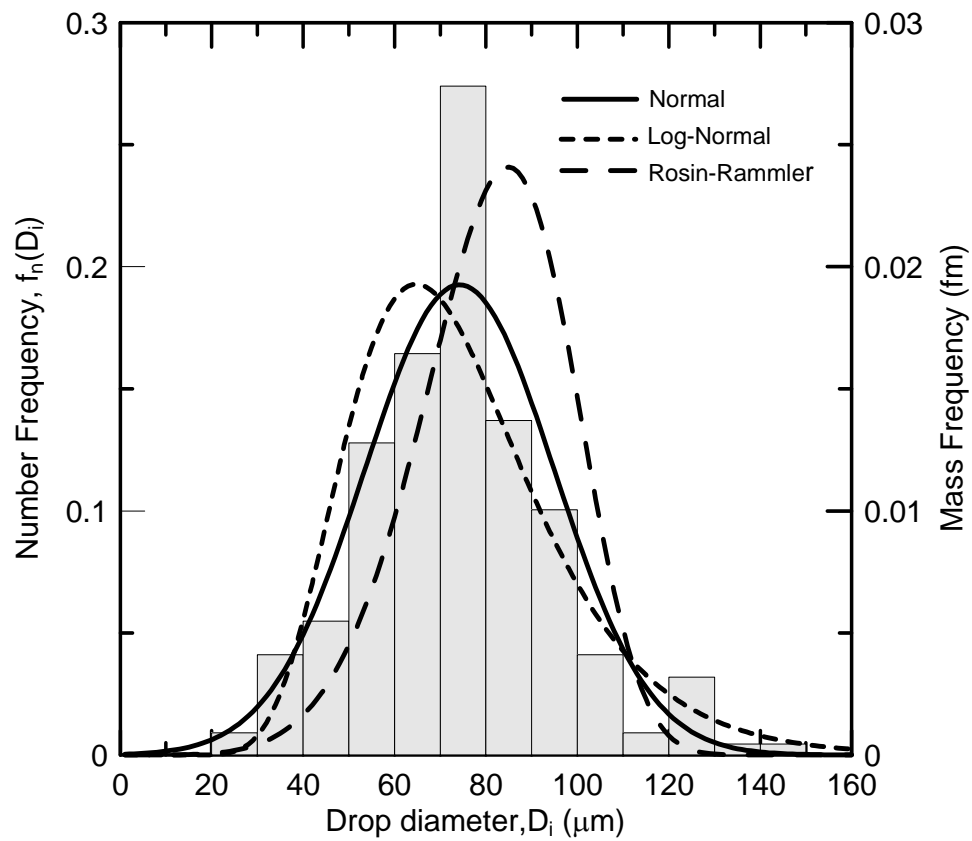
Figure A-2 drop size distribution (x/d_o=4.5)
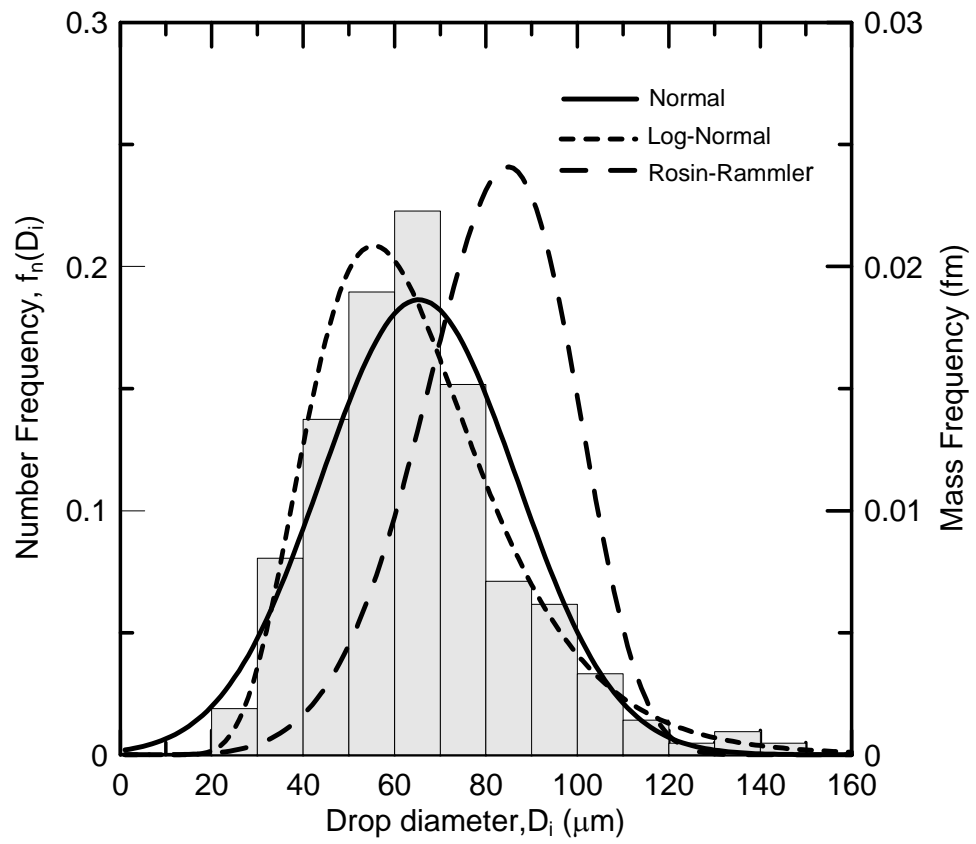
Figure A-3 drop size distribution ($x/d_o=13.5$)
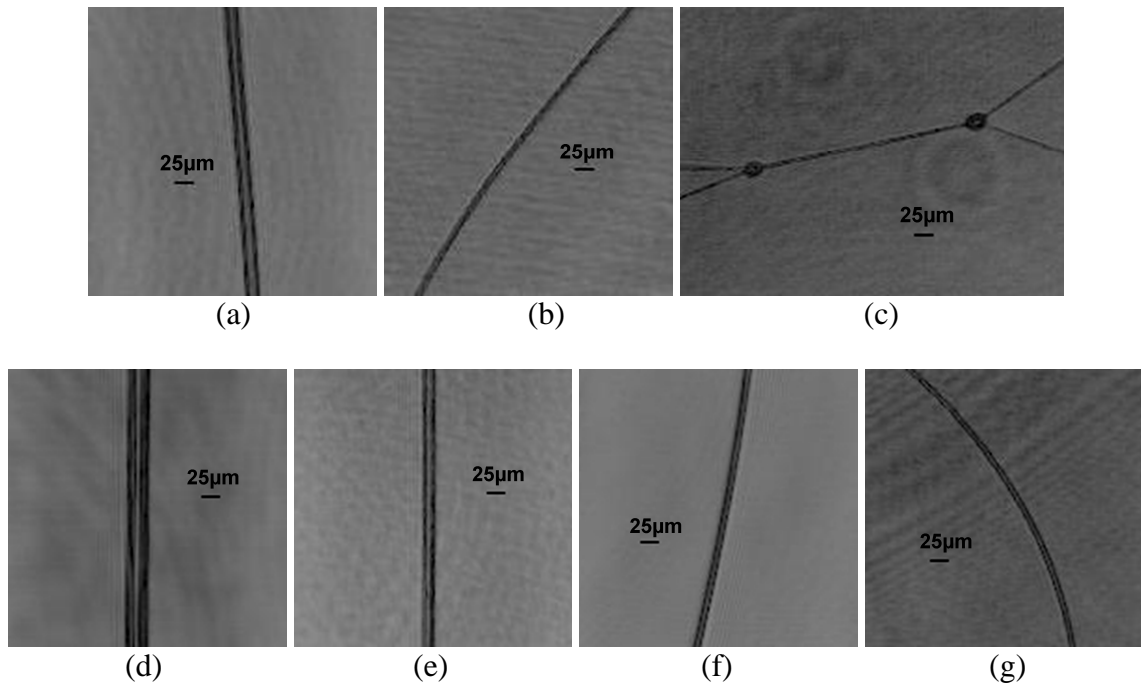
Figure B-1. Beaded and uniform fibers at different distances from the nozzle tip. The holograms were recorded in flight with the exposure time of 10ns. Images (a) through (c) correspond to distances of 3, 12, and 30 mm (0.5% solution, 7 kV and zero injection pressure). Images (d) through (g) correspond to distance of 3, 12, 30, and 42 mm (2.0% solution, 7 kV and 21 kPa injection pressure). The original images (a) through (g) were cropped from the original hologram recorded with field of view of 5×5 mm^2.
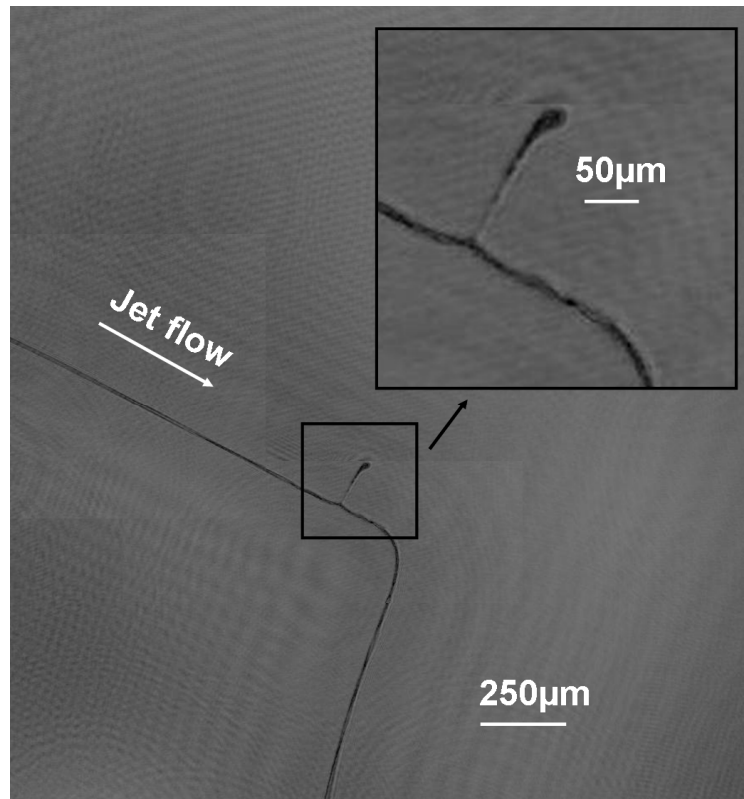
Figure B-2 Jet splaying. The original hologram was recorded at the location of y = 37 mm from the Taylor cone and with the field of view of 5×5mm^2. This image was obtained by cropping the original hologram, and the jet splaying was magnified in the large rectangular box. Test condition: 2.0% solution, 7 kV and 21 kPa injection pressure.
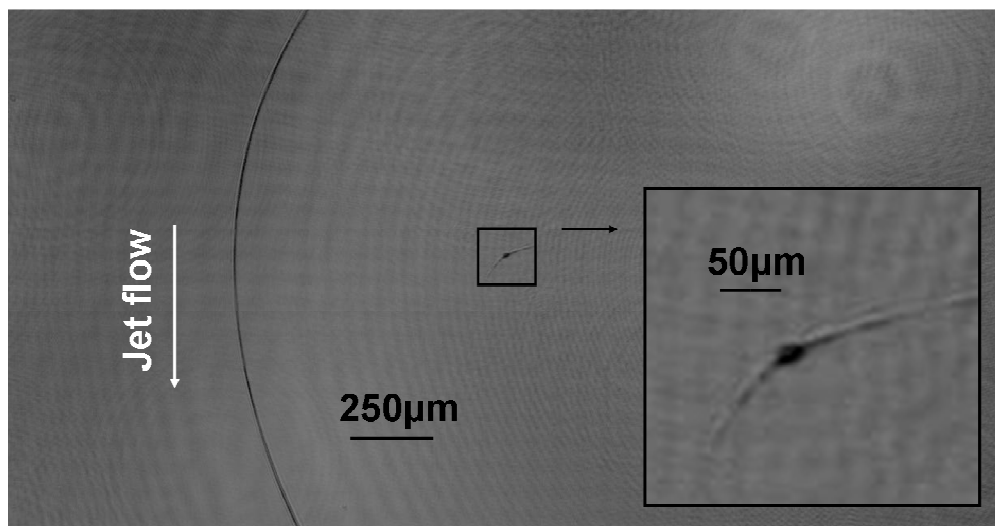
Figure B-3 Beaded fiber in-flight. The original hologram was recorded at the location of $y = 37$ mm from the Taylor cone and with the field of view of 5×5mm^2. Beaded fiber is shown in the large rectangular box with the high magnification. Test condition: 2.0% solution, 7 kV and 21 kPa injection pressure.

VITA

JAIHO LEE

Candidate for the Degree of

Doctor of Philosophy

Dissertation: DIGITAL HOLOGRAPHIC DIAGNOSTICS OF
              NEAR-INJECTOR REGION

Major Field: Mechanical Engineering

Biographical:

Personal Data: Born in South Korea, Nov 21 1976, the son of Jongil Lee and
        Younglye Kwon.

Education: Received Bachelor of Science degree and Master of Science degree
        in Mechanical Engineering from Chonbuk National University,
        Jeonju, Jeonbuk in Feb 2002 and Feb 2004, respectively.

Completed the requirements for Doctor of Philosophy degree in Mechanical
Engineering from Oklahoma State University, Stillwater, Oklahoma in May
2009.

Experience: Employed by Oklahoma State University, Department of
        Mechanical and Aerospace Engineering as a graduate teaching
        assistant and research assistant, 2005 to 2009.

Professional Memberships: American Physical Society

Name: JAIHO LEE   Date of Degree: May, 2009

Institution: Oklahoma State University   Location: Stillwater, Oklahoma

Title of Study: DIGITAL HOLOGRAPHIC DIAGNOSTICS OF
                NEAR-INJECTOR REGION

Pages in Study: 113   Candidate for the Degree of Doctor of Philosophy

Major Field: Mechanical Engineering

Scope and Method of Study: The primary breakup of near-injector region of liquid jets is of interest motivated by its application to gas turbine fuel injectors, diesel fuel injectors, industrial cleaning, medical spray, and inkjet printers, among others. The dense spray region near the injector is optically obscure for Phase Doppler Interferometer. Moreover, two-dimensional methods, e.g. shadowgraphy, have limited depth-of-field that renders them impractical for measuring droplet sizes and velocities of three-dimensional spray structure. The main objective of this study is to investigate the dense spray near the injector region of liquid jets using digital holography. The digital microscopic holography (DMH) was used for drop size and velocity measurements of the breakup of aerated liquid jets. Digital microscopic holography (DMH) is similar to digital inline holography (DIH) except that no lens is used to collimate the object beam. Two Nd:YAG lasers were used to generate two independent laser pulses, and the laser beams were expanded with an objective lens and a spatial filter. This eliminates two lenses from the typical optical path used for in-line holography, which results in a much cleaner hologram recording.

Findings and Conclusions: Using a commercial grade CCD for the DMH, the cost of CCD sensor needed for recording holograms could be reduced. The dense spray region of aerated liquid jets in crossflow was investigated using the DMH (test condition: 1mm jet diameter, 8% GLR, and $q_o=0.74$). The spray structure of aerated liquid jets was obtained by patching several high resolution holograms. Droplet velocities in three dimensions were measured by tracking their displacements in the streamwise and cross-stream direction and by tracking the change in the plane of focus in the spanwise direction. The distributions of the streamwise and cross-stream velocities were uniform in the near-injector region and could be characterized by the mass-average velocity except for very small and very large droplets. Double view DMH reduced the uncertainty of spatial measurements in the spanwise direction.

ADVISER'S APPROVAL: Khaled. A. Sallam